SAPIENZA
UNIVERSITÀ DI ROMA

Dipartimento di Ingegneria Astronautica, Elettrica ed Energetica

Dottorato di Ricerca in Ingegneria Aerospaziale
Ciclo XXV

NUMERICAL SIMULATIONS OF THE JUNO GRAVITY EXPERIMENT

Candidate	Advisor
Stefano Finocchiaro	**Prof. Luciano Iess**

ANNO ACCADEMICO 2011-2012

ANNO ACCADEMICO 2011-2012

Acknowledgements

I owe sincere thankfulness to my research advisor, Professor Luciano Iess, who guided me through these years. I am sure that this work would not have been possible without his support, understanding and encouragement I felt when working on my research. Thanks for all the opportunities you gave me.

I express sincere gratitude to Dr. Sami Asmar and the Radio Science Team at NASA-JPL for offering me the summer internship opportunity and for the continuous moral encouragement. A special thanks goes to Dr. William Folkner and Dr. Ryan Parks. I always enjoyed our discussions during the meetings at JPL. I learned a lot in those days.

Thanks to my labmates. Thanks for every laugh we had together. Every one of you contributed to the success of this work, just cheering me up when I needed it.

I would also like to show my gratitude to my parents and my brother, my safe harbour. Thanks to Alessia and Sophie, my new, small, beautiful family, for all your love and comprehension.

Stefano Finocchiaro

Summary

Introduction

The Italian Space Agency (ASI) is significantly involved in the NASA's Juno mission (cf. Section 1). The Italian contribution consists in the funding of the development, delivery and scientific support of two of the eight scientific instruments installed on the spacecraft: the Jovian InfraRed Auroral Mapper (JIRAM) and the Ka-band Translator System (KaTS), which is the core of the Gravity Experiment. The development and manufacturing of the KaTS was awarded to Thales Alenia Space – Italia with the scientific support of the Universities of Rome, Bologna and Forlì.

This research aims to assess the performance attainable by the Juno gravity experiment in terms of accomplishment of the scientific objectives.

The level-1 objectives of the gravity experiment are the determination of the mass of the Jupiter core and the detection of the possible presence of deep-seated zonal winds structures in the jovian atmosphere (cf. Section 2).

The level-2 requirements stated that the gravity field spherical harmonics coefficients up to degree 14 had to be estimated with an absolute uncertainty of 10^{-7}.

Determining the gravity of a planet requires a system experiment (cf. Section 3), involving a ground antenna (ground equipment), onboard instrumentation and adequate orbit determination software. The ground antenna transmits a radio signal towards the spacecraft orbiting the planet. The signal is received onboard and coherently transmitted back by means of an onboard transponder. The radio signal received on the Earth will keep the signature of the spacecraft dynamics in the Doppler shift of its frequency. The orbit determination software is crucial for the reconstruction of the dynamical perturbations determining the shift.

The radio system and the orbit geometry of Juno are realistically described in order to carry out a numerical simulation of the experiment with the scope of performing a covariance analysis of the fundamental parameters describing the gravity field of Jupiter and the tidal deformation. The numerical simulations are a very important step of the design process of the gravity science experiment because they offer the opportunity to detect in advance the criticalities (as well as the opportunities) in the orbit determination process much before the Jupiter arrival.

The early detection of criticalities allows corrections to the orbital geometry, mission operations and data analysis strategy that would be otherwise impossible once in Jupiter orbit. The decision to waive the level-2 requirements of the experiment, taken at project level, is a direct consequence of the results obtained in this thesis (cf. Section 4). The re-formulation of the requirements is currently in progress.

Moreover, it is possible to test the possibility to perform additional measurements not taken into account during the mission design phase. For example it has been proved that it is possible to obtain an estimate of the angular momentum of Jupiter from the Doppler signal due to the relativistic Lense-Thirring precession (cf. Section 5). It is the first time that General Relativity is used to constrain a geophysical parameter. This measurement is a strong contribution to the scientific return of the Juno mission.

This thesis collects the most important original results obtained during a multi-year participation to the Juno Science Team. The results shown are confirmed by independent studies of NASA-JPL.

1 The Juno mission

The Juno mission is the second mission of the NASA New Frontiers program. The spacecraft is a solar powered, spin-stabilized, polar orbiter of Jupiter devoted to the improvement of the knowledge about the origin, evolution and composition of the planet.

Juno was selected in May 2005 and initially scheduled for a 2009 launch, afterwards slipped to August 2011 (Grammier, 2009). The institutions contributing to the Juno mission are the NASA centers Jet Propulsion Laboratory and Goddard Space Flight Center, the Southwest Research Institute, the Italian Space Agency, University of Iowa, Applied Physics Laboratory of the Johns Hopkins University, Malin Space Science Systems, Danish Technical University and University of Wisconsin. Lockheed Martin is responsible for the spacecraft assembly and launcher procurement.

Figure 1.1 Juno mission logo

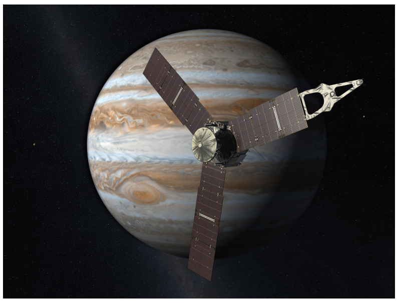

Figure 1.2 Juno artist's concept. Credit: NASA/JPL

1.1 Scientific objectives

The Juno mission will host onboard a set of 9 (8+1, cf. Section 0) scientific instruments that will collect important data about the atmospheric structure and composition, the magnetic and gravity field, the polar magnetosphere. The key objectives of the scientific investigation of the Juno mission are (Grammier, 2009):

1. Atmospheric composition:

Study of the formation of Jupiter's atmosphere by measuring the global O/H ratio (water abundance) and N/H ratio (ammonia).

2. Atmospheric structure:

Determination of the microwave opacity as a function of latitude and altitude, of the depths of clouds and atmospheric features (zones, belts, spots) and characterization of the microwave opacity of the polar atmosphere region.

3. Magnetic Field

Global mapping and determination of the long-term variations along with the determination of its spectrum to provide information about the core dynamo.

4. Gravity field

Provide constraint on the core mass, detect the centrifugal response of the planet to its own differential rotation (zonal winds structure) and the response to tides raised by the satellites.

5. Polar Magnetosphere

Investigate the auroral processes; characterization of the field-aligned currents that transfer angular momentum from Jupiter to its magnetosphere, of the auroral radio and plasma wave emissions, of the nature, location and spatial scale of auroral features.

1.1.1 Radio Science experiment objectives

The radio science instrumentation onboard Juno is designed for the accurate sensing of the Jupiter gravity field. In addition to its primary goal, it performed a solar conjunction experiment (General Relativity Test, August 2012) and will be used during the Earth Flyby to answer the unresolved question about the Earth anomaly.

1.1.1.1 Gravity Experiment

The gravity experiment in the scientific phase in orbit about Jupiter is the primary goal of the radio science instrumentation.

The measurement of the low degree gravity field (J_2, J_4, J_6) poses a radical constraint on the mass of the planet's core.

The determination of the finer structure of the gravity field will help in understanding the magnitude and the extension in depth of the convective phenomena in the atmosphere of Jupiter.

Radio science will also return a measurement of the response of Jupiter to tides raised by satellites (in particular the Galilean moon Io).

The thesis focuses on this particular experiment. The results are shown in Section 4.

Under certain hypotheses it will be possible to attempt a measurement of the planet's angular momentum by assuming the general relativity correct and measuring the Lense-Thirring acceleration acting on the spacecraft when flying close to Jupiter. The Lense-Thirring effect is supposed to be large, given the mass of the planet and its rotation period (approximately 10 hours). This particular measurement requires a modification of the orbit determination code that will be exhaustively exposed in Section 5.

1.2 Scientific Payload

The scientific payload of the Juno mission is composed by 8 instruments and a camera for education and public outreach (E/PO).

The nine instruments have been provided by different institutions in Europe and in the USA, thus requiring a strong effort in the coordination of the activities.

The Gravity Science instrument is a joint product of JPL and the Italian Space Agency (ASI). JPL developed the Small Deep Space Transponder (**SDST**) and the antenna system, while ASI took the responsibility of the Ka-band Translator System (**KaTS**) manufactured by Thales Alenia Space – Italia. The instrumentation will be used to determine the perturbation acting on the spacecraft, and the consequent Doppler shift on the X and Ka band radio signal, due to the irregularities of the gravity field of Jupiter (Bolton, 2010). The KaTS will be further descripted in Section 3.2.1.

The ASI contribution is not limited to gravity science but it funds also the Jupiter Infrared Auroral Mapper (**JIRAM**), an instrument that will study the upper layers of the Jupiter's atmosphere at infrared wavelength (2-5 μ) using an imager and a spectrometer (Bolton, 2010).

The magnetometer (**MAG**) is a product of Goddard Space Flight Center. It will accurately map the magnetic field of Jupiter. The instrument is composed by two Flux Gate Magnetometers and two Advanced Stellar Compasses (ASC), procured by the Danish Technical University (DTU), that will return the precise information on the magnetometers location and orientation (Bolton, 2010).

The microwave radiometer (**MWR**) is provided by JPL. It will use six antennas disposed on the spacecraft body that will measure the radiation from Jupiter at six different wavelengths returning data on the water and ammonia abundance and on the circulation of Jupiter's deep atmosphere (Bolton, 2010).

Jupiter Energetic-particle Detector Instrument (**JEDI**) is an instrument of the Applied Physics Laboratory – Johns Hopkins University (APL). Its three sensing heads will sort the incoming particles into mass, species and energy discriminating between ions and electrons (Bolton, 2010).

Southwest Research Institute (SwRI) provides the Jovian Auroral Distributions Experiment (**JADE**) and the Ultraviolet Spectrometer (**UVS**). The first instrument will return the distribution of particles in the polar magnetosphere of Jupiter. It is composed by a single head ion mass spectrometer and three electron energy per charge analyzers. The ultraviolet spectrometer will use a 1024 256 micro channel plate (MCP) detector to provide spectral images of the UV auroral emission in the polar magnetosphere (Bolton, 2010).

The University of Iowa contribution to the Juno mission, the Plasma Waves instrument (**Waves**), will measure the radio and plasma spectra in the auroral region. It is composed by an electric dipole antenna and a magnetic search coil (Bolton, 2010).

The Visible Camera by Malin Space Science Systems, **JunoCam**, is a four filters color camera that will be used for Educational and Public Outreach purposes (Bolton, 2010).

1.3 The Juno spacecraft

Juno is a solar powered, spin-stabilized spacecraft. The choice of a solar powered spacecraft is due to the cost and the uncertain availability of a radioactive power source (Grammier, 2009). At Jupiter the solar power is nearly 2-3% the power available for a spacecraft in orbit about the Earth, therefore the spacecraft had to be provided with three large solar arrays (total area 60 m^2, active area 50 m^2 (Nybakken, 2011) disposed symmetrically about the main hexagonal bus. Moreover the cruise trajectory and the science orbits have been designed in order to minimize the Sun occultation. The limited power budget excluded the possibility of the selection of a three-axis control on the spacecraft attitude, which would have required power-consuming reaction wheels (Grammier, 2009). Hence the selection of a spinning spacecraft that also brought the benefit of avoiding complex scan-platforms. An appropriate distribution of the instruments sensors guarantees the necessary field of view necessary for the measurements, avoiding also complex spacecraft maneuvers (Grammier, 2009).

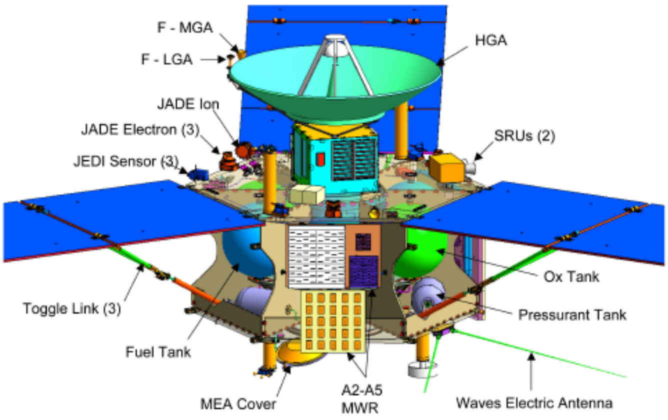

Figure 1.3 Exploded view of the Juno spacecraft with sensors and instrument location (Grammier, 2009).

One of the greatest problems in the design of the spacecraft was the harsh Jupiter radiation environment. The goal of the design is to survive the Jupiter environment while at the same time containing the expanses maintaining heritage technology for the instruments (Bolton, 2010). This has been achieved by designing a shielding titanium vault (weighting nearly 157 kg) containing the more sensitive electronics and choosing an orbital geometry which keeps the radiation dose to acceptable levels (Nybakken, 2011).

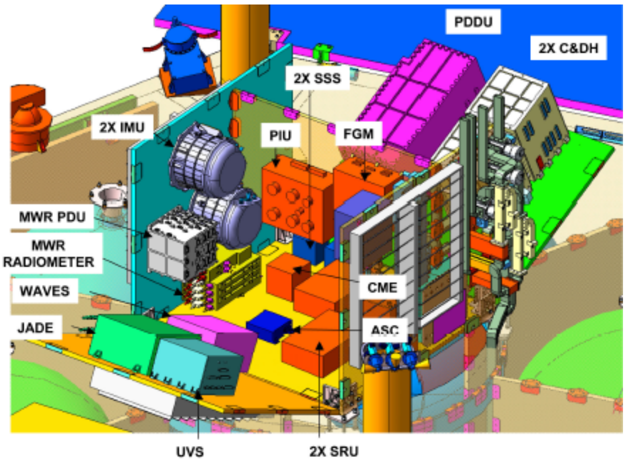

Figure 1.4 Electronics disposal within the radiation vault (2009) (Grammier, 2009).

The geometry of the first 15 orbits of the scientific phase ensures the minimum radiation dose. In fact the observation of the instruments other than radio science are concentrated in the early orbits. While the line of apses rotates northward the radiation dose increases.

The first 15 orbits return global coverage with a 24° spacing in longitude. Considering the latest orbits the spacing reduces to 12°.

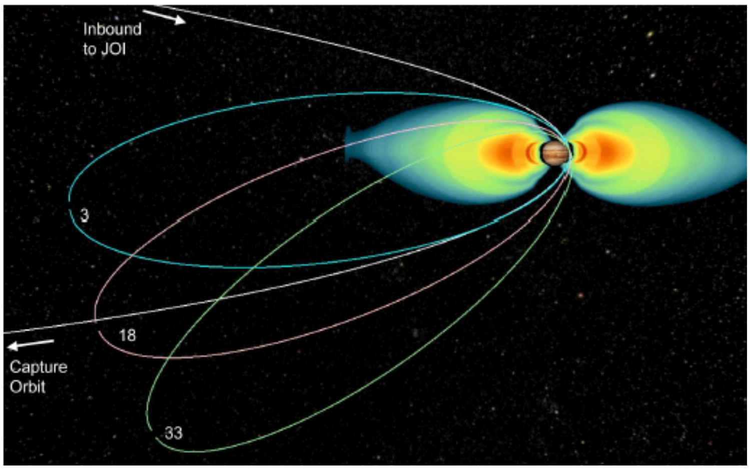

Figure 1.5 Juno orbit geometry with respect to Jupiter radiation belts (Grammier, 2009).

The communication system is composed by a suite of antennas, the X-band Deep Space Transponder (DST) and the Ka-band Translator System (KaTS). As shown in Figure 1.3 the spacecraft is provided with a main High Gain Antenna (HGA), which will be used as the main device for science measurements, a fore Medium Gain Antenna (MGA) , fore and aft Low Gain Antenna (LGA) and an aft toroid low gain antenna, enabling communication during the main engine burns (Grammier, 2009).

The main engine will execute the most important maneuvers during the mission (DSMs, JOI, PRMs) and is complemented by four rocket engine modules (REM) towers each consisting of two lateral and one axial thrusters.

1.4 Trajectory

1.4.1 Launch phase

The spacecraft was launched in August 2011 on an Atlas V 551 from the Kennedy Space Center, Florida. The launch period was 22 days (August 5-26) and it was optimized to maximize the mass injected into the science orbits about Jupiter (Nybakken, 2011).

Figure 1.6 Juno launch on Atlas V 551 (Nybakken, 2012).

1.4.2 Cruise phase

After the launch phase and spacecraft separation, Juno was inserted in a 5 years ΔV-EGA (Earth gravity assist) trajectory towards Jupiter.

The trajectory started with the phase called Inner Cruise 1. The first trajectory correction maneuver (TCM) took place at launch + 20 days (Nybakken, 2011). It will be followed by 12 other TCMs that will be executed in the throughout the trajectory.

The second cruise phase (Inner Cruise 2) started 63 days after the launch. The main events of this phase are the two Deep Space Maneuvers (DSMs) that were scheduled to be executed 13 months after the launch to get a first targeting towards the Earth Flyby. These maneuvers worked as a test for the spacecraft main engine (ME) (Nybakken, 2011).

The third cruise phase will be the Inner Cruise 3 where the Earth Flyby (EFB) will occur, 26 months after launch. This phase will serve as a rehearsal for the science phase (Nybakken, 2011).

Following the Inner Cruise 3 there will be a Quiet Cruise phase that will end with the Jupiter Orbit Insertion (JOI). This burn will be executed by the main engine and will insert Juno in a 107 days capture orbit about Jupiter, setting up the orbital geometry for the scientific phase. The precise orbit period (10.9725 days) and perijove synchronization with Goldstone DSS-25 visibility will be acquired by means of a Period Reduction Maneuver (PRM) (Nybakken, 2011).

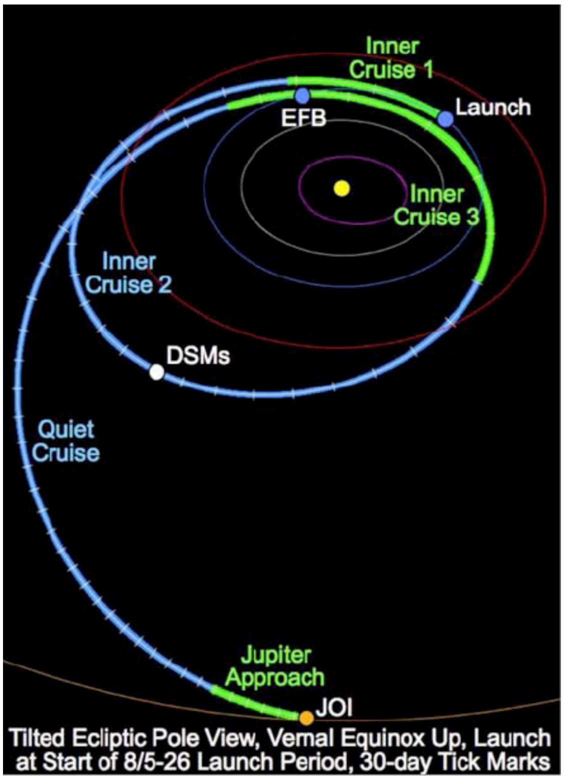

Figure 1.7 Juno mission cruise phases (Nybakken, 2012).

1.4.3 Scientific phase

The science phase of the mission consists in 32 highly eccentric ($e = 0.9466$) polar orbits ($i = 90° \pm 10°$) about Jupiter (Grammier, 2009). The orbits 3 to 33 are science orbits while orbit 1 and 2 contain cleanup for the JOI and a PRM. The orbits are repetitive in an inertial reference frame, except for the argument of periapsis that drifts northwards by 1 degree per orbit because of the effect of Jupiter's oblateness. The apoapsis is located at nearly 39 jovian radii, while the periapsis is approximately at 1.06 jovian radii. The orbit period guarantees a global coverage of the planet surface with a spacing of 12 degrees in longitude, while minimizing the radiation dose.

The periapses dedicated to gravity science are the number 4 (early gravity science orbit) and number 9 to 32 for a total of 25 gravity science orbits. The remaining orbits are scheduled for MWR observations. Gravity science and MWR requires incompatible spacecraft attitudes. During gravity science passes the spacecraft HGA must point the Earth, while in MWR orbits the radiometer must point nadir.

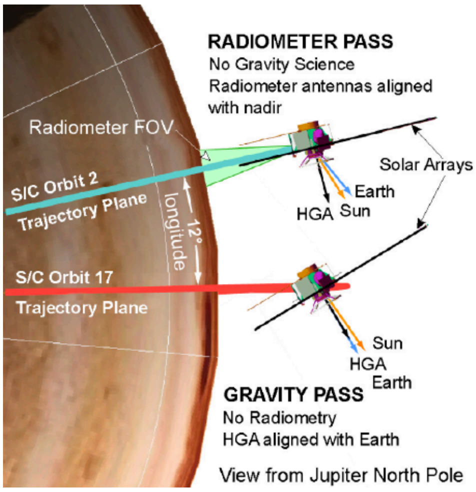

Figure 1.8 Juno different attitude during a radiometer or a gravity pass (Grammier, 2009).

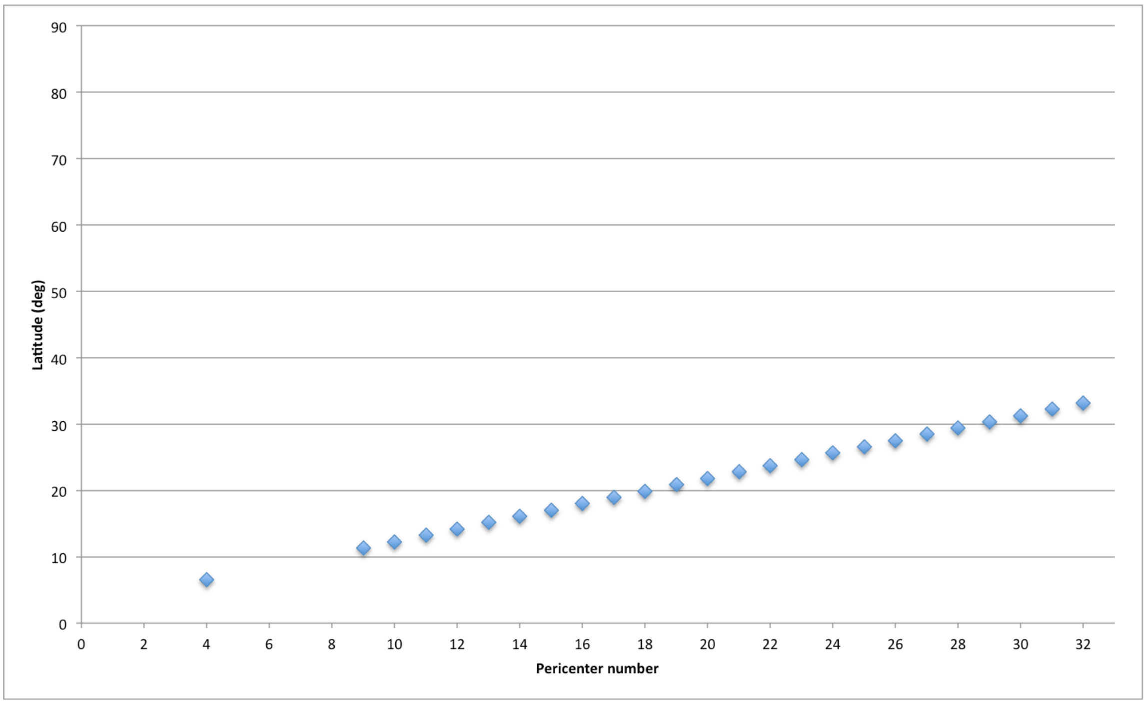

Figure 1.9 Pericenters latitude (degrees)

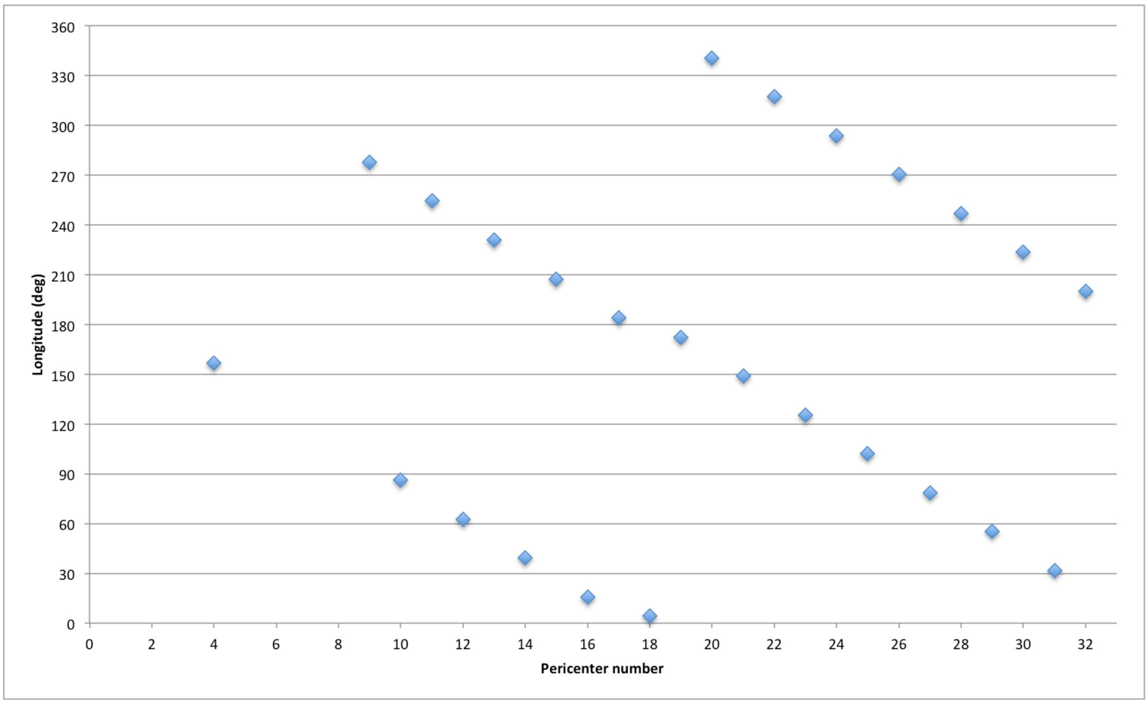

Figure 1.10 Pericenters Longitude (degrees)

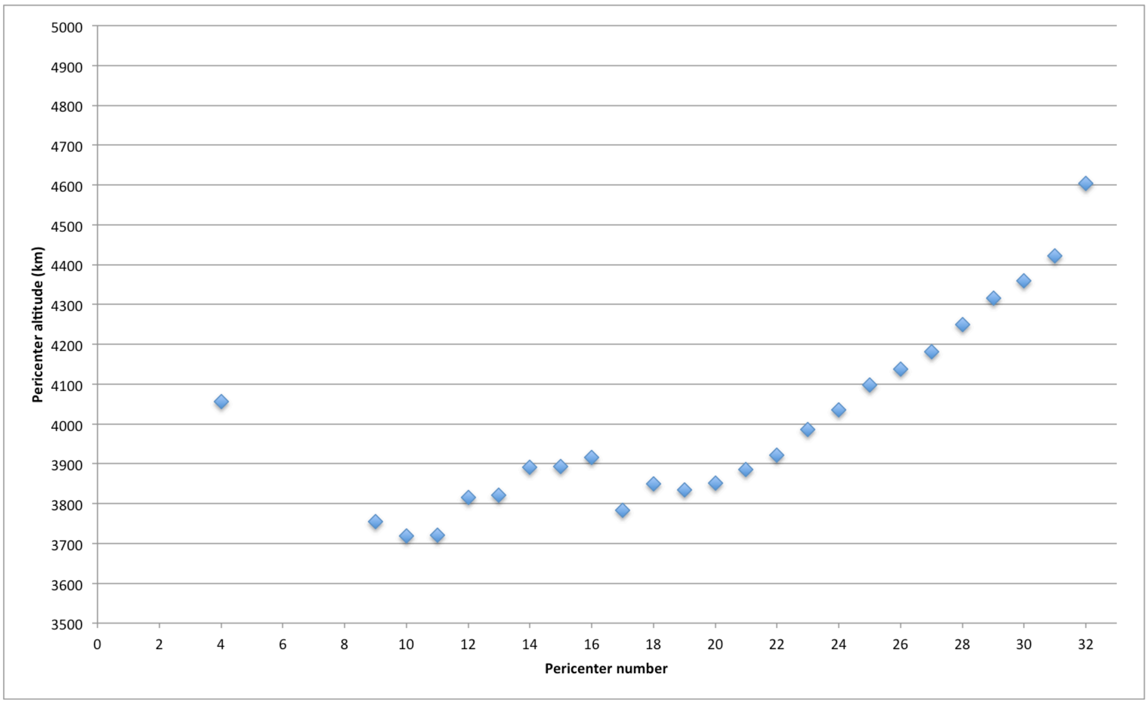

Figure 1.11 Pericenters altitude (kilometers)

The mean altitude of the pericenters is 4000 km.

While achieving a good coverage in longitude, this kind of trajectory allows only a limited coverage in latitude.

When flying on a highly eccentric orbit the limited coverage in latitude can be a possible source of problem in gravity science experiments, since the spacecraft will be effectively sensitive to the fine structure of the gravity field only in a small region about the pericenter, leaving therefore uncovered vast regions of the surface.

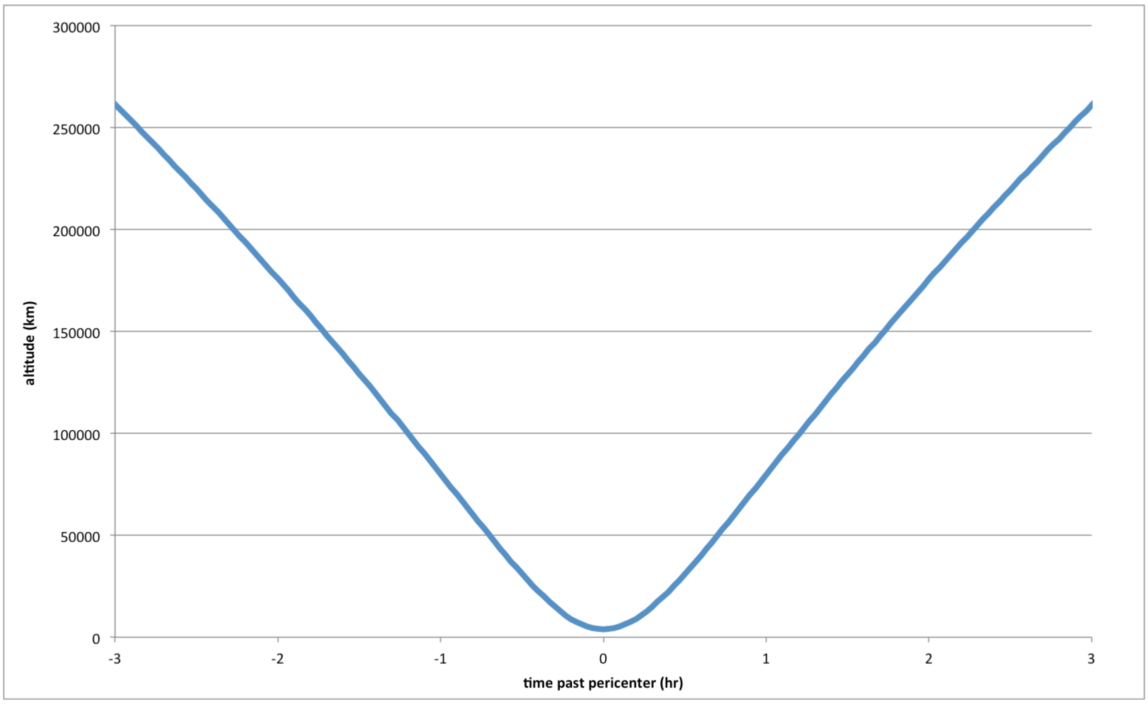

Figure 1.12 Altitude vs time at closest approach (orbit 22)

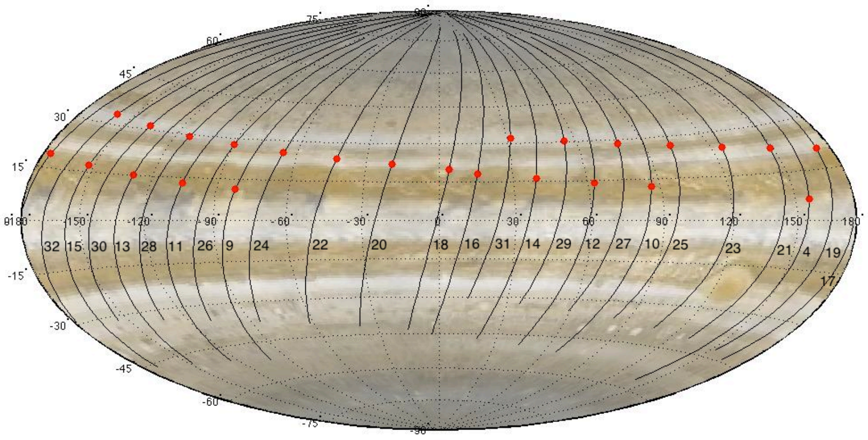

Figure 1.13 Juno gravity science orbits ground tracks (one hour about the pericenter). The red dots indicate the perijoves.

A crucial factor in gravity science experiment is the orientation of the orbit plane with respect to the line-of-sight with the Earth. The experiment relies on the measurement of the radial velocity of the spacecraft, hence it is important to have the orbit plane almost aligned with the Earth direction in order to maximize the Doppler signal coming from the projection of the spacecraft velocity onto the line-of-sight. The need of a constantly illuminated orbit drove the choice of the inertial orientation towards a plane nearly orthogonal to the Sun direction. From Jupiter, the Earth and the Sun have a very small angular separation; therefore the orbit plane results nearly orthogonal also to the Earth direction, thus not achieving the best scenario for radio science measurements. Figure 1.14 shows the angle between the orbit plane and the line-of-sight with the Earth for all the 25 gravity science orbits.

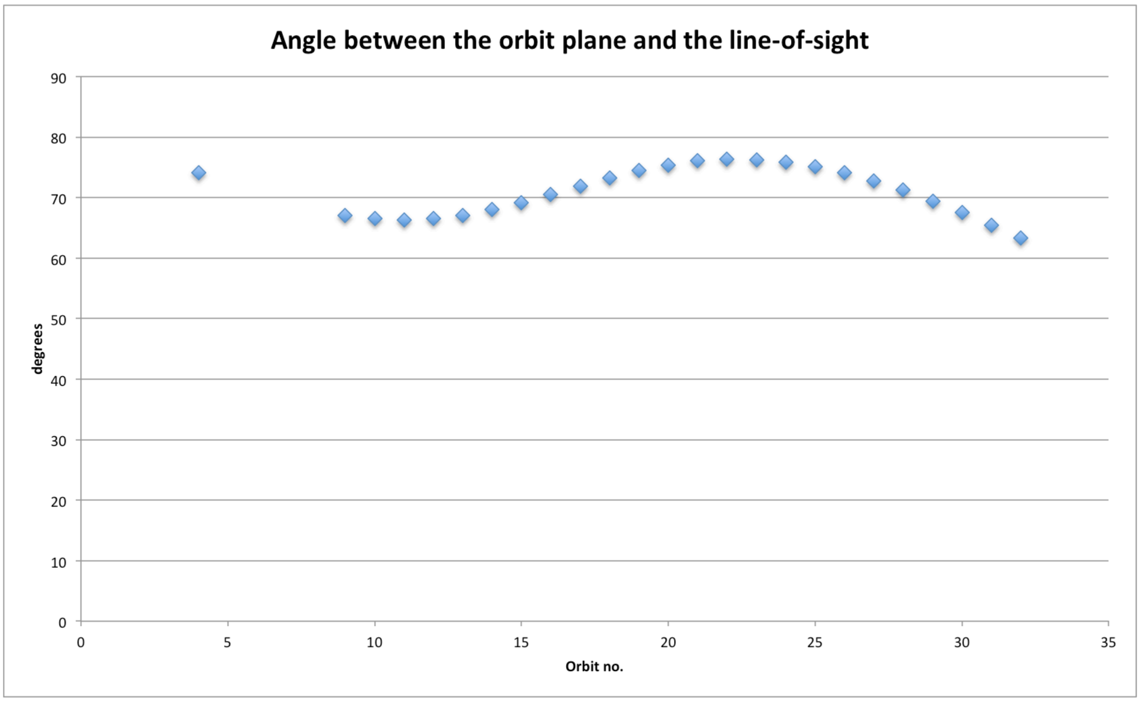

Figure 1.14 Angle between the orbit plane and the line-of-sight with the Earth.

1.4.4 De-orbiting

The final maneuver of the mission will be executed during orbit 34 and will insert Juno in an orbit that will plunge the spacecraft in the jovian atmosphere, in observation to the planetary protection regulation (Nybakken, 2011).

2 The planet Jupiter

2.1 Formation

The giant planets are rich in primary cosmic elements hydrogen and helium, therefore they must have formed early in the process of planetary formation. After their formation they contributed to shape the solar system dynamical environment due to their gravitational action.

The two competing theories on the formation of Jupiter are the *gravitational disk instability* or (*direct collapse*) and the *nucleated instability*. Both the theories try to explain how the giant planets formed out from the proto-nebula, which resulted by a stellar explosion (Lunine *et al.*, 2004).

The gravitational disk instability theory postulates that when the proto-nebula started to cool and condense, small particles of gas and dust started to aggregate, generating regions of density instability. One of these instabilities was able to gravitationally attract more and more gas and dust becoming a giant gaseous proto-planet. Not all the density instabilities become proto-planets. The instability must be stable with respect to disruptive forces (solar tides, pressure perturbations, etc.). The mass of the proto-planet might have been much larger than the final planetary mass. The external gas layers may have been removed by solar UV radiation or extra-solar evaporation. The final planet is entirely gaseous with no solid core. All the processes involved in the direct collapse theory do not explain the abundance of heavy elements on Jupiter with respect to the solar abundance. As a consequence the direct collapse seems to be the less probable theory for the Jupiter formation (Lunine *et al.*, 2004).

The nucleated instability theory hypothesizes that a terrestrial planet embryo formed in the Jupiter region of the solar nebula. The mass of the planet embryo had to grow to a certain minimum size (critical mass) to permanently capture the gas of the nebula, while enough gas mass is present in the region (nebula lifetime 10 million years). The result of this process is a differentiated planet with a solid core and a gas envelope. For a distance of 5 AU the minimum critical masses ranges from 1.5 M_E (Earth masses) to 20 M_E (Lunine *et al.*, 2004).

Measuring the low degree gravity field will help determining the size of the Jupiter's core (if any) giving an important contribution to the comprehension of the origin of the planet.

2.2 Interior

Jupiter is at first order a gas giant of helium and hydrogen in hydrostatic equilibrium. The temperature of the interior is nearly 20 000 K result of the transformation of the nebula gas gravitational energy into heat by means of contraction. The contraction proceeds at a rate of 3 cm per year the interior, while the interior is cooling at a rate of 1 K per million years. The cooling and contraction process implies a fluid interior since it causes a significant intrinsic energy flux, demonstrated by the fact that Jupiter emits more energy than it receives from the sun, and convective motions in most of the interior (Bagenal *et al.*, 2004).

The convective motions are responsible for the homogeneity of the planet and cause the internal dynamo generating the external magnetic field (Bagenal *et al.*, 2004).

Jupiter composition closely resembles the Sun. The main difference is the abundance of heavy elements. While the Sun only has the 2% of its mass in elements other than hydrogen and helium, for Jupiter models return an abundance of heavy elements ranging from 3% to 13%. Half of this mass is supposed to be oxygen, which is the third most diffuse species in the universe. An important measurement necessary to understanding the Jupiter interior composition is the bulk water abundance. This measurement combined with the high accuracy gravity and magnetic fields mapping, will be crucial to understand the Jupiter internal composition (Bagenal *et al.*, 2004).

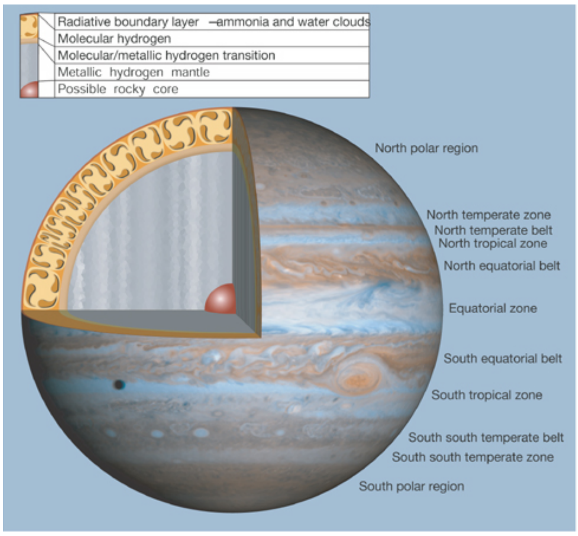

Figure 2.1 Jupiter internal structure schematics (Bagenal *et al.*, 2004).

2.3 Atmosphere

Jupiter is provided of the largest atmosphere in the Solar System. Conventionally the atmosphere is defined as the region extending down to 20 bars (Seiff *et al.*, 1998).

A layer of clouds, composed of ammonia crystals and hydrosulfide, covers the planet. The clouds are distributed in zonal bands circulating at different speed and direction. The white bands are called *zones* while the dark ones are called *belts*. The mutual interaction between the bands generates storms and turbulence, which manifest as ovals on the planet surface. The zonal bands show an annual variation of width, intensity and color but remain stable on larger timescales. Different hypotheses have been formulated on the extension in depth of the banded structure (Ingersoll *et al.*, 2004).

In the traditional view, the winds are shallow. The zones and ovals, where the cloud deck is higher, are features were the air is warmer than in the surrounding same pressure region. The warm air tends to rise while the cold air in the belts sinks; therefore the cloud deck is higher in the warmer zones (Ingersoll *et al.*, 2004).

On the other hand, a different theory states that if the fluid is at constant temperature on constant pressure surfaces, the winds could be the external manifestation of differentially rotating cylinders concentric with the planet's polar axis. In this theory the winds extend much deeper in the planet interior (Ingersoll *et al.,* 2004).

The Galileo Entry Probe penetrated the cloud layer in 1995. It registered the presence of zonal winds at its deepest penetration (0.2% of the planet equatorial radius) (Kaspi *et al.,* 2010).

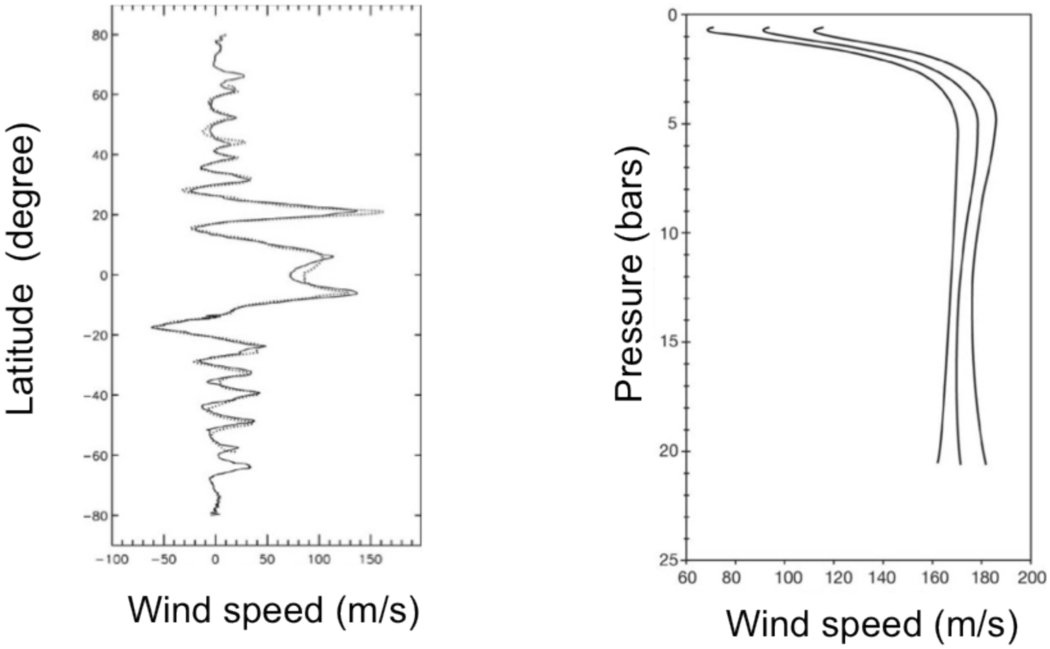

Figure 2.2. Wind speed profile at different penetration depth (Porco *et al.,* 2003;Atkinson *et al.,* 1998).

The observation of flashes of lightning in the atmosphere could be the evidence of the presence of a thin water clouds layer below the ammonia clouds. The water polarity creates the conditions for the charge separation needed to produce lightning (Elkins-Tanton, 2006).

2.4 Magnetic Field

The Jupiter's inner mantle is composed by metallic conductive hydrogen under convective motion. A dynamo effect converts part of the energy involved in the conductive motion in the energy necessary to create a magnetic field. The more energetic is the convective motion the more intense is the dynamo effect and the resultant magnetic field.

The magnetic field of Jupiter is substantially a dipole, with the axis tilted by 9.6° with respect to the polar axis (Guillot *et al.*, 2004).

The magnetic field B is expressed as the gradient of the scalar potential W, whose spherical harmonic expansion is (Guillot *et al.*, 2004):

$$B = -\nabla W$$

$$W = R_e \sum_{1}^{\infty} \left(\frac{R_e}{r} \right)^{n+1} \sum_{m=0}^{n} \left\{ g_n^m \cos(m\phi) + h_n^m \sin(m\phi) \right\} P_{n,m} \cos(\vartheta)$$

The coefficients g_n^m and h_n^m are called magnetic moments.

n	**m**	g_n^m	h_n^m
1	0	4.208	0.000
1	1	-0.660	0.261
2	0	-0.034	0.000
2	1	-0.759	-0.294
2	2	0.483	0.107
3	0	…	0.000
3	1	…	…
3	2	0.263	0.695
3	3	-0.069	-0.247

Table 2.1. Jupiter magnetic moments in Gauss (Connerney *et al.*, 1982).

The strong magnetic field along with the Jupiter fast rotation generates a huge a magnetosphere (the largest in the Solar System), extending to a distance of 100 Jupiter radii. It is traditionally divided into *inner magnetosphere*, the region below the 10 Jupiter radii, *middle magnetosphere*, from 10 to 40 Jupiter radii, and *outer magnetosphere*, from 40 to 100 Jupiter radii. The uniqueness of the Jupiter magnetosphere comes from the fact that it derives much of its plasma internally from the moon Io. Without the contribution of the Io plasma the magnetosphere would extend only up to nearly 42 Jupiter radii (Khurana *et al.*, 2004).

Since Jupiter has no solid surface, the rotational period of Jupiter is determined from the radio emission at decametric or decimetric wavelengths from the plasma trapped in the Jupiter's magnetic field. Some of the radio sources are fixed with respect a particular system of longitudes called System III. The rotation period of the radio sources define the rotation period of the planets itself (Khurana *et al.*, 2004).

2.5 Gravity Field

2.5.1 The ellipsoidal gravitational potential

The planet Jupiter is a gas giant spinning very fast (10 hours rotation period) about its polar axis. The rotation deforms the planet so that its shape is closer to an ellipsoid than to a sphere and this will affect the external gravitational potential.

W.B. Hubbard (Hubbard, 2012) describes a simplified model of the hydrostatic interior of Jupiter considering a scaled Maclaurin model. The resulting ellipsoid is described in terms of spherical harmonics by a series of even zonal harmonics. Their magnitude decreases exponentially with the degree of the zonal harmonic.

n	**$J_n \cdot 10^6$ (calculated)** Hubbard 2012	**$J_n \cdot 10^6$ (observed)** Jacobson 2003

2	14696.43	14696.43 ± 0.21
4	-587.14	-587.14 ± 1.68
6	30.82	34.25 ± 5.22
8	-1.862	…
10	0.1227	…
12	$-8.573 \cdot 10^{-3}$	…
14	$6.253 \cdot 10^{-4}$	…
16	$-4.711 \cdot 10^{-5}$	…
18	$3.641 \cdot 10^{-6}$	…
20	$-2.873 \cdot 10^{-7}$	…
22	$2.304 \cdot 10^{-8}$	…
24	$-1.873 \cdot 10^{-9}$	…
26	$1.534 \cdot 10^{-10}$	…
28	$-1.154 \cdot 10^{-11}$	…
30	$6.358 \cdot 10^{-13}$	…

Table 2.2. Jupiter ellipsoid gravity model coefficients (Hubbard, 2012).

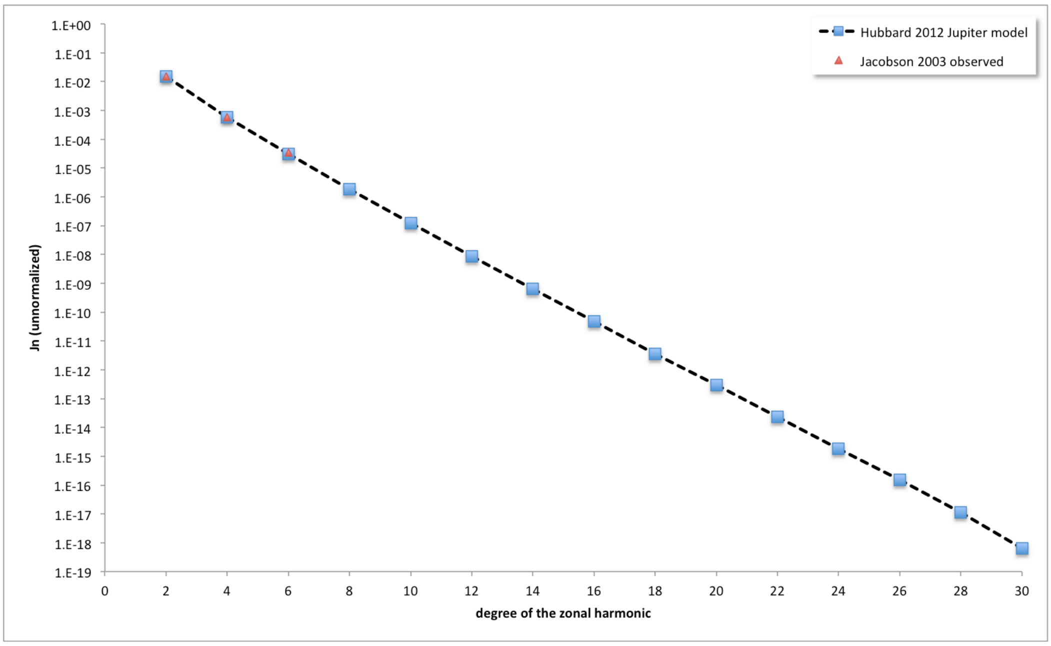

Figure 2.3. Jupiter ellipsoid gravity model (cf. Table 2.2).

2.5.2 The zonal winds potential

In addition to the rotation other factors intervene in the definition of the gravitational potential of Jupiter.

Direct observational data of the cloud layer on Jupiter surface returned evidence of the presence of strong winds zonally distributed on the planet surface. The winds speed is supposed to exponentially decrease in the radial direction proportionally to the scale height (Kaspi *et al.*, 2010).

If the zonal winds extended at high pressures (large scale height) they would involve a significant amount of the planetary mass. Therefore the gravitational signature of the winds increases with the depth. If the winds were very shallow the gravitational signature would be almost negligible. On the other hand if they penetrate in depth inside the planet their gravitational signature would be relevant (Kaspi *et al.*, 2010).

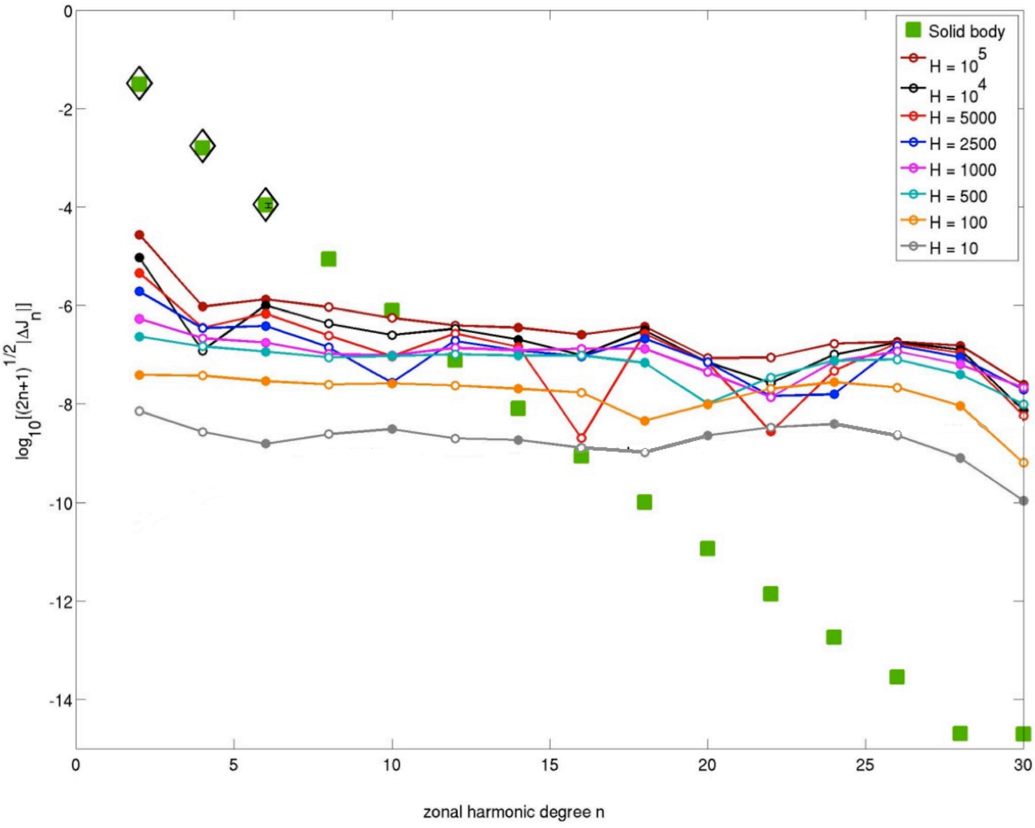

Figure 2.4. Gravity spectrum for different winds penetration depth (Kaspi *et al.*, 2010). H (km) is the scale height of the exponential attenuation.

Component of the power spectrum of the zonal winds can be found also in the tesseral and sectoral moments of the spherical harmonics expansion, even if rapidly decreasing in magnitude with the order.

The goal of the Juno gravity experiment is to exploit the sensitivity of the instrument onboard the spacecraft to take proof of the extension in depth of the zonal winds.

2.5.3 Jupiter Love numbers

Further contribution to the exploration of the planet Jupiter will be given by the measurement of the tidal deformation of the body under the combined effect of its satellites (mainly the galilean moon Io) and the Sun.

Perturbing body	GM (km^3/s^2)	Semi-major axis (km)	Revolution period (dd)	Tidal parameter
Io	5959.9	421 800	1.796	$2.29 \cdot 10^{-7}$
Europa	3202.7	671 100	3.551	$3.06 \cdot 10^{-8}$
Ganymede	9887.8	1 070 400	7.155	$2.33 \cdot 10^{-8}$
Callisto	7179.3	1 882 700	16.69	$3.10 \cdot 10^{-9}$
Sun	$1.3273 \cdot 10^{11}$	778 412 020	4330.6	$8.11 \cdot 10^{-10}$

Table 2.3 Tidal parameters of Jupiter with respect to the Galilean satellites and the Sun

The gaseous nature of the planet, allows assuming a constant proportionality factor for the tidal deformation at every frequency and direction.

2.6 Satellites and rings

A Rings system and a large number of moons surround the planet Jupiter. In the XVII century, Galileo Galilei observed 4 moons orbiting the giant planet. In recent times, astronomers have observed other 63 Jupiter moons and the long-exposure Voyager 1 images detected the ring system (Smith *et al.*, 1979).

Jupiter moons divide into 3 main groups: *inner moons* or *ring-moons*, *Galilean moons*, *outer* or *irregular moons*.

Four small bodies named Metis, Adrastea, Amalthea and Thebe compose the inner moons group. The dust separating from these bodies and pulled inward or outward by orbital stability forms the ring system (Burns *et al.*, 2004).

The ring system is composed by three main components: the *halo*, the *main ring* and the two *gossamer rings*.

The main ring extends from 1.70 to 1.803 jovian radii. It is the brightest ring and is formed by dust particles from Adrastea and Metis pulled inward towards Jupiter. At the inner limit of the main rings there is a transition toward the region known as halo. The halo ring rapidly increases in thickness up to 20 000-40 000 km opening in a torus which disappears at 1.4 Jovian radii. The thickness refer to the highest height at which material can be observed, but the most of the material in the halo is concentrated in a few hundreds km from the equatorial plane. The inner gossamer ring is composed by material coming from Amalthea while the outer ring is alimented by dust from Thebe (Burns *et al.*, 2004).

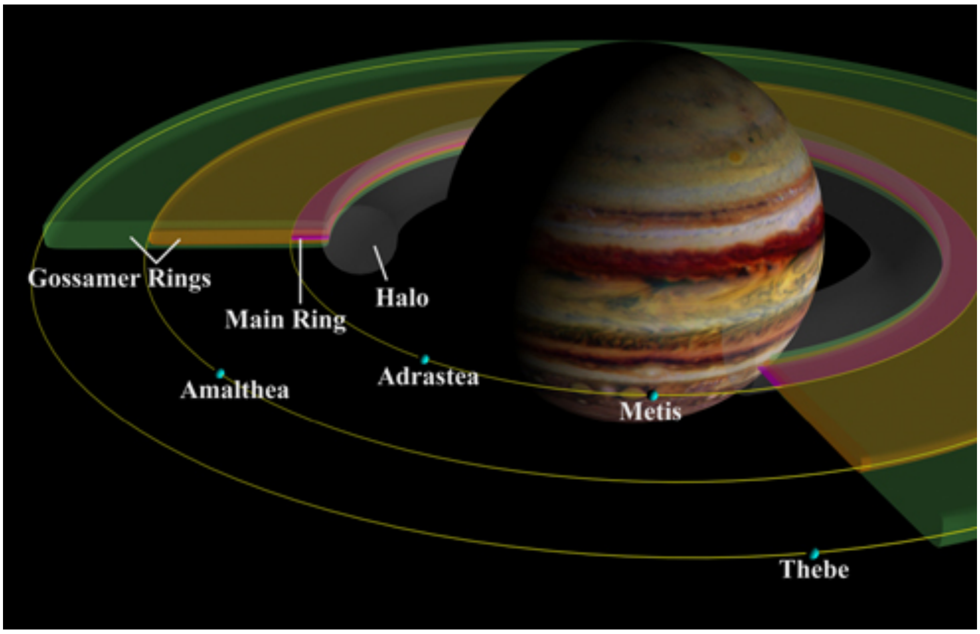

Figure 2.5 Jupiter inner moons and rings system (Burns *et al.*, 2004).

The Galilean moons are named Io, Europa, Ganymede and Callisto. They are the largest natural satellites of Jupiter and concentrate most of the mass of the moons system. This group of moons is characterized by a complex geology (Bagenal *et al.*, 2004).

Io is the most volcanically active body of the solar system. The strong tidal heating aliments the volcanic process. Io is supposed to be composed by a silicate crust and mantle with an iron rich metallic core. The magnetic field of Jupiter induces a magnetic field in the Io melted mantle. The absence of an intrinsic magnetic field suggests a non-convecting core (Bagenal *et al.*, 2004).

Europa has an ice crust characterized by intense tectonism that produces a fast resurfacing. The presence of an induced magnetic field requires a liquid water shell beneath the ice crust. The mantle is composed by silicate while the core is metallic even if its size and composition is unknown (Bagenal *et al.*, 2004).

Ganymede is the largest moon of the system. It is the only Galilean moon which show an intrinsic magnetic field that must be alimented by a dynamo in the liquid iron-rich core. The ice crust is characterized by tectonic resurfacing but the presence of impact craters suggest that the resurfacing is slower than for Europa. Between the ice crust and the silicate mantle there is a liquid water layer (Bagenal *et al.*, 2004).

The surface of Callisto shows many impact craters that are an index of slow resurfacing. The induced magnetic field requires a water layer beneath the ice crust (Bagenal *et al.*, 2004).

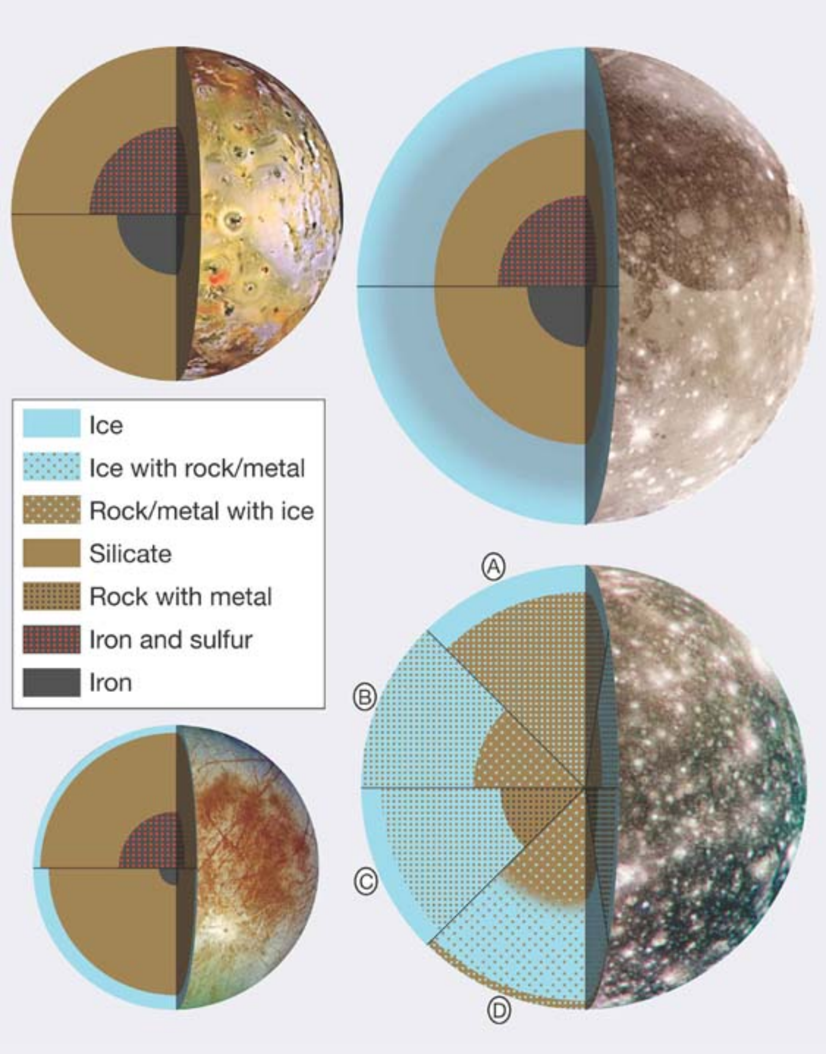

Figure 2.6 Possible models for the interior structure of the Galilean moons. Top left is Io, bottom left is Europa, top right is Ganymede and bottom right is Callisto (Bagenal *et al.*, 2004).

The group of the irregular moons is composed by a large variety of small bodies whose orbits are characterized by large semi-major axis and eccentricity. They divide in two main classes: prograde and retrograde.

3 Orbit determination techniques

3.1 Radiometric observables

The measurement of the spacecraft position and velocity is carried out by means of a tracking system, which measures the properties of the radio signal travelling from the transmitter to the receiver. The role of transmitter and receiver may be taken from the ground station or from the spacecraft telecommunication system depending on the chosen operative mode (Montenbruck *et al.*, 2000).

If the link consists only of a downlink signal from the spacecraft to the ground station the observable is called *one-way*. Alternatively, the ground station irradiates a radio signal towards to the spacecraft, which receives and retransmits it to the same ground station in *two-way* mode. For missions to the outer solar system may occur that the round trip travelling time between the ground station and the spacecraft is greater than the visibility period from the ground station. Therefore the returning signal is received not by the ground station transmitting the signal but from a second one (*three-way* mode) (Montenbruck *et al.*, 2000).

The radiometric observables divide in three main categories (Montenbruck *et al.*, 2000):

- Angular observables
- Range observables
- Range-rate observables.

The Juno mission tracking system will use only two-way range and range-rate observables. During Ka-band tracking only range-rate measurements will be collected.

3.1.1 Two-way Range observables

3.1.1.1 Multi-tone ranging

The two-way range observable is a measurement of the round trip light time of a signal emitted from the ground station to the spacecraft and transmitted back to the station.

The ranging signal modulated onto the carrier is substantially a sine wave:

$$s_t = A\sin\left(2\pi f_0 t\right)$$

When the signal is received at the ground station it is demodulated by the ranging demodulator and the phase of the incoming tone is compared to the phase of the outgoing one. The received phase will result shifted by a quantity dependent by the distance travelled by the signal (Montenbruck *et al.*, 2000).

$$s_r = A\sin\left(2\pi f_0\left(t - \frac{2\rho}{c}\right)\right)$$

The phase difference is proportional to the round trip light time.

$$\Delta\Phi = 2\pi f_0 \frac{2\rho}{c}$$

$$RTLT = \frac{2\rho}{c} = \frac{\Delta\Phi}{2\pi f_0}$$

The phase shift can only be measured in an interval $\left[0,2\pi\right]$ therefore ambiguity problems arise when converting from phase to range. To solve the ambiguities minor tones derived from the major tone are coherently modulated onto the carrier. Considering that the accuracy in the phase determination is independent by frequency, the shortest wavelength defines the range accuracy while the low frequency tones resolve the ambiguities (Montenbruck *et al.*, 2000).

3.1.1.2 *Pseudo-noise code ranging*

An alternative to multi-tone ranging is to modulate onto the carrier a random-like binary code. The code is repeated after a predefined number of bits known as *code length*. When the signal is received and demodulated by the ground station and the received code is correlated with a replica of the uplink code, to determine the phase shifting. The *chip length* gives the accuracy in the range determination while the code length resolves the ambiguities (Montenbruck *et al.*, 2000).

3.1.2 Two-way Range-rate observables

The two-way range-rate observable is a measurement of the Doppler shift of a signal. The signal is transmitted from the ground station at a frequency f_T and it is received by the spacecraft with a certain Doppler shift due to the relative motion of the two participants. The onboard transponder coherently transmits it back with a frequency multiple of the received one (turn-around ratio T) in order to avoid interference with the incoming wave. When the signal is finally received at the ground station at a frequency f_R. The received frequency is mixed with a reference frequency and a low pass filter returns the Doppler frequency $f_r - f_{ref}$ (Montenbruck *et al.*, 2000).

The Doppler shift cannot be measured instantaneously, but it is instead measured by counting the accumulated cycles of zero-crossings over a count time T_c. The observable built in this way is the Integrated Doppler which is different by the instantaneous Doppler (Montenbruck *et al.*, 2000).

The number of cycles the Doppler frequency accumulates in a count time interval $T_c = [t_1, t_2]$ is

$$N = \int_{t_1}^{t_2} \left(f_R - f_{ref} \right) dt$$

The reference frequency is assumed constant over the count time interval and proportional to the transmitted frequency.

$$f_{ref} = Tf_T$$

The received frequency can be approximated as

$$f_R = Tf_T \left(1 - \frac{2\bar{\dot{\rho}}}{c} \right)$$

where $\bar{\dot{\rho}}$ is the average range-rate over the count time.

The cycles count is rewritten as

$$N = \int_{t_1}^{t_2} \left[Tf_T \left(1 - \frac{2\bar{\dot{\rho}}}{c} \right) - Tf_T \right] dt = -\int_{t_1}^{t_2} Tf_T \frac{2\bar{\dot{\rho}}}{c} dt = -Tf_T \frac{2\bar{\dot{\rho}}}{c} \left(t_2 - t_1 \right) = -Tf_T \frac{2\bar{\dot{\rho}}}{c} T_c$$

The average range-rate is therefore related to the cycles count

$$\bar{\dot{\rho}} = -\frac{1}{2} \frac{Nc}{Tf_T T_c} .$$

3.2 Instrumentation

3.2.1 Onboard instrumentation

The instrument enabling the high accuracy measurements of the Juno gravity science experiment is the onboard Ka-band translator (Simone *et al.*, 2009).

The instrument is able to receive a radio signal from the ground station and transpond it back to the station in coherent mode. It is characterized by a high frequency stability which allows high accuracy Doppler measurements ($3\,\mu m/s$ at 1000 s integration time).

The modules composing the Kat are:

- Receiver analog module
- Digital module
- Transmitter analog module
- Baseplate module

A 3D view of the instruments and the functional block diagram are reported:

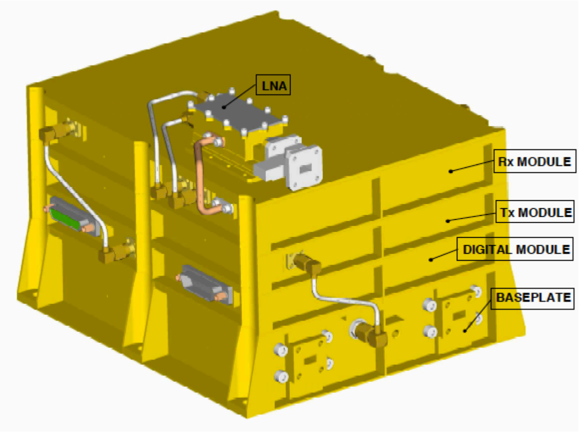

Figure 3.1. KaT 3D model (Simone *et al.*, 2009).

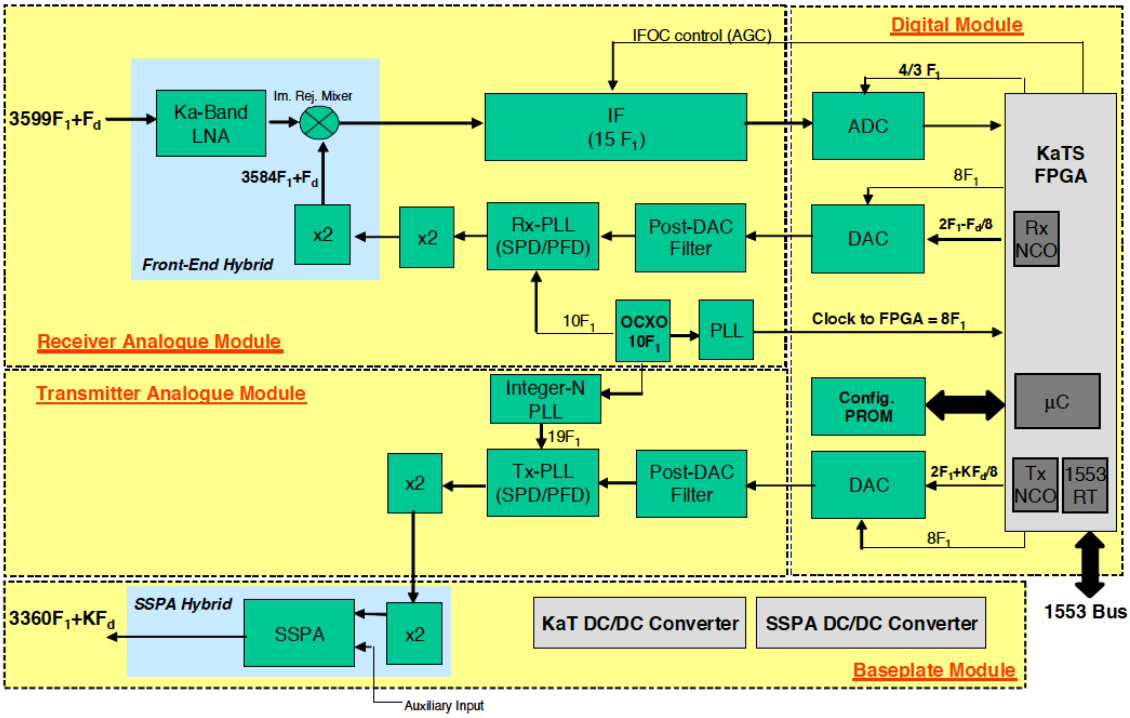

Figure 3.2. KaT top-level block diagram (Simone *et al.*, 2009).

The frequency plan is based on a particular Phase-Locked Loop (PLL) called Flexible PLL.

The internal frequency reference is given by an Oven Controlled Quartz Oscillator (OCXO).

The KaT characteristics are:

Figure	Specification	Test Results	Notes
Turn-around ratio	3360/3599		
Acquisition Threshold	-130 dBm @ 4 kHz/s	-132 dBm	
Tracking threshold	-135 dBm @ 1.2 kHz/s	-139 dBm	
Tracking Range	±3MHz	> ± 7 MHz	
Noise Figure	< 5 dB	≤4 dB	
Output Power	34 dBm @ 32 GHz	34.5 dBm	

Allan Deviation			
- **1 sec**	10^{-13} (goal)	$3.04 \cdot 10^{-13}$	Measured @ -130 dBm
- **10 sec**	10^{-14} (goal)	$3.11 \cdot 10^{-14}$	
- **100 sec**	$4 \cdot 10^{-15}$	$3.08 \cdot 10^{-15}$	
- **1000 sec**	$4 \cdot 10^{-16}$	----	

Table 3.1. KaT performance test results (Simone *et al.*, 2009).

The instrument has been manufactured by Thales Alenia Space – Italy (TAS-I) and funded by the Italian Space Agency (ASI).

3.2.2 On ground instrumentation

When close to pericenter, the Juno spacecraft will be tracked from DSS-25 (NASA – DSN). It is located at the Apollo site of the Goldstone Deep Space Communication Complex in Fort Irwin, California.

Figure 3.3. DSS-25, Goldstone Deep Space Communication Complex, Fort Irwin (CA).

DSS-25 is *34-m beam waveguide (BWG) antenna* and its design and basic performance parameters are similar to those of the *34-m high efficiency (HEF) antenna*. 5 precision radio frequency mirrors reflect the signals along a beam-waveguide from the vertex of the antenna to the underground equipment room (deepspace.jpl.nasa.gov, 2006).

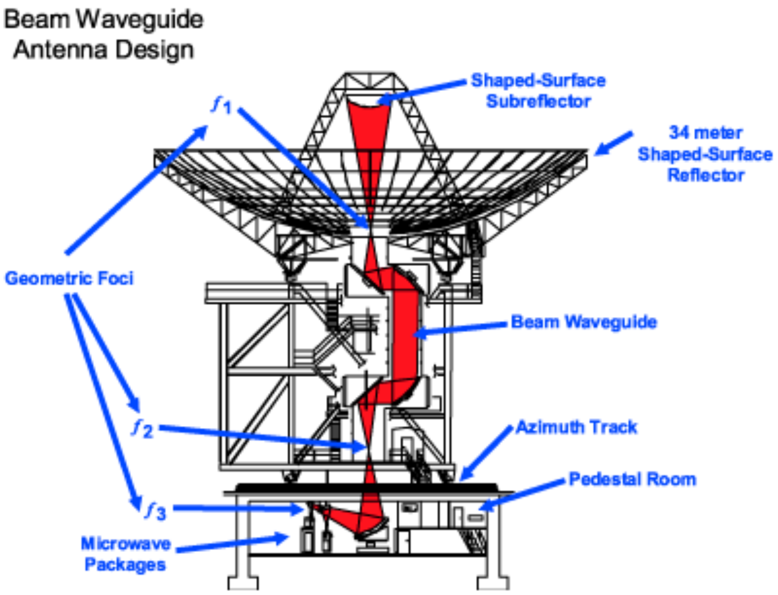

Figure 3.4. 34-m BWG antenna design (deepspace.jpl.nasa.gov, 2006).

This station is also equipped with an Advanced Media Calibration System (AMC), which provides calibration of the dry and wet component of the troposphere. The system includes water vapor radiometers, digital pressure sensors and microwave temperature profilers, which are symmetrically installed at short distance from the antenna (Tortora *et al.*, 2004).

Figure 3.5. Advenced Media Calibration System - Water Vapour Radiometer at DSS-25.

3.3 Error budget for the Juno mission

Radiometric measurements are affected by several noise sources. It is important to quantify the error expected on the observables (error budget) in order to faithfully reproduce the results of the experiment.

The gravity experiment of the Juno mission will be carried out using range-rate measurements only, therefore the link budget will focus on the Doppler observable. The disturbances on the Doppler signal are due to instrumental noises, propagation noises and systematic errors.

The instrumental noises are random errors introduced by the on-ground and the onboard instrumentation.

An electromagnetic signal propagating trough a media with random refractive index fluctuations undergoes a change of direction and velocity propagation, which reflects on the signal phase, frequency and polarization (Asmar, 2005).

Possible systematic effects are due to a residual orbital signature or biases in the calibrations.

The signal and the noises enter the observation with different transfer functions depending on the Doppler mode (one/two/three-way). The observation are represented by a time series y(t) of fractional Doppler fluctuations, that is the change in frequency between the received and reference signal, divided by the nominal frequency of the Doppler link.

$$y(t) = \frac{\Delta f(t)}{f_0}.$$

The index chosen to represent the frequency stability of the radio signal is the Allan variance, which is a time domain measure of fractional frequency fluctuation as a function of averaging time (τ).

$$\sigma_y^2(t) = \frac{1}{2}\left\langle \left| \overline{y(t)} - \overline{y(t+\tau)} \right|^2 \right\rangle = \int_{-\infty}^{+\infty} 2S_y(f) \frac{\sin^4(\pi f \tau)}{(\pi f \tau)^2} df$$

with

$$\overline{y(t)} = \int_{t'}^{t'+t} y(t')dt'$$

$S_y(f)$ is the power spectral density of the fluctuations (Asmar, 2005).

Usually it is a function of the kind $S_y(f) = hf^{\alpha}$.

Section 3.3.1 contains an operative computation of the expected noise for the Juno radio link.

3.3.1 Instrumental noise

The power input at the receiving antenna can be computed using the following equation:

$$P_{RX} = \frac{EIRP \cdot G_{RX}}{L_{ATM} L_{FS} L_P L_C L_{POL}}$$

where

$EIRP = P_{TX} G_{TX}$	Equivalent Isotropically Radiated Power
P_{TX}	Transmitted Power
G_{TX}	Transmitting antenna gain
G_{RX}	Receiving antenna gain
L_{ATM}	Atmospheric attenuation
L_{FS}	Free space attenuation

L_P	Pointing loss
L_C	Circuit loss
L_{POL}	Polarization loss.

The antenna gain is defined as

$$G = \eta \left(\frac{\pi D}{\lambda} \right)^2$$

where

η	Antenna efficiency
D	Antenna diameter
λ	Signal wavelength

Free space losses depend on the distance between the two antennas.

$$L_{FS} = \left(\frac{4\pi R}{\lambda} \right)^2$$

The power associated to the disturbing noise is expressed by

$$N = K T_{SYS} B = N_0 B$$

where

N	Noise power
$K = 1.38 \cdot 10^{-23}\ J/K$	Boltzmann constant
T_{SYS}	System temperature
B	Instrument bandwidth
N_0	Noise power density

The SNR is the ratio between received and noise power P_{RX}/N_0 .

Uplink frequency	34.4	GHz	
Downlink frequency	32	GHz	
Uplink wavelength	8.7	mm	
Downlink wavelength	9.4	mm	
Ground Station			
Tx Power	755	W	(Slobin, 2010)
Antenna diameter	34	M	(Slobin, 2010)
Antenna efficiency	0.6		
System noise temperature	39.62	K	(Slobin, 2010)
PLL Bandwidth	0.1	Hz	
Spacecraft			
Antenna diameter	2.5	m	
Antenna efficiency	0.6		
Tx Power	2.5	W	(Simone *et al.*, 2009)
Distance from the Earth	6	AU	
System noise temperature	300	K	TAS-I
PLL bandwidth	1	Hz	TAS-I

Table 3.2. Radio link input data.

3.3.1.1 Uplink

Using the equations in section 3.3.1 with the inputs of Table 3.2 it is possible to evaluate the link budget for the uplink leg.

Ground Station		
Tx Power	28.78	dBW
Antenna gain	79.54	dBi

EIRP	108.32	dBW	
Polarization loss	0.08	dB	
Pointing loss	0.12	dB	(Slobin, 2010)

Propagation loss			
Free Space loss	302.22	dB	
Atmospheric attenuation	0.37	dB	(Slobin, 2010)

Spacecraft		
Antenna gain	56.87	dBi
Circuit loss	1.69	dB
Pointing loss	0.2	dB
System noise temperature	24.77	dBK
Received Power	-139.49	dBW
Noise Power density	-203.83	dB
SNR	64.34	dBHz

Table 3.3. DSS25 - Juno HGA link budget (uplink).

3.3.1.2 *Downlink*

Spacecraft			
Tx Power	3.98	dBW	
Antenna gain	56.24	dBi	
EIRP	60.22	dBW	
Circuit loss	1.69	dB	
Pointing loss	0.2	dB	(Slobin, 2010)

Propagation loss		
Free Space loss	301.59	dB

Atmospheric attenuation	0.37	dB	(Slobin, 2010)

Ground station			
Antenna gain	78.91	dBi	
Polarization loss	0.08	dB	
Antenna axial ratio	1	dB	(Slobin, 2010)
Pointing loss	0.12		
System noise temperature	15.98	dBK	
Received Power	-165.92	dBW	
Noise Power density	-212.63	dB	
SNR	46.71	dBHz	

Table 3.4. Juno HGA - DSS25 link budget (downlink).

3.3.2 Troposphere

The troposphere is a portion of the Earth atmosphere extending from sea level to approximately 42 km. It is composed mostly by neutral gas and the fluctuations of the refractive index are due mostly to temperature, pressure and partial pressure of water vapor.

At microwaves frequencies the troposphere is a non-dispersive medium hence the refractive index does not depend on the frequency of the signal.

Tropospheric refraction has two components: A dry component due to dry air contribution and a wet component due to water vapor.

Long period observations of the tropospheric refractive index show a seasonal fluctuation of the wet component. Fluctuations are larger in summer daytime and smallest in winter nighttime (Asmar, 2005).

The wet component effect can be removed at the level of nearly 90%, using the Advanced Media Calibration (AMC) instrumentation (Resch *et al.*, 2002;Tanner, 2003), which is substantially based on the use of water vapor radiometers.

The calibration of the dry part of the troposphere base on (Asmar, 2005)

- Surface metrology
- Assumption that the atmosphere is in hydrostatic equilibrium
- Elevation dependent model of dry component

	Allan dev (1000 s) 2-way
Tropospheric scintillation (winter night)	$1.3\cdot 10^{-14} \div 4.3\cdot 10^{-14}$
Tropospheric scintillation after AMC	$3.2\cdot 10^{-15}$

Table 3.5 Tropospheric noise contribution (Asmar, 2005).

3.3.3 Ionosphere

The ionosphere is a layer of the atmosphere extending from 50 km up to 1000 km. It is composed of plasma of ions and free electrons, generated by the absorption of the solar ultraviolet radiation.

Free electrons play a key role in the fluctuations of the refractive index of the ionosphere. The electrons concentration increases with height, as the solar radiation is stronger. The maximum is located at 300 km. After this point the concentration decreases due to the reduction of the atmospheric density. Seasonal and diurnal variations affect the electron density profile.

A simplified model of the ionospheric refractive indices leads to (Jeske 1988)

$$n_{ph} \approx 1 - \frac{1}{2}\frac{f_p^2}{f^2} \quad ; \quad n_{gr} \approx 1 + \frac{1}{2}\frac{f_p^2}{f^2}$$

with

$$f_p = \frac{1}{2\pi}\sqrt{\frac{d_e e_0^2}{m_e \varepsilon_0}}$$

where

f_p	plasma frequency
d_e	electron number density
e_0	electron charge
m_e	electron mass
ε_0	vacuum dielectric constant

The total electron content (TEC) is defined as the integral of the electron number density along the line of sight (observer – spacecraft direction).

$$TEC = \int_S^O d_e(s)\,ds$$

It is expressed in $TECU = 10^{16} m^{-2}$.

The range correction due to ionospheric refraction is

$$\Delta\rho = \int_S^O \left(n_{gr} - 1\right) ds = \frac{40.3 \cdot TEC}{f^2}$$

while the signal phase correction is

$$\frac{\Delta\phi}{2\pi}\lambda = \int_S^O \left(n_{ph} - 1\right) ds = -\frac{40.3 \cdot TEC}{f^2}$$

Since global ionospheric models do not provide the sufficient calibration accuracy, it is important to locally measure the total electron content.

The corrections become weaker as the frequency of the signal increases (Ka-band is more convenient than S or X band). Being a dispersive medium, the ionosphere allows its complete calibration by the use of multifrequency links.

In the Juno case the link will be Ka-band only. The effect of the ionosphere is limited but not completely removed.

3.3.4 Interplanetary plasma

The Sun continuously ejects charged particles in the outer space. The particles interact with the electromagnetic signals propagating in space.

In the solar wind there are density fluctuations that, convected by the solar wind speed cross the line between the signal source and the receiver. The solar wind density fluctuations cause random fluctuations of the refractive index. The only component of the solar wind speed affecting the signal is the component perpendicular to the line of sight (Iess *et al.*, 1983). There is clearly a dependence on the relative position of solar wind source, the Earth station and the spacecraft. The relative position is expressed by the Elongation angle or, in the outer solar system Sun-Earth-Probe (SEP) angle.

The interplanetary plasma is a dispersive medium therefore the effect on the signal depends on the frequency.

As for the ionosphere the dependency on the frequency is $\frac{1}{f^2}$, hence at Ka-band the plasma contribution is 16 time smaller than at X-band (Asmar, 2005).

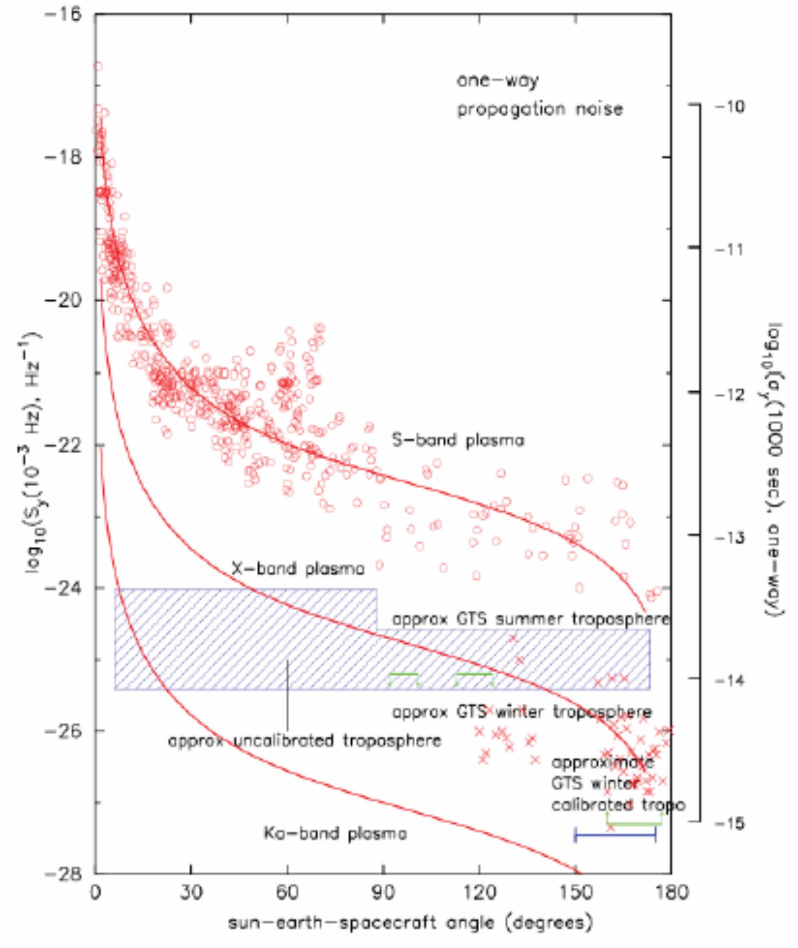

Figure 3.6. Power spectral density of proplasma phase scintillation at f=0.001 Hz versus SEP angle (red circles and crosses), approximate level of uncalibrated tropospheric scintillation noise (blue) and limits to antenna mechanical noise (green) (Asmar, 2005).

The right hand scale of Figure 3.6 is the equivalent Allan deviation at 1000 s integration time.

The interplanetary plasma scintillation can be completely calibrated by means of a multifrequency link, as already done during the Cassini Solar Conjunction Experiment in 2002, using a triple link X/X, X/Ka, Ka/Ka. A dual frequency link allows plasma removal at a level of 75%.

3.3.5 Error budget summary

The following tables summarize the noise sources descripted in the previous section

Type	$\sigma_y(1000s)$ **two-way**	α	h	**Reference**
Media				
Troposphere (with AMC) nominal	$3.2\cdot 10^{-15}$	-2/5	$9.8\cdot 10^{-28}$	
Troposphere minimum (without AMC)	$1.4\cdot 10^{-14}$	-2/5	$4.7\cdot 10^{-27}$	
Plasma/ionosphere (SEP = 30°)	$4.7\cdot 10^{-15}$	-2/3	$1.1\cdot 10^{-27}$	
Plasma/ionosphere (SEP = 150°)	$1.4\cdot 10^{-15}$	-2/3	$1.1\cdot 10^{-31}$	
Ground Segment				
Antenna wind loading	$2.2\cdot 10^{-15}$	0	$2.3\cdot 10^{-26}$	
Antenna gravity deflection	$4.7\cdot 10^{-16}$	0	$1.8\cdot 10^{-25}$	
Antenna thermal deformation	$3.7\cdot 10^{-15}$	0		
BWG mirror deformation	$1.7\cdot 10^{-15}$	0		
Frequency standard	$1.0\cdot 10^{-15}$	0		
Ground receiving chain	$2.3\cdot 10^{-17}$	2		
Ground transmitting chain	$5.7\cdot 10^{-17}$	2		
Spacecraft Segment				
KaT and onboard amplifiers	$4.0\cdot 10^{-16}$	2	$5.8\cdot 10^{-30}$	
Antenna System	$5.0\cdot 10^{-17}$	0	$3.6\cdot 10^{-28}$	
Diplexer and Triplexer	$2.3\cdot 10^{-17}$	2		
Passive RF components (waveguides)	$1.6\cdot 10^{-15}$	0		
OD system				
Station location, Earth tides and polar motion	$8.0\cdot 10^{-16}$		$2.5\cdot 10^{-28}$ @ $1.16\cdot 10^{-5}$ Hz	

Total RSS best **(SEP = 150°; calibrated troposphere)**	$6.2 \cdot 10^{-15}$
Total RSS worst **(SEP = 30°; uncalibrated troposphere)**	$1.6 \cdot 10^{-14}$

Table 3.6. Error budget summary for the Juno mission

The estimate of the total end-to-end Allan variance has been obtained by summing the variances from all the contributions.

The total expected power spectral density for the best and worst case are

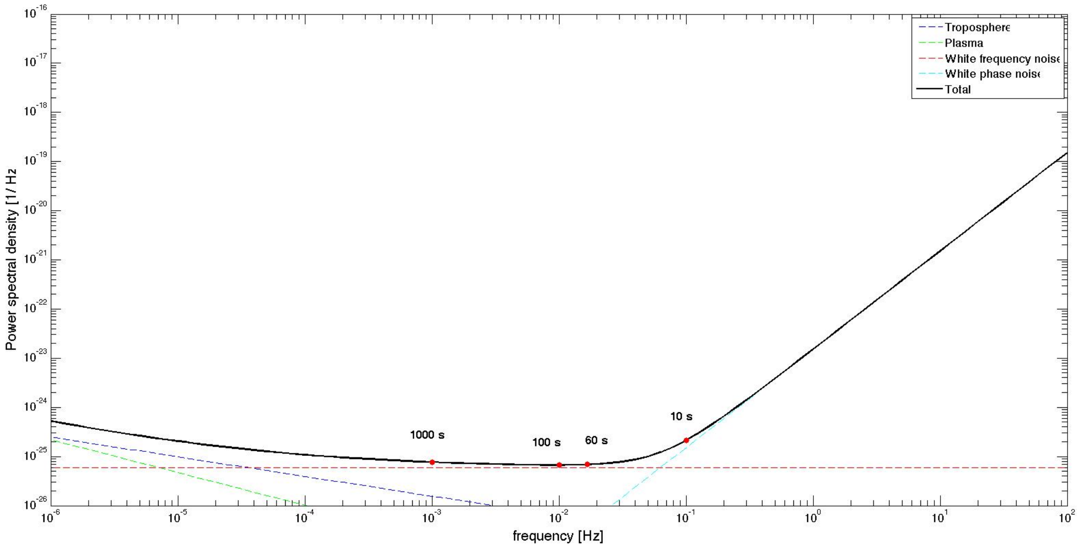

Figure 3.7. Doppler residuals expected power spectral density – best case.

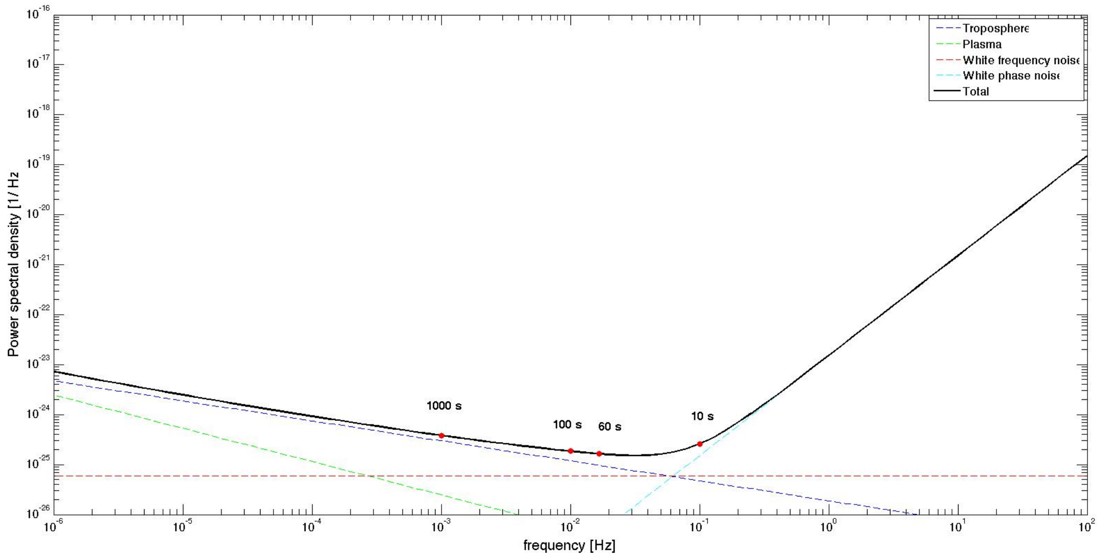

Figure 3.8. Doppler residuals expected power spectral density - worst case.

The Doppler integration time will be 60 s. This region of the spectrum is not dominated by thermal noise. Thermal noise will not significantly affect the gravity measurements.

The 60 s Allan deviations for best and worst case are

Case	$\sigma_y(1000s)$	$\sigma_y(60s)$
Best	$6.2\cdot10^{-15}$	$2.3\cdot10^{-14}$
Worst	$1.6\cdot10^{-14}$	$4.0\cdot10^{-14}$

Table 3.7 Best and worst case allan deviation for 60 s and 1000 s integration time.

3.4 Orbit determination problem

The accurate determination of a spacecraft orbit is crucial problem in space missions. The mission operations have to rely on an affordable reconstruction of the spacecraft trajectory to plan maneuvers and observations.

The classical orbit determination problem based on the assumption that the bodies move along keplerian trajectories (conics), that is under the only influence of the gravity of a central body, determining the evolution of their motion.

A keplerian conic is defined by 6 parameters, were they the body position (3 parameters) and velocity (3 parameters) at a given epoch or the 6 classical elements (semi-major axis, inclination, eccentricity, right ascension of the ascending node, argument of pericenter and mean anomaly at a given epoch).

The problem can be solved by realizing 6 observations of the body state vector and therefore solving a determined system of 6 equations in six unknowns.

The motion of a celestial body (planet or satellite) is generally closely approximated by a keplerian orbit, but this is not true for other bodies such as artificial satellites or asteroids. In these cases the equations of motion depart significantly from the central body law. Non-gravitational accelerations and the gravity corrections due to asphericity of the central body or to third body effects start to play a key role.

The equation of motion is therefore more complicated and the analytical solution is generally not available. It is therefore necessary to approximate the dynamics of the problem (usually linearizing). Even in this case the problem can be solved iteratively having the availability of a number of observables equal to the number of parameters and an initial guess solution close enough to the actual one.

This approach neglects the fact that the observations are not perfect but are affected by random and systematic errors characterized by a certain statistics. Moreover, also the knowledge of the dynamics regulating the trajectory propagation is not perfect.

The errors are, as a matter of fact, additional unknowns of the system. Being *m* the number of observations and *n* the dimension of the state vector, there are m equations for *m* + *n* unknowns and the system results to be always underdetermined (Tapley *et al.,* 2004, p.12).

A statistical approach is needed to obtain the solution which best approximate the actual one. This solution is not coincident with the actual trajectory, but is the best approximation on the basis of the observational data.

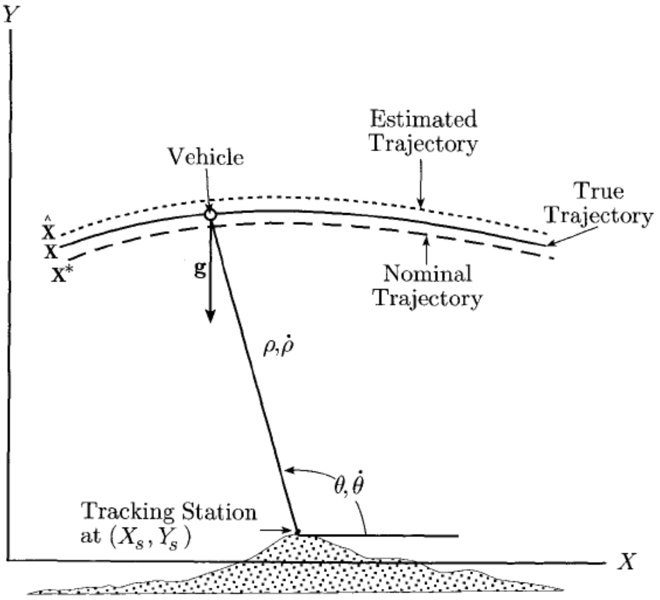

Figure 3.9. Orbit determination problem schematics. The nominal trajectory is the first guess solution required by the iterative solution method (Tapley *et al.*, 2004, fig.1.2.1).

3.4.1 Mathematical formulation

The following mathematical formulation is based on Chapter 4 of (Tapley *et al.*, 2004).

The differential equation regulating the spacecraft dynamics is a non-linear function of state and time

$$\dot{X}(t) = F(X(t), t) \qquad X_k = X(t_k)$$

where $X(t)$ is the spacecraft state vector (position and velocity). The minimal set of parameters constituting the state vector is the spacecraft state and velocity. It can be expanded to include model parameters, e.g. the central body GM.

Real observations are non-linearly dependent by the state and time and are corrupted by random errors.

$$Y(t_i) = G(X(t_i), t_i) + \varepsilon(t_i) \qquad i = 1,2,\ldots,l \quad ; \quad \varepsilon_k = \varepsilon(t_k)$$

where t_i are the observation epochs, Y is the actual observation (observed observable), G is a model of the observable in terms of the state vector of the spacecraft and ε is the observation error.

This two set of equations can be expanded in a Taylor series arrested at the first order about a nominal known trajectory $X_*(t)$ (time dependence from time omitted for the sake of clarity):

$$\dot{X} = F(X_*, t) + \left(\frac{\partial F}{\partial X}\right)_* (X - X_*) + o\left((X - X_*)^2\right) \approx F(X_*, t) + \left(\frac{\partial F}{\partial X}\right)_* (X - X_*).$$

This expression can be rewritten in terms of the trajectory correction $x = X - X_*$:

$$\dot{X}_* = F(X_*, t)$$
$$\dot{x} = \left(\frac{\partial F}{\partial X}\right)_* x = Ax$$

where $A = \left(\frac{\partial F}{\partial X}\right)_*$ is the square matrix of the partial derivatives of the dynamics with respect to the spacecraft trajectory.

The solution of the differential equation has the form

$$x(t) = \Phi(t_0, t) x_0 \qquad ; \qquad x_0 = x(t_0)$$

$$X(t) = X_*(t) + \Phi(t_0, t)\left(X(t_0) - X_*(t_0)\right)$$

$\Phi(t_0,t)$ is an n-by-n matrix linearly linking the state at a given epoch t_0 to the state at a general epoch t. It takes the name of *state transition matrix*.

This matrix enjoys the following properties

1. $\Phi(t_0,t_0) = I$
2. $\Phi^{-1}(t_0,t) = \Phi(t,t_0)$
3. $\Phi(t_1,t_2)\Phi(t_0,t_1) = \Phi(t_0,t_2)$

Even the observation equations are linearized about the nominal trajectory and expressed in terms of observation residuals vector y:

$$Y_i \approx G(X_{*i},t_i) + \left(\frac{\partial G}{\partial X}\right)_{*i}(X_i - X_{*i}) + \varepsilon_i \quad ; \qquad Y_{*i} = G(X_{*i},t_i)$$

$$y_i = \tilde{H}_i x_i + \varepsilon_i \qquad\qquad i = 1,\ldots,l$$

where $\tilde{H}$ is a 1-by-n *mapping matrix*, Y_{*i} is the observable computed on the nominal trajectory X_* at epoch t_i (*computed observable*).

Each residual can be expressed in terms of the state vector of the spacecraft at the epoch $t = t_0$

$$y_i = \tilde{H}_i \Phi(t_0,t_i) x_0 + \varepsilon_i = H_i x_0 + \varepsilon_i \qquad\qquad i = 1,\ldots,l$$

rewriting everything in matrix form

$$y = \begin{bmatrix} y_1 \\ \vdots \\ y_l \end{bmatrix} = \begin{bmatrix} [\quad H_1 \quad] \\ \vdots \\ [\quad H_l \quad] \end{bmatrix} x_0 + \begin{bmatrix} \varepsilon_1 \\ \vdots \\ \varepsilon_l \end{bmatrix} = Hx_0 + \varepsilon\,.$$

H takes the name of *normal matrix* and contains the partial derivatives of the observables with respect to x_0, y is the residuals vector and ε is the observation error vector.

The objective of the statistical orbit determination is to find the correction x_0, which minimizes a certain cost function of the observation errors. Propagating the estimated correction $\hat{x}_0$, it is possible to get the trajectory best approximating the actual trajectory followed by the spacecraft at each time.

The observation error statistics is assumed a priori to be white Gaussian, therefore

$$E(\varepsilon)=0 \qquad ; \qquad E\left(\varepsilon^T\varepsilon\right)=\begin{bmatrix} \sigma_1^2 & \cdots & 0 \\ \vdots & \ddots & \vdots \\ 0 & \cdots & \sigma_l^2 \end{bmatrix}=R$$

This means that the observation error distribution is zero mean and that errors at different times are not correlated.

It is now time to introduce the concept that the observables are not equally accurate. Each observable has to be weighted differently in regard of its intrinsic accuracy:

$$W^{1/2}y=W^{1/2}Hx_0+W^{1/2}\varepsilon \qquad\qquad W^{1/2}=R^{-1/2}=\begin{bmatrix} 1/\sigma_1 & \cdots & 0 \\ \vdots & \ddots & \vdots \\ 0 & \cdots & 1/\sigma_l \end{bmatrix}$$

It is straightforward that the smaller the standard deviation associated to an observable, the larger its weight is.

The cost function to be minimized is the sum of the squares of the observation errors, taking into account the relative weights (*weighted least squares filter*):

$$J=\frac{1}{2}\varepsilon^T W\varepsilon \qquad ; \qquad W=\begin{bmatrix} 1/\sigma_1^2 & \cdots & 0 \\ \vdots & \ddots & \vdots \\ 0 & \cdots & 1/\sigma_l^2 \end{bmatrix}$$

where W is called *weighting matrix*.

The cost function can be expressed as function of the unknown correction x_0:

$$J(x_0)=\frac{1}{2}(y-Hx_0)^T W(y-Hx_0)=\frac{1}{2}\left(y^T Wy-x_0^T H^T Wy-y^T WHx_0+x_0^T H^T WHx_0\right)$$

to get the minimum of the function :

$$\frac{\partial J(x_0)}{\partial x_0}=-H^T Wy+H^T WHx_0=0$$

The correction satisfying this constraint is the best estimate :

$$\hat{x}_0=\left(H^T WH\right)^{-1} H^T Wy\,.$$

Usually an a priori solution $\overline{x}_0$ with a certain associated covariance matrix $\overline{P}$ is available. The a priori information is useful in order to better condition the solution avoiding symmetries intrinsic in the non-linearity of the problem.

The cost function expression is slightly different from the previous case, since it contains a penalty for the solution departing significantly from the a priori one.

$$J(x_0)=\frac{1}{2}(y-Hx_0)^T W(y-Hx_0)+\frac{1}{2}(x_0-\overline{x}_0)^T \overline{P}^{-1}(x_0-\overline{x}_0)$$

$$\hat{x}_0=\left(H^T WH+\overline{P}^{-1}\right)^{-1}\left(H^T Wy+\overline{P}^{-1}\overline{x}_0\right)$$

The a priori covariance matrix of the a priori solution plays a key role. If its element are too large, the a priori solution loses its conditioning of the solution. On the other hand, if its elements are too small they will tend to overcome the information content coming from the data and the estimate will result bonded to the a priori solution.

The matrix $\left(H^T WH+\overline{P}^{-1}\right)$ is called *information matrix*. Thanks to the assumption made on the weighting matrix, it is easy to demonstrate that the inverse of the information matrix, $P=\left(H^T WH+\overline{P}^{-1}\right)^{-1}$, is the *covariance matrix* associated to the estimated solution.

At this point, the trajectory propagated from the estimated correction can be used as a new nominal trajectory and the whole process can be iterated until convergence occurs.

3.4.2 Consider parameters

The consider parameters is a set of model parameters which are not included in the estimated parameters vector. Their value is characterized by an uncertainty that can influence the uncertainty associated to the estimated parameters.

The equation of the least squares filter must be adapted. In the following equations the subscript x indicates quantities relative to the estimated parameter while the subscript c is for consider parameters quantities. The formulation for consider parameters is from Chapter 6 of (Tapley *et al.*, 2004).

Assume a given set of a priori deviations for the consider parameter, $\bar{c}$, and the relative a priori uncertainty, $\bar{P}_{cc}$, is given

$$
\begin{aligned}
&y = H_x x + H_c \bar{c} + \varepsilon \quad ; \quad P_x = \left(H_x^T W H_x + \bar{P}_x^{-1}\right) \quad ; \quad S_{xc} = P_x^{-1} H_x^T W H_c \\
&\hat{x} = P_x^{-1}\left(H_x^T W y + \bar{P}_x^{-1}\bar{x}\right) \\
&\hat{x}_c = \hat{x} + S_{xc}\bar{c} \\
&P_{xx} = P_x + S_{xc}\bar{P}_{cc}S_{xc}^T
\end{aligned}
$$

where $\hat{x}_c$ is the new estimate accounting for the deviation in the consider parameters and P_{xx} is the new covariance matrix including the effect of the uncertainties in $\bar{P}_{cc}$.

The matrix S_{xc} is called *sensitivity matrix*. From the sensitivity matrix it is possible to build the *perturbation matrix*,

$$\Gamma = S_{xc}\, diag\left(\sigma_c\right)$$

which returns the correction to the estimate for a 1 sigma deviation in the consider parameters.

3.4.3 Multiarc approach

Often the observables set is composed by observables collected along arcs of trajectory that are not dynamically coherent. This happens for example in the Juno mission where after each passage at pericenter and outside the Ka-band tracking period there is an orbit trim maneuver (OTM), followed by 11 days in which the spacecraft flies far from the influence of the perturbations of the gravitational field of Jupiter. Integrating a single arc of trajectory requires high accuracy in the modeling of all the perturbations affecting the spacecraft trajectory in the period between two consecutive Ka-band passes. This modeling effort does not add much to the information about the gravity field of Jupiter, that is the object of the investigation.

An alternative approach consists in dividing the trajectory in several arcs, dynamically independent one from the others. Each arc will be characterized by a state vector containing a different initial state vector (*local* parameters) but a common set of model parameters (*global parameters*). This results in an over parametrization of the problem, despite of a loss of accuracy in the determination of the spacecraft positions a velocities since the single arcs are not constrained to belong to a coherent trajectory.

Mathematically, the formulation is similar to the case of the single arc estimation.

For each arc n, the subset of local and global parameters is individuated

$$y_n = H_n x_n + \varepsilon_n \qquad ; \qquad \begin{cases} x_n = \begin{bmatrix} x_{l,n} \\ x_g \end{bmatrix} \\ H = \begin{bmatrix} H_{l,n} & H_{g,n} \end{bmatrix} \end{cases} \qquad n = 1,\ldots,n_{arcs}$$

Rearranging :

$$y = \begin{bmatrix} y_1 \\ \vdots \\ y_{n_{arc}} \end{bmatrix} = \begin{bmatrix} H_{l,1} & 0 & 0 & 0 & H_{g,1} \\ 0 & H_{l,2} & 0 & 0 & H_{g,2} \\ 0 & 0 & \ddots & 0 & \vdots \\ 0 & \cdots & 0 & H_{l,n_{arc}} & H_{g,n_{arc}} \end{bmatrix} \begin{bmatrix} x_{l,1} \\ x_{l,2} \\ \vdots \\ x_{l,n_{arc}} \\ x_g \end{bmatrix} + \begin{bmatrix} \varepsilon_1 \\ \vdots \\ \varepsilon_{n_{arc}} \end{bmatrix} = Hx_0 + \varepsilon \, .$$

The minimization process leads formally to the same results for the best estimate of the parameters vector and its associated covariance.

For the Juno mission it has been chosen to select from the nominal trajectory 25 independent arcs. Each arc starts 12 hours before the closest approach with Jupiter and ends 12 hours after it. The arcs of trajectory contain 1 Ka-band tracking pass each. The multiarc approach will be used selecting as local parameters the Juno position and velocity at the beginning of the arcs, and as global parameters the gravity field coefficients of Jupiter.

3.4.4 Orbit Determination Software

The key tool of the analysis is the NASA-JPL operative software package for interplanetary spacecraft Navigation : DPTRAJ-ODP (Double Precision Trajectory – Orbit Determination Program). It is a collection of routines each fulfilling one of the tasks required in the orbit determination process. The heart of the software is constituted by two particular routines:

- The trajectory and trajectory partials numerical integrator (DIVA)
- The routine for the observables and regression partials computing (REGRES).

The DPTRAJ-ODP least squares filter routine has not be conceived for an extensive use of the multi-arc approach. Therefore the *Laboratorio di Radio Scienza* of *Sapienza, Università di Roma* developed a new routine for the least squares filter, ORACLE, particularly performing if used for multiarc orbit determination.

The operation of comparing the values of two observables to compute the residual and the finite representation of the variable *time* are the principal sources of the numerical noise that the code introduce in the residuals due to the limited number of digits. The necessity to limit this behavior led JPL to the choice to develop a new operative code for navigation, MONTE, which is the code that will be actually used to analyze the Juno tracking data.

The analyses presented in this work have been realized with DPTRAJ-ODP

4 The Juno gravity experiment simulation

The measurement of the gravity anomalies on the surface of Jupiter is one of the main goals of the Juno mission.

In order to find the most efficient estimation strategy, an in depth analysis of the problem must be carried out, identifying the criticalities and the opportunities for further science.

The first step in this process is the realistic simulation of the environmental conditions in which the Juno spacecraft will be at experiment epoch. The accelerations that will significantly affect the spacecraft trajectory must be accurately modeled (cf. Section 4.1).

The second step is to model the radio signal characteristics, reproducing the effective radio link and data quality (cf. Section 4.1.6).

The third step is to find the correct estimation strategy allowing the achievement of the goals established for the experiment. (cf. Section 0)

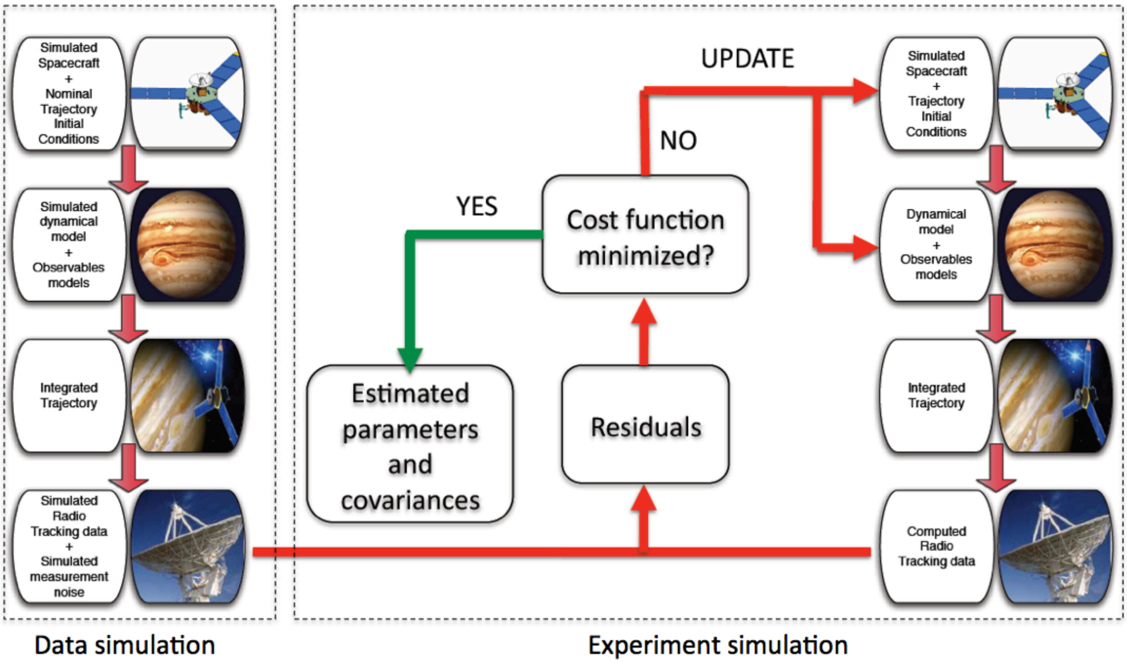

Figure 4.1. Data simulation and experiment simulation process.

4.1 Data Simulation Process

4.1.1 Relevant accelerations

The simulation focuses on the orbital phase of the spacecraft about Jupiter. The arcs of trajectory considered start at one day before the periapsis and end one day after. Therefore only the perturbations that significantly affect the trajectory in these periods are considered. The following table shows the order of magnitude of the most important accelerations at the closest approach with Jupiter.

Gravitational forces are dependent exclusively on the mass of the probe they are acting on.

Gravitational acceleration	**Maximum value (km/s²)**
Jupiter monopole	$2.5 \cdot 10^{-2}$
Jupiter oblateness (J_2)	$4.5 \cdot 10^{-4}$

Galilean satellites monopole	$3.5 \cdot 10^{-7}$
Jupiter tidal deformation (k_2 and k_3)	$6.0 \cdot 10^{-9}$
Lense-Thirring	$1.0 \cdot 10^{-10}$

Table 4.1. Gravitational accelerations order of magnitude at closest approach with Jupiter

Non-gravitational accelerations strongly depend on the surface of the spacecraft they interact with. The large surface of the solar arrays makes Juno particularly sensitive to this kind of forces.

Non-gravitational acceleration	Maximum value (km/s^2)
Solar radiation pressure	$9.0 \cdot 10^{-12}$
Thermal IR planetary emission pressure	$1.2 \cdot 10^{-12}$
Jovian albedo	$6.0 \cdot 10^{-13}$

Table 4.2. Non-gravitational accelerations order of magnitude at closest approach with Jupiter

4.1.2 Nominal Trajectory

The nominal trajectory has been provided by the NASA – Jet Propulsion Laboratory by means of dedicated SPICE kernels to all the scientific teams involved in the Juno project.

In the analysis, the 25 arcs relative to the gravity science pericenters are isolated from the nominal trajectory. The initial conditions are taken at perijove − 12 hours.

4.1.3 Jupiter gravity field simulation

The gravity field of Jupiter, main object of the investigation, is simulated by superimposing the ellipsoidal gravity field and the gravitational figure of the zonal winds for a medium penetration depth (about 1000 km).

The ellipsoidal gravity field is simulated to be exactly what predicted by W.B. Hubbard (Hubbard, 2012). For the zonal winds gravity perturbation Y. Kaspi provided a set of gravity field coefficients computed considering the maximum possible extension in depth. This set of values is the result of the participation of the entire mass of the planet to the zonal winds motion therefore does not represent a realistic scenario. It is adopted as the a priori uncertainty limit for the magnitude of the zonal winds correction. For the simulation of the gravity field it has been chosen to scale this realization by a factor of 1/10.

Only the zonal coefficients are considered in the analysis, since the author has no available prediction for a realistic value of the tesseral and sectoral coefficients at 1000 km depth. The non-zonal contribution is considered to be negligible. Obviously this is a strong hypothesis since it reflects directly onto the number of gravity moments to estimate.

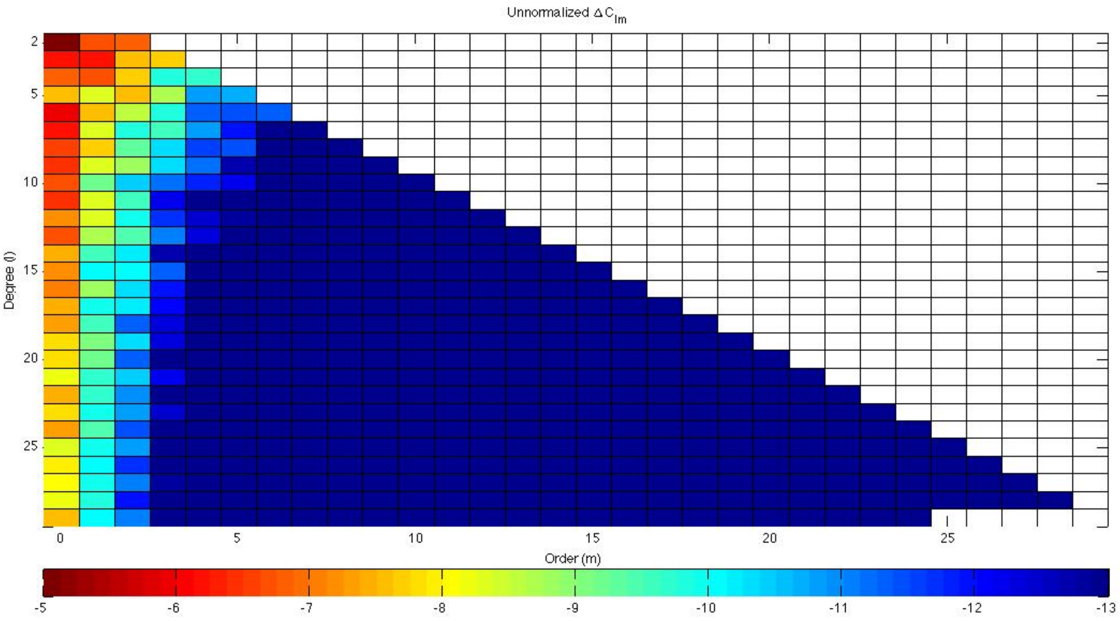

Figure 4.2. Unnormalized ΔClm for the maximum penetration depth (Kaspi Y., private communication,2011).

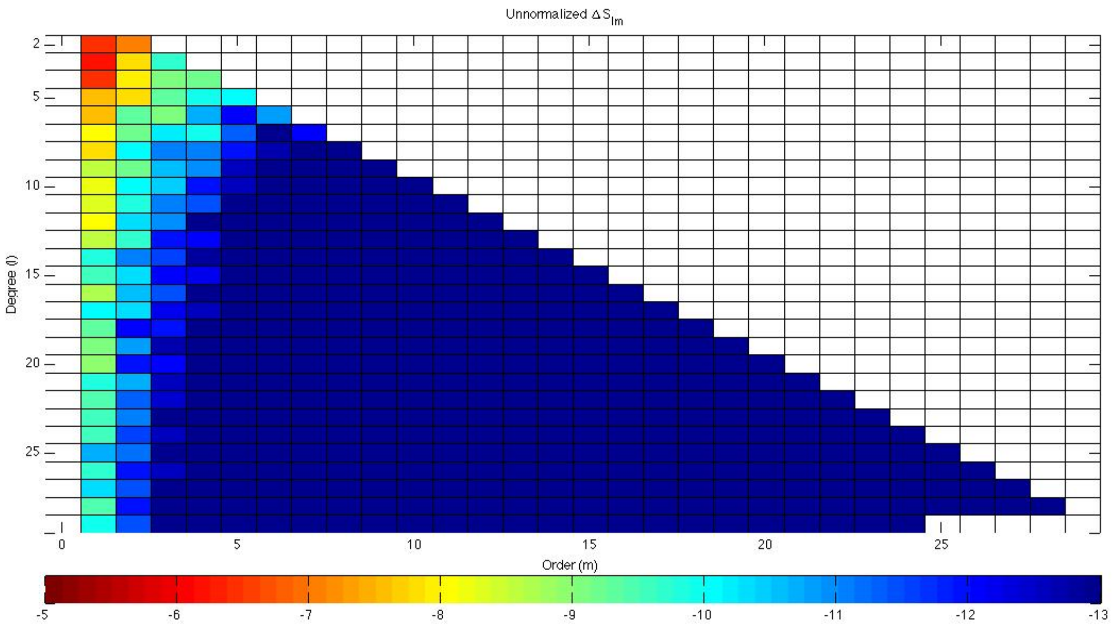

Figure 4.3. Unnormalized ΔSlm for the maximum penetration depth (Kaspi Y., private communication,2011).

The simulated gravity coefficients are reported in Table 4.3:

Coefficient	Zonal winds ΔJ	Total value
$\mathbf{J_{2}}$	$1.252237940150419 \cdot 10^{-6}$	$1.469768223794015 \cdot 10^{-2}$
$\mathbf{J_{3}}$	$-5.799646196902762 \cdot 10^{-8}$	$-5.799646196902762 \cdot 10^{-8}$
$\mathbf{J_{4}}$	$1.582914824151301 \cdot 10^{-8}$	$-5.871241708517585 \cdot 10^{-4}$
$\mathbf{J_{5}}$	$2.507218245087703 \cdot 10^{-9}$	$2.507218245087703 \cdot 10^{-9}$
$\mathbf{J_{6}}$	$1.142661182476699 \cdot 10^{-7}$	$3.093426611824767 \cdot 10^{-5}$
$\mathbf{J_{7}}$	$6.889535749280466 \cdot 10^{-8}$	$6.889535749280466 \cdot 10^{-8}$
$\mathbf{J_{8}}$	$-2.930791600868505 \cdot 10^{-8}$	$-1.891307916008685 \cdot 10^{-6}$
$\mathbf{J_{9}}$	$-3.959003838096452 \cdot 10^{-8}$	$-3.959003838096452 \cdot 10^{-8}$
$\mathbf{J_{10}}$	$-2.046454392842821 \cdot 10^{-8}$	$1.022354560715718 \cdot 10^{-7}$
$\mathbf{J_{11}}$	$4.097572138760080 \cdot 10^{-8}$	$4.097572138760080 \cdot 10^{-8}$
$\mathbf{J_{12}}$	$-6.813089218623050 \cdot 10^{-8}$	$-1.538608921862305 \cdot 10^{-8}$
$\mathbf{J_{13}}$	$-2.194601291076683 \cdot 10^{-8}$	$-2.194601291076683 \cdot 10^{-8}$
$\mathbf{J_{14}}$	$-3.331522786988295 \cdot 10^{-9}$	$-2.706222786988295 \cdot 10^{-9}$
$\mathbf{J_{15}}$	$6.766118930368163 \cdot 10^{-9}$	$6.766118930368163 \cdot 10^{-9}$
$\mathbf{J_{16}}$	$9.406368185924863 \cdot 10^{-9}$	$9.359258185924863 \cdot 10^{-9}$
$\mathbf{J_{17}}$	$-3.868747716403672 \cdot 10^{-9}$	$-3.868747716403672 \cdot 10^{-9}$
$\mathbf{J_{18}}$	$4.679111543428224 \cdot 10^{-9}$	$4.682752543428224 \cdot 10^{-9}$

J_{19}	$1.591009318726042 \cdot 10^{-9}$	$1.591009318726042 \cdot 10^{-9}$
J_{20}	$-1.627169077921347 \cdot 10^{-9}$	$-1.627456377921347 \cdot 10^{-9}$
J_{21}	$7.333917468071332 \cdot 10^{-10}$	$7.333917468071332 \cdot 10^{-10}$
J_{22}	$3.982849659430137 \cdot 10^{-9}$	$3.982872699430137 \cdot 10^{-9}$
J_{23}	$1.372107355060810 \cdot 10^{-9}$	$1.372107355060810 \cdot 10^{-9}$
J_{24}	$-4.890096797989601 \cdot 10^{-9}$	$-4.890098670989601 \cdot 10^{-9}$
J_{25}	$-4.496337983161392 \cdot 10^{-10}$	$-4.496337983161392 \cdot 10^{-10}$
J_{26}	$-1.178175530319418 \cdot 10^{-9}$	$-1.178175376919418 \cdot 10^{-9}$
J_{27}	$8.271938184315541 \cdot 10^{-10}$	$8.271938184315541 \cdot 10^{-10}$
J_{28}	$-5.996900416620652 \cdot 10^{-10}$	$-5.996900532020652 \cdot 10^{-10}$
J_{29}	$-3.155342388029311 \cdot 10^{-9}$	$-3.155342388029311 \cdot 10^{-9}$
J_{30}	$4.751608532116014 \cdot 10^{-10}$	$4.751608538474014 \cdot 10^{-10}$

Table 4.3 Simulated zonal gravity coefficients (unnormalized).

4.1.4 The spacecraft model

The presence of large surfaces exposes the Juno spacecraft to the relevant perturbations coming from surface forces of non-gravitational origin. The spacecraft does not host an accelerometer that could calibrate this kind of perturbations therefore an accurate modeling of this dynamical noise must be achieved.

In the Juno case five main surfaces have been identified: the three solar arrays, the spacecraft bus and the high gain antenna. All these surfaces are considered independent one from the other since the focus is on the resultant acceleration of the spacecraft center of mass and not the attitude dynamics of the body. The characteristics of these components are briefly reported.

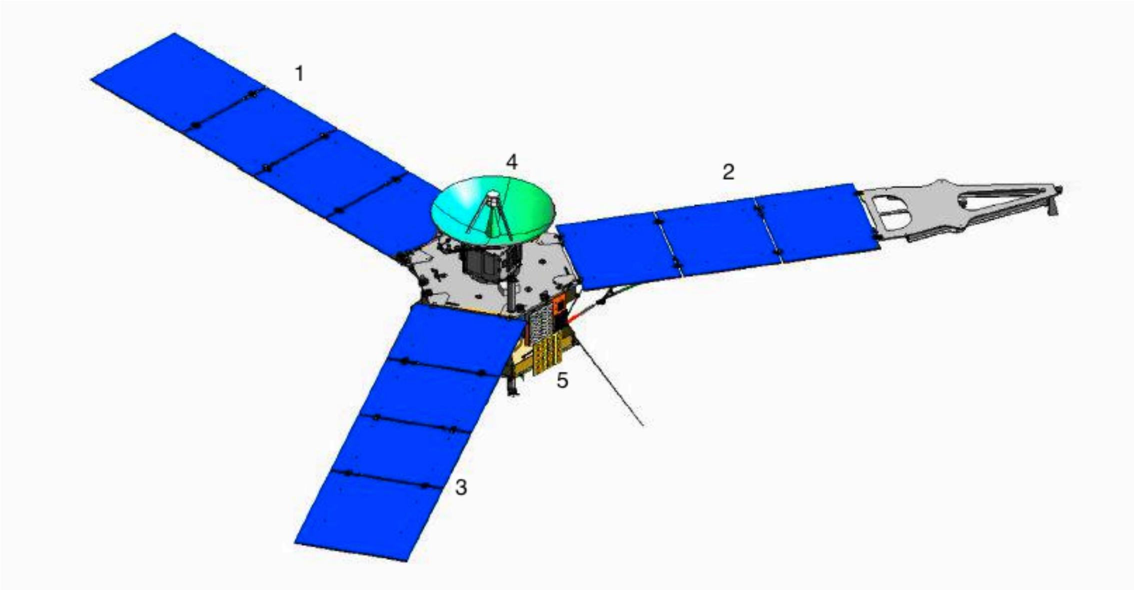

Figure 4.4. Juno spacecraft main surfaces.

n	Component	Model	Direction	Size
1	Solar array	Flat plate	Normal pointing Earth	Area = 18 m^2
2	Solar array	Flat plate	Normal pointing Earth	Area = 18 m^2
3	Solar array	Flat plate	Normal pointing Earth	Area = 18 m^2
4	HGA	Antenna	Axis pointing Earth	Radius = 1.25 m Depth = 0.47
5	Bus	Cylinder	Axis pointing Earth	

Table 4.4. Spacecraft components dimensions.

The optical properties of the surfaces must also be specified. A certain ratio r of the incoming radiation is reflected. The reflected radiation is in part reflected specularly (s), while the remaining portion is diffuse reflection. The specular reflectivity coefficient is $rs/2$ while the diffuse coefficient is $\left(r(1-s)+k(1-r)\right)/3$, where k is a coefficient modeling backside reradiation. The same optical properties are applied for solar radiation pressure, albedo and planetary IR emission.

n	Component	Specular coefficient	Diffuse coefficient
1	Solar array	0.016	0.1226
2	Solar array	0.016	0.1226
3	Solar array	0.016	0.1226
4	HGA	0.036	0.1760
5	Bus	0.036	0.1760

Table 4.5. Spacecraft components optical properties.

The spacecraft mass changes during the mission because of the fuel consumption for the maneuvers necessary to orbit maintenance. For the simulation purposes, it is sufficient to keep the mass of the spacecraft fixed at a level of 1282.8 kg.

4.1.5 Non-gravitational accelerations

The non-gravitational accelerations constitute a possible source of dynamical noise that must be carefully calibrated in order to ensure the success of the experiment.

The perturbations present in the simulation are the solar radiation pressure, the planetary albedo and the Jupiter infrared thermal emission. Among these, only the solar radiation pressure can produce a significant effect on the spacecraft trajectory. The spacecraft attitude during the gravity science orbits places most of the surface (solar arrays) facing the Earth (which from Jupiter is angularly close to the Sun) and nearly orthogonal to the nadir direction.

4.1.5.1 Solar radiation pressure

The acceleration exerted on the spacecraft by the light coming from the sun can be expressed as (ODP User's Manual v.1, p. 113)

$$\ddot{\vec{r}} = \left(\frac{C_1 P}{m r_{sp}^2} \right) \vec{F}$$

where

C_1 is the solar flux constant at 1 AU $\left(C_1 = \frac{\Phi_{1AU} r_{1AU}^2}{c} = 1.020506244 \cdot 10^8 \frac{kg\, km^3}{m^2\, s^2} \right)$.

r_{sp} is the Sun-spacecraft distance (km).

m is the mass of the spacecraft (kg).

P is the Sun shadow factor

= 0 if the spacecraft is in the umbra.

< 1 if the spacecraft is in the penumbra.

= 1 if the spacecraft is in clear sunlight.

$\vec{F}$ is the vector of geometry/reflectivities.

4.1.5.2 *Planetary Albedo*

The elemental acceleration caused by the sunlight reflected by a point P on the surface of Jupiter is expressed by (ODP User's Manual v.1, p. 128)

$$d\ddot{r}_{ALB} = \frac{-C_1 K \cos\psi_s}{m r_{cs}^2} A \left(\sum_i F_{Ti} \hat{N}_i + F_{Ri} \hat{r}_{ps} \right) \frac{\cos\psi}{\pi r_{ps}^2} dS$$

where

C_1 is the solar flux constant at 1 AU.

r_{cs} is the planet-Sun distance (km).

m is the mass of the spacecraft (kg).

K is the Sun shadow function

= 0 if the spacecraft is in the shadow.

= 1 if the spacecraft is in clear sunlight.

r_{ps} is the point P to spacecraft distance (km).

$\hat{r}_{ps}$ point P to spacecraft direction.

ψ_s is the Sun-planet center-point P angle.

ψ is the angle between the planet center-point P and point P-spacecraft direction vectors.

$\hat{N}_i$ is the spacecraft component i orientation vector (surface normal or axes).

F_{Ti} , F_{Ri} are quantities depending upon the shapes of the spacecraft components.

A is the albedo coefficient. Generally it is expanded in terms of spherical harmonics in order to describe the different reflectivity of the particular planet surface regions.

$$A = \sum_{l=0}^{10} \sum_{m=0}^{l} \left(C_{lm}^{A} \cos m\lambda + S_{lm}^{A} \sin m\lambda \right) P_{lm} \left(\sin \phi \right)$$

where

ϕ, λ are the latitude and longitude of the point P.

P_{lm} is the associated Legendre function.

In the case of the Jupiter it has been chosen that the albedo coefficient has the same value for each point on Jupiter surface.

$$\left.\begin{array}{ll} l,m = 0 & C_{00}^{A} = 0.52 \\ l,m \neq 0 & C_{lm}^{A} = 0 \end{array}\right\} \quad A = 0.52$$

. (Allen *et al.*, 2000, table 12.8)

4.1.5.3 Jupiter thermal infrared emission

The planet emits power in the form of thermal radiation at infrared frequency.

The elemental acceleration is expressed similarly to what already shown for the albedo (ODP User's Manual v.1, p. 128).

$$d\ddot{r}_{IR} = \frac{-C_1}{4mr_{cs}^2} E \left(\sum_i F_{Ti} \hat{N}_i + F_{Ri} \hat{r}_{ps} \right) \frac{\cos\psi}{\pi r_{ps}^2} dS$$

The symbols have the same meaning as in Section 4.1.5.2.

E is the planet emission coefficient. It is expressed in terms of spherical harmonics to represent the variability of the power emitted over the planet surface.

$$E = \sum_{l=0}^{10} \sum_{m=0}^{l} \left(C_{lm}^E \cos m\lambda + S_{lm}^E \sin m\lambda \right) P_{lm} \left(\sin\phi \right)$$

The power emission is not uniform over the spherical surface. The emissivity is larger at the equator and smaller at the poles (Gierasch, 1999).

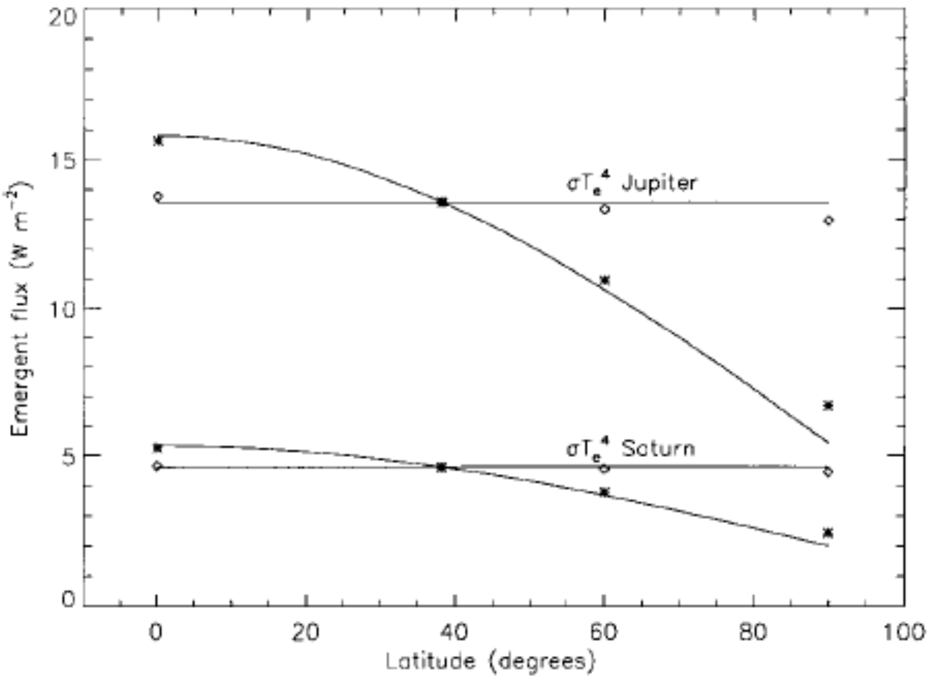

Figure 4.5. Emergent thermal flux for Jupiter and Saturn (Gierasch, 1999).

Moreover, the infrared mapping of Jupiter from the NASA Infra-Red Telescope Facility shows that the power emission is zonally differentiated. This behavior can be represented by a zonal expansion of the emission coefficient.

The realization in Table 4.6 is not representative of the real Jupiter emission. The coefficients are computed by approximating the latitudinal variability of the flux with superimposed higher degree variations. This kind of modeling is useful to study possible interference of the perturbation with the gravity signal (mainly zonal).

l	**M**	$C^{E}_{l,m}$
0	0	1.02
1	0	$5.63 \cdot 10^{-2}$
2	0	$-4.74 \cdot 10^{-1}$
3	0	$-1.06 \cdot 10^{-1}$
4	0	$6.90 \cdot 10^{-3}$
5	0	$7.82 \cdot 10^{-2}$
6	0	$-1.10 \cdot 10^{-1}$
7	0	$-5.99 \cdot 10^{-2}$
8	0	$1.28 \cdot 10^{-2}$
9	0	$8.78 \cdot 10^{-3}$
10	0	$-1.14 \cdot 10^{-2}$

Table 4.6. Emission coefficient zonal harmonic expansion.

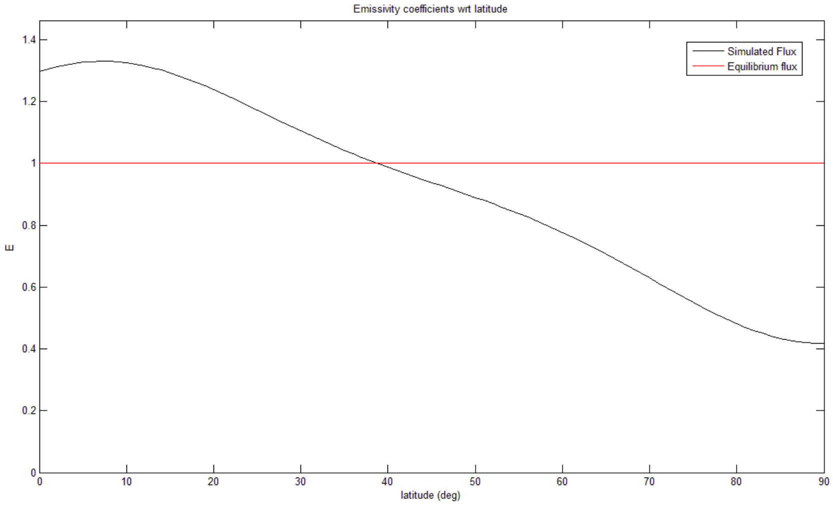

Figure 4.6. Emission coefficient wrt latitude (coefficients in Table 4.6)

4.1.6 Data simulation

The models presented in Section 4.1 are used to integrate the Juno trajectory when flying close to perijoves.

The integrated trajectory, along with the Earth station inertial position, is the input for the precise solution of the light-time problem and the observables computation.

The Juno gravity experiment will be carried out using range-rate (Doppler) observables only, collected in a period of six hours about the pericenter.

The Ka-band signal will be sent from ground and coherently transmitted back by the onboard Ka-band transponder.

The Doppler observables will be corrupted by noise coming from several sources. An error assessment has been given in Section 3.3. The frequency spectrum of the noise is not completely white but shows components with spectral index -2/5 and -2/3 dominant at low frequencies.

The instrument requirements state that the expected error in the Doppler observable should not exceed $5 \cdot 10^{-3}$ mm/s two-way at 1000 s integration time. This error corresponds to a two-way Allan deviation of $\sigma_y(1000\,s) = 1.67 \cdot 10^{-14}$.

The ODP does not allow the generation of observables in Ka-band. An equivalent X-band is adopted. The Allan deviation is calculated for a signal in Ka-band, but the frequency is X-band (7.2 GHz). The effective frequency deviation can be computed using the following equations:

$$\sigma_y(60\,s) = \sqrt{\frac{1000}{60}}\sigma_y(1000\,s) = 6.8 \cdot 10^{-14}$$
$$\delta f = \sigma_y(60\,s) \cdot f_{ref(X)} = 0.49\,mHz$$

The first relationship comes from the scaling in time of white frequency noise while the second is an approximation of the definition of Allan deviation.

An additive white gaussian noise with standard deviation δf is applied to the generated data.

4.2 Gravity field estimation

The data simulation process substitutes what in 2016-2017 will be the tracking data acquisition from DSS-25. The final output is a tracking data file entirely similar to what would be return in the real mission.

The first step of the estimation process is to build a model of universe able to represent the accelerations affecting the spacecraft trajectory and consequently the observables. This model has to rely on present day accepted measurements and geophysical assumptions.

The second step is to define the weight to apply to the observables. In real data processing, this step is an iterative process requiring a continuous update of the weighting matrix until convergence to a level close to the noise RMS. In simulated data analysis it is possible to use the correct weighting matrix from the beginning, since the standard deviation of the noise is already known.

The third step is the choice of the set of model parameters to estimate.

4.2.1 Model of the jovian system

In a real case, each model of acceleration will be only an approximation of the actual one. Therefore we have to deal with multiple sources of mismodeling, even if most of the models are sufficiently accurate to calibrate the real accelerations at the observable precision.

On the other hand, the most inaccurate of them must be corrected in the estimation process even if their determination is not the main objective of the experiment.

As a starting point, it has been chosen that the model of universe for the estimation process is exactly equal to the model used to generate the observables, except for the accelerations object of the experiment.

Therefore all non-gravitational accelerations result perfectly calibrated once the estimated trajectory sufficiently approximates the actual one. It is equivalent to state that the models, which are not of interest, are adequate enough to calibrate the real accelerations at the data accuracy.

The investigation focuses on the Jupiter gravity field and tidal deformation.

4.2.1.1 Trajectory initial conditions

The initial conditions of the trajectory are the same used while simulating the observables.

Therefore no initial error is assumed for the spacecraft position and velocity.

However, the acceleration acting on the spacecraft in the two cases is different. Hence, the propagated trajectories are not coincident.

4.2.1.2 Gravitational accelerations

The gravity field of Jupiter is the main object of the study. It is initially set to the following values.

Body	Parameter	Value
5	GM	$1.267127648382719 \cdot 10^{8}\ km^3/s^2$
599	J_2	$6.572442857220718 \cdot 10^{-3}$
599	J_3	$-2.432734712710358 \cdot 10^{-7}$
599	J_4	$-1.957134305251665 \cdot 10^{-4}$
599	J_6	$9.499311632060060 \cdot 10^{-6}$
599	k_2	0.5
599	k_3	0.5
501	GM	$5.959916033410404 \cdot 10^{3}\ km^3/s^2$
502	GM	$3.202738774922892 \cdot 10^{3}\ km^3/s^2$

503	GM	$9.887834453334144 \cdot 10^3 \; km^3/s^2$
504	GM	$7.179289361397270 \cdot 10^3 \; km^3/s^2$

Table 4.7. Gravity field initial conditions (Jacobson, 2003). The Body ID 5 refers to Jupiter system, 599 to Jupiter as a planet. Body ID 501 to 504 identify the 4 galilean satellites Io, Europa, Ganymede and Callisto.

All not listed gravity coefficients are initially set to zero.

4.2.1.3 *Spacecraft model and non-gravitational accelerations*

The spacecraft and non-gravitational accelerations models are identical to what used to simulate the tracking data. Obviously the acceleration is dependent on the spacecraft state vector at each integration node. In principle if the integrated trajectory coincides with the actual one no acceleration difference would come from this models.

A mismodeling of the spacecraft properties or of the non-gravitational accelerations may be inserted to test the sensitivity of the solution to these perturbations. The characteristics of models used for the spacecraft, solar radiation pressure, albedo and thermal IR emission can be found in Sections 4.1.5.

4.2.2 Data weighting

The weight applied to the observables is defined as (Tapley *et al.*, 2004) $WEIGHT = 1/\sigma^2$.

For the Doppler observable $\sigma = RMS \cdot \left(1 + \frac{18}{(E+1)^2}\right)$

where

RMS is the noise RMS

E is the data point elevation.

The elevation dependent factor is introduced to de-weight those data collected when the spacecraft is at an elevation below 20 degrees. In this cases the radio signal has to travel along a wide portion of the atmosphere resulting less accurate than data received when the spacecraft is at the zenith (90 degrees elevation).

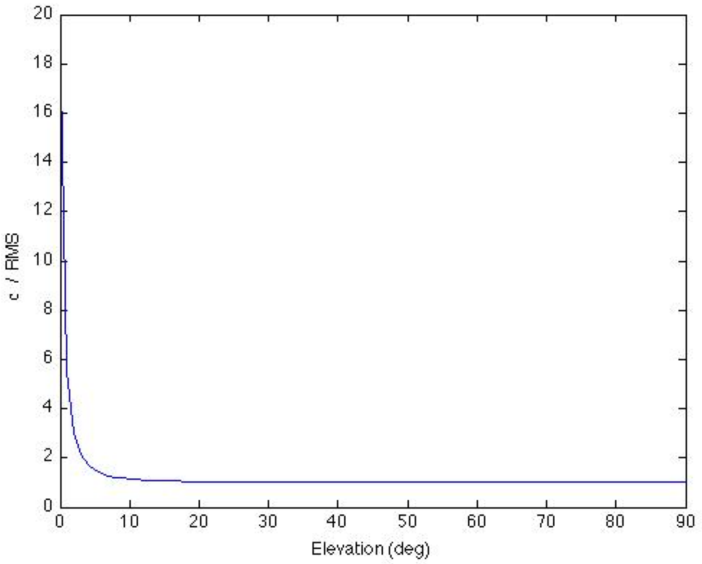

Figure 4.7. Elevation dependent correction factor wrt elevation.

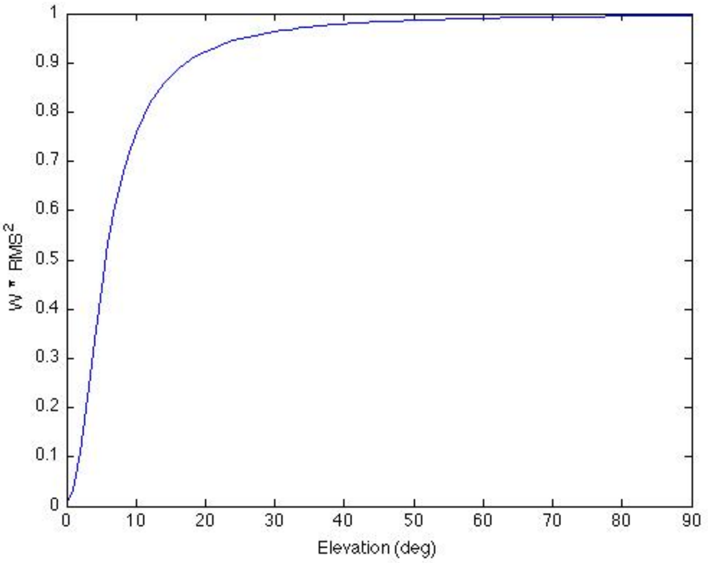

Figure 4.8. Effect of the elevation dependent correction on the weight.

The noise RMS is chosen equal to the simulated noise RMS. The software automatically computes the correct weight for each data point on the basis of the elevation.

4.2.3 Estimated parameters set

The parameters that are included in the estimation are listed in Table 4.8, Table 4.9Table 4.10Table 4.11 with the associated a priori uncertainty.

Since the multi-arc approach will be used, it is necessary to specify which are the local and the global parameters.

The local parameters are the state vector components at the start epoch of each arc. X_i and DX_i are the initial position and velocity vectors for arc i (6 components per arc). The reference frame is Jupiter System Barycenter, Earth Mean Equator at epoch J2000.

State vector component	A priori uncertainty
X_i (i =1, …, 25)	10 km
DX_i (i = 1, …, 25)	10^{-5} km/s

Table 4.8 Local parameters and their a priori uncertainty.

The Jupiter GM, the gravity field spherical harmonics coefficients and the Love numbers of degree 2 and 3 compose the global parameters set. The gravity field coefficients are normalized allowing a faster computation of the partial derivatives. Low degrees tesseral coefficients (up to degree 5) are accounted in to consider the uncertainty that could come from the their possible presence.

Parameter	A priori uncertainty
GM	2 km^3/s^2
J2	$9.391 \cdot 10^{-7}$
C2,1	$1.681 \cdot 10^{-6}$
S2,1	$3.056 \cdot 10^{-6}$
C2,2	$2.609 \cdot 10^{-6}$
S2,2	$1.174 \cdot 10^{-6}$
J3	$3.402 \cdot 10^{-6}$

Parameter	A priori uncertainty
C5,4	$1.780 \cdot 10^{-8}$
S5,4	$1.418 \cdot 10^{-7}$
C5,5	$7.734 \cdot 10^{-8}$
S5,5	$3.692 \cdot 10^{-7}$
J6	$1.448 \cdot 10^{-5}$
J7	$1.779 \cdot 10^{-6}$
J8	$7.108 \cdot 10^{-7}$

C3,1	$6.620\cdot10^{-6}$
S3,1	$5.582\cdot10^{-6}$
C3,2	$8.490\cdot10^{-7}$
S3,2	$4.299\cdot10^{-7}$
C3,3	$1.657\cdot10^{-6}$
S3,3	$1.348\cdot10^{-8}$
J4	$5.600\cdot10^{-6}$
C4,1	$2.097\cdot10^{-6}$
S4,1	$3.977\cdot10^{-6}$
C4,2	$9.914\cdot10^{-7}$
S4,2	$5.581\cdot10^{-7}$
C4,3	$2.276\cdot10^{-8}$
S4,3	$1.410\cdot10^{-7}$
C4,4	$1.071\cdot10^{-7}$
S4,4	$3.254\cdot10^{-7}$
J5	$7.560\cdot10^{-8}$
C5,1	$5.012\cdot10^{-8}$
S5,1	$3.256\cdot10^{-7}$
C5,2	$1.710\cdot10^{-6}$
S5,2	$8.891\cdot10^{-7}$
C5,3	$5.999\cdot10^{-7}$
S5,3	$1.512\cdot10^{-7}$

J9	$9.083\cdot10^{-7}$
J10	$4.466\cdot10^{-7}$
J11	$8.544\cdot10^{-7}$
J12	$1.363\cdot10^{-7}$
J13	$4.224\cdot10^{-7}$
J14	$6.186\cdot10^{-8}$
J15	$1.215\cdot10^{-7}$
J16	$1.637\cdot10^{-7}$
J17	$6.539\cdot10^{-8}$
J18	$7.692\cdot10^{-8}$
J19	$2.548\cdot10^{-8}$
J20	$2.541\cdot10^{-8}$
J21	$1.118\cdot10^{-8}$
J22	$5.937\cdot10^{-8}$
J23	$2.001\cdot10^{-8}$
J24	$6.986\cdot10^{-8}$
J25	$6.296\cdot10^{-9}$
J26	$1.618\cdot10^{-8}$
J27	$1.115\cdot10^{-8}$
J28	$7.943\cdot10^{-9}$
J29	$4.108\cdot10^{-8}$
J30	$6.084\cdot10^{-9}$

Table 4.9 Gravity field global coefficients with associated a priori uncertainty (normalized).

In the ODP the Love numbers are defined by degree and order, to allow the determination of a different tidal deformation relatively to the corresponding gravity field coefficient.

In formulas, the tidal correction to the gravity field coefficient is given by (Gavrilov *et al.*, 1976):

$$\Delta J_n = -\left(\frac{m_s}{M_J}\right)\left(\frac{s_1}{a_1}\right)^n\left(\frac{s_1}{R}\right)^{n+1} k_{n,0}P_n\left(\cos\vartheta'\right)$$

$$\left.\begin{matrix}\Delta C_{l,m}\\ \Delta S_{l,m}\end{matrix}\right\} = 2\frac{(n-m)!}{(n+m)!}\left(\frac{m_s}{M_J}\right)\left(\frac{s_1}{a_1}\right)^n\left(\frac{s_1}{R}\right)^{n+1} k_{n,m}P_{n,m}\left(\cos\vartheta'\right)\left\{\begin{matrix}\cos m\lambda'\\ \sin m\lambda'\end{matrix}\right\}$$

where

m_s, M_J	perturbing body and Jupiter mass.
s_1	Jupiter mean radius.
a_1	Jupiter equatorial radius.
R, ϑ', λ'	perturbing body spherical coordinates in a Jupiter centered Jupiter fixed frame.

The degree n Love number is therefore expressed by n+1 parameters. In the current analysis each group of n+1 parameters is a priori correlated with correlation index equal to 1 (or a value close to 1 to avoid singularities) in order to have a unique parameter describing the tidal gravity field distortion of degree n. Henceforth the author will refer to the single parameter k_2 or k_3 without further specifying the order subdivision.

Love number	A priori uncertainty
k_2	0.5
k_3	0.5

Table 4.10 Global Love numbers and associated a priori uncertainty.

The GMs of the galilean satellites are inserted in the estimation process as consider parameters. They are not estimated but their a priori uncertainty is considered.

Parameter	A priori uncertainty (10^{-2} km^3/s^2)
Io GM	1.2
Europa GM	0.9
Ganymede GM	1.7
Callisto GM	1.3

Table 4.11 Consider parameters: the galilean satellites GM a priori uncertainty.

Concluding, the estimation will count 150 local parameters, 65 global parameters and 4 global consider parameters, for a total of 215 estimated parameters and 4 consider.

4.2.4 Estimation results

The results of the gravity field estimation will be shown in terms of gravity spectrum and surface gravity.

The Table 4.12 and the plot in Figure 4.9 shows the results for the zonal gravity spectrum.

Parameter	Formal uncertainty	Estimation Error	Estimated value
J2	$2.02 \cdot 10^{-10}$	$3.78 \cdot 10^{-11}$	$6.57300335696616 \cdot 10^{-3}$
J3	$1.62 \cdot 10^{-10}$	$2.19 \cdot 10^{-11}$	$-2.19424688710042 \cdot 10^{-8}$
J4	$1.08 \cdot 10^{-10}$	$4.29 \cdot 10^{-11}$	$-1.95708014002502 \cdot 10^{-4}$
J5	$1.76 \cdot 10^{-10}$	$1.67 \cdot 10^{-10}$	$9.23303568556361 \cdot 10^{-10}$
J6	$3.02 \cdot 10^{-10}$	$1.79 \cdot 10^{-10}$	$8.57944323547712 \cdot 10^{-6}$
J7	$5.52 \cdot 10^{-10}$	$6.84 \cdot 10^{-10}$	$1.84726400413802 \cdot 10^{-8}$
J8	$9.93 \cdot 10^{-10}$	$6.27 \cdot 10^{-10}$	$-4.59336528185576 \cdot 10^{-7}$
J9	$1.73 \cdot 10^{-9}$	$8.91 \cdot 10^{-10}$	$-8.19170843615847 \cdot 10^{-9}$
J10	$2.88 \cdot 10^{-9}$	$5.08 \cdot 10^{-10}$	$2.18017153608362 \cdot 10^{-8}$
J11	$4.56 \cdot 10^{-9}$	$3.90 \cdot 10^{-10}$	$8.93359265100151 \cdot 10^{-9}$
J12	$6.79 \cdot 10^{-9}$	$9.43 \cdot 10^{-10}$	$-2.13373345818863 \cdot 10^{-9}$
J13	$9.52 \cdot 10^{-9}$	$1.19 \cdot 10^{-9}$	$-5.41700081855902 \cdot 10^{-9}$
J14	$1.25 \cdot 10^{-8}$	$3.36 \cdot 10^{-9}$	$2.85375441953438 \cdot 10^{-9}$
J15	$1.52 \cdot 10^{-8}$	$2.90 \cdot 10^{-9}$	$-1.68123498362022 \cdot 10^{-9}$
J16	$1.70 \cdot 10^{-8}$	$3.95 \cdot 10^{-9}$	$5.58257820545857 \cdot 10^{-9}$
J17	$1.75 \cdot 10^{-8}$	$1.72 \cdot 10^{-9}$	$-2.37886724407397 \cdot 10^{-9}$
J18	$1.61 \cdot 10^{-8}$	$1.66 \cdot 10^{-9}$	$2.42609796583061 \cdot 10^{-9}$
J19	$1.34 \cdot 10^{-8}$	$2.73 \cdot 10^{-10}$	$5.27967584275388 \cdot 10^{-10}$
J20	$1.05 \cdot 10^{-8}$	$3.78 \cdot 10^{-10}$	$1.24143085549203 \cdot 10^{-10}$
J21	$8.97 \cdot 10^{-9}$	$1.99 \cdot 10^{-10}$	$3.11094514672530 \cdot 10^{-10}$
J22	$9.37 \cdot 10^{-9}$	$1.49 \cdot 10^{-9}$	$2.08535182277297 \cdot 10^{-9}$
J23	$8.69 \cdot 10^{-9}$	$6.89 \cdot 10^{-10}$	$-4.89203281850926 \cdot 10^{-10}$

J24	$7.65 \cdot 10^{-9}$	$1.80 \cdot 10^{-9}$	$1.09795377693858 \cdot 10^{-9}$
J25	$5.56 \cdot 10^{-9}$	$3.48 \cdot 10^{-10}$	$2.85117078965368 \cdot 10^{-10}$
J26	$5.58 \cdot 10^{-9}$	$1.07 \cdot 10^{-9}$	$9.08903605044376 \cdot 10^{-10}$
J27	$5.56 \cdot 10^{-9}$	$4.12 \cdot 10^{-10}$	$5.23579192389037 \cdot 10^{-10}$
J28	$5.30 \cdot 10^{-9}$	$7.83 \cdot 10^{-10}$	$7.03555980452321 \cdot 10^{-10}$
J29	$3.17 \cdot 10^{-9}$	$8.47 \cdot 10^{-11}$	$-3.26075340031098 \cdot 10^{-10}$
J30	$2.04 \cdot 10^{-9}$	$5.43 \cdot 10^{-10}$	$6.03525431155385 \cdot 10^{-10}$

Table 4.12 Zonal gravity estimation results.

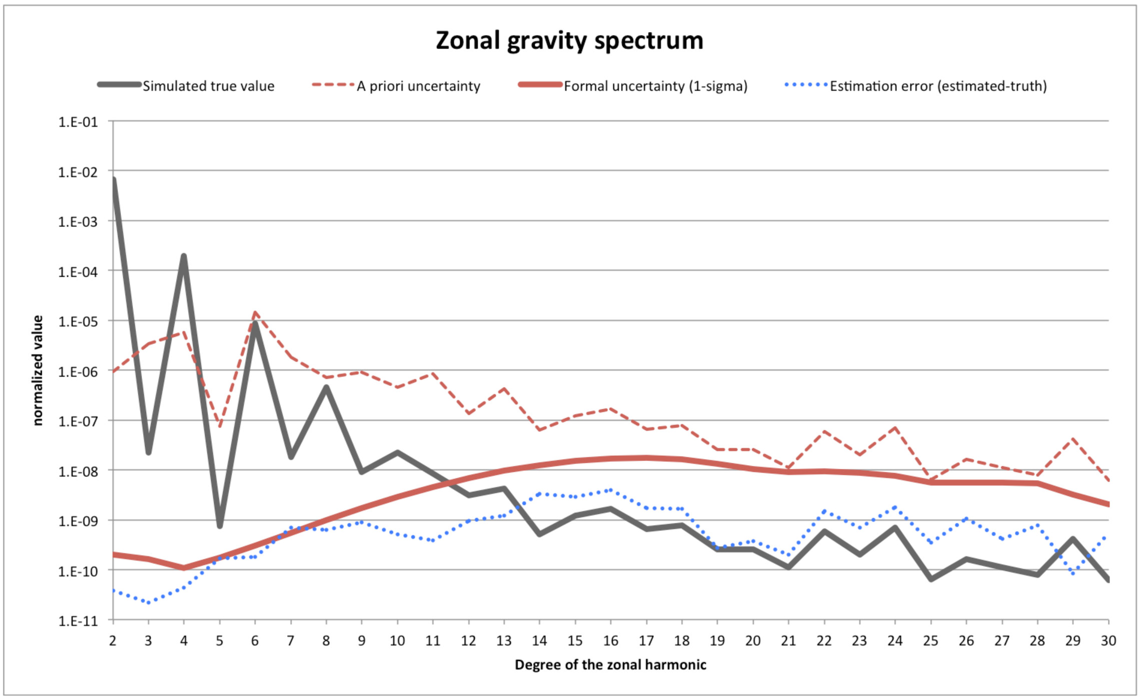

Figure 4.9 Zonal gravity spectrum. The black continuous line represents the simulated "true" gravity field. The dashed red line is the a priori uncertainty corresponding to the gravity perturbation produced if the whole planet's mass participate to the zonal winds motion (multiplied by 10). The red continuous line and the dotted blue line are relatively the formal uncertainty associated with the estimation and the true estimation error (estimated value – true value).

The 1-sigma formal uncertainty is at a level of 10^{-10} for the low degree zonal harmonics. This level of uncertainty is sufficient to pose a strong constraint on the mass of the core of Jupiter. Right after J_4 the uncertainty starts to increase rapidly until a priori saturation around J_{16}. All the harmonics beyond J_{10} are below the formal uncertainty curve and therefore cannot be correctly determined.

This kind of behavior is well known to gravity data analyst, and shows up whenever the spacecraft cannot uniformly sample the gravity field in the whole range of latitudes (cf. Milani *et al.*, 2010, pp. 339-344). The issue has a mathematical origin. The spherical harmonics basis of functions is defined to be orthonormal on a spherical surface. This property is not valid on a limited subspace of the sphere. Spherical harmonics are therefore not orthonormal in the latitude belt covered by the Juno gravity data (cf. section 0). This problem reflects in correlation factors among the parameters close to 1.

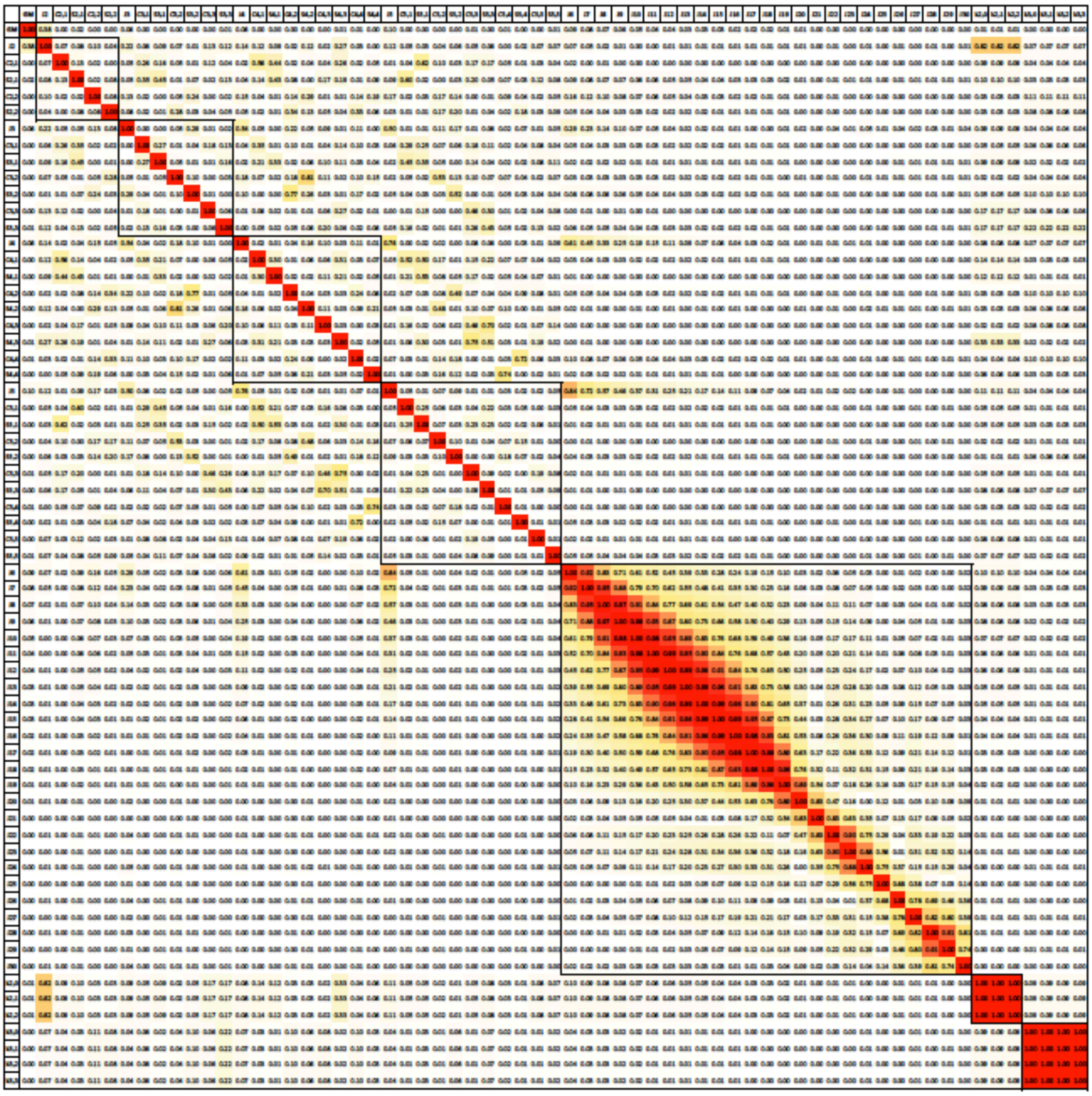

Figure 4.10 Global parameters correlation matrix. The color scale ranges from white for the minimum values to red for values close to 1.

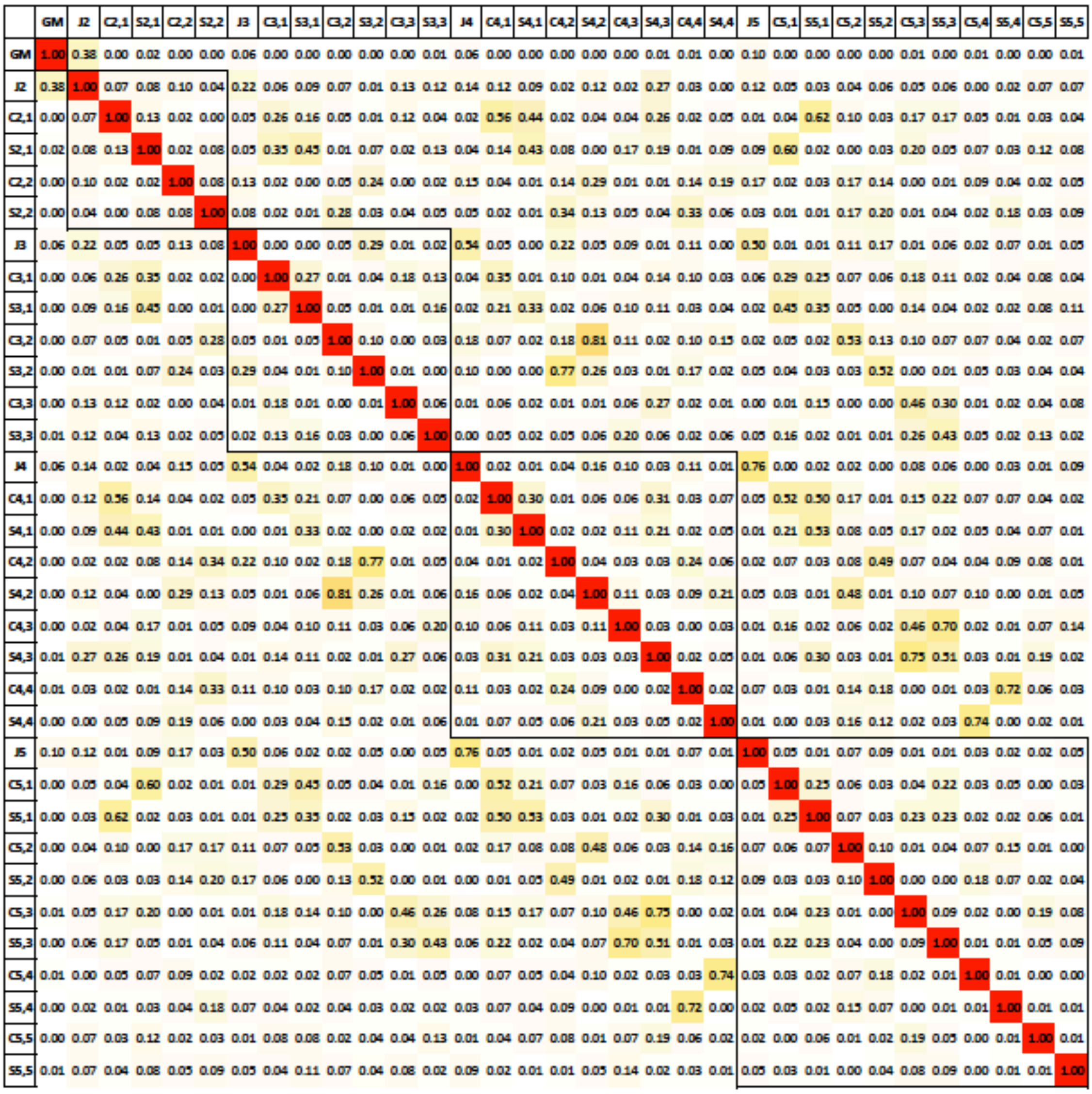

	GM	J2	C2,1	S2,1	C2,2	S2,2	J3	C3,1	S3,1	C3,2	S3,2	C3,3	S3,3	J4	C4,1	S4,1	C4,2	S4,2	C4,3	S4,3	C4,4	S4,4	J5	C5,1	S5,1	C5,2	S5,2	C5,3	S5,3	C5,4	S5,4	C5,5	S5,5
GM	1.00	0.38	0.00	0.02	0.00	0.00	0.06	0.00	0.00	0.00	0.00	0.00	0.01	0.06	0.00	0.00	0.00	0.00	0.00	0.01	0.01	0.00	0.10	0.00	0.00	0.00	0.00	0.01	0.00	0.01	0.00	0.00	0.01
J2	0.38	1.00	0.07	0.08	0.10	0.04	0.22	0.06	0.09	0.07	0.01	0.13	0.12	0.14	0.12	0.09	0.02	0.12	0.02	0.27	0.03	0.00	0.12	0.05	0.03	0.04	0.06	0.05	0.06	0.00	0.02	0.07	0.07
C2,1	0.00	0.07	1.00	0.13	0.02	0.00	0.05	0.26	0.16	0.05	0.01	0.12	0.04	0.02	0.56	0.44	0.02	0.04	0.04	0.26	0.02	0.05	0.01	0.04	0.62	0.10	0.03	0.17	0.17	0.05	0.01	0.03	0.04
S2,1	0.02	0.08	0.13	1.00	0.02	0.08	0.05	0.35	0.45	0.01	0.07	0.02	0.13	0.04	0.14	0.43	0.08	0.00	0.17	0.19	0.01	0.09	0.09	0.60	0.02	0.00	0.03	0.20	0.05	0.07	0.03	0.12	0.08
C2,2	0.00	0.10	0.02	0.02	1.00	0.08	0.13	0.02	0.00	0.05	0.24	0.00	0.02	0.15	0.04	0.01	0.14	0.29	0.01	0.01	0.14	0.19	0.17	0.02	0.03	0.17	0.14	0.00	0.01	0.09	0.04	0.02	0.05
S2,2	0.00	0.04	0.00	0.08	0.08	1.00	0.08	0.02	0.01	0.28	0.03	0.04	0.05	0.05	0.02	0.01	0.34	0.13	0.05	0.04	0.33	0.06	0.03	0.01	0.01	0.17	0.20	0.01	0.04	0.02	0.18	0.03	0.09
J3	0.06	0.22	0.05	0.05	0.13	0.08	1.00	0.00	0.00	0.05	0.29	0.01	0.02	0.54	0.05	0.00	0.22	0.05	0.09	0.01	0.11	0.00	0.50	0.01	0.01	0.11	0.17	0.01	0.06	0.02	0.07	0.01	0.05
C3,1	0.00	0.06	0.26	0.35	0.02	0.02	0.00	1.00	0.27	0.01	0.04	0.18	0.13	0.04	0.35	0.01	0.10	0.01	0.04	0.14	0.10	0.03	0.06	0.29	0.25	0.07	0.06	0.18	0.11	0.02	0.04	0.08	0.04
S3,1	0.00	0.09	0.16	0.45	0.00	0.01	0.00	0.27	1.00	0.05	0.01	0.01	0.16	0.02	0.21	0.33	0.02	0.06	0.10	0.11	0.03	0.04	0.02	0.45	0.35	0.05	0.00	0.14	0.04	0.02	0.02	0.08	0.11
C3,2	0.00	0.07	0.05	0.01	0.05	0.28	0.05	0.01	0.05	1.00	0.10	0.00	0.03	0.18	0.07	0.02	0.18	0.81	0.11	0.02	0.10	0.15	0.02	0.05	0.02	0.53	0.13	0.10	0.07	0.07	0.04	0.02	0.07
S3,2	0.00	0.01	0.01	0.07	0.24	0.03	0.29	0.04	0.01	0.10	1.00	0.01	0.00	0.10	0.00	0.00	0.77	0.26	0.03	0.01	0.17	0.02	0.05	0.04	0.03	0.03	0.52	0.00	0.01	0.05	0.03	0.04	0.04
C3,3	0.00	0.13	0.12	0.02	0.00	0.04	0.01	0.18	0.01	0.00	0.01	1.00	0.06	0.01	0.06	0.02	0.01	0.01	0.06	0.27	0.02	0.01	0.00	0.01	0.15	0.00	0.00	0.46	0.30	0.01	0.02	0.04	0.08
S3,3	0.01	0.12	0.04	0.13	0.02	0.05	0.02	0.13	0.16	0.03	0.00	0.06	1.00	0.00	0.05	0.02	0.05	0.06	0.20	0.06	0.02	0.06	0.05	0.16	0.02	0.01	0.01	0.26	0.43	0.05	0.02	0.13	0.02
J4	0.06	0.14	0.02	0.04	0.15	0.05	0.54	0.04	0.02	0.18	0.10	0.01	0.00	1.00	0.02	0.01	0.04	0.16	0.10	0.03	0.11	0.01	0.76	0.00	0.02	0.02	0.00	0.08	0.06	0.00	0.03	0.01	0.09
C4,1	0.00	0.12	0.56	0.14	0.04	0.02	0.05	0.35	0.21	0.07	0.00	0.06	0.05	0.02	1.00	0.30	0.01	0.06	0.06	0.31	0.03	0.07	0.05	0.52	0.50	0.17	0.01	0.15	0.22	0.07	0.07	0.04	0.02
S4,1	0.00	0.09	0.44	0.43	0.01	0.01	0.00	0.01	0.33	0.02	0.00	0.02	0.02	0.01	0.30	1.00	0.02	0.02	0.11	0.21	0.02	0.05	0.01	0.21	0.53	0.08	0.05	0.17	0.02	0.05	0.04	0.07	0.01
C4,2	0.00	0.02	0.02	0.08	0.14	0.34	0.22	0.10	0.02	0.18	0.77	0.01	0.05	0.04	0.01	0.02	1.00	0.04	0.03	0.03	0.24	0.06	0.02	0.07	0.03	0.08	0.49	0.07	0.04	0.04	0.09	0.08	0.01
S4,2	0.00	0.12	0.04	0.00	0.29	0.13	0.05	0.01	0.06	0.81	0.26	0.01	0.06	0.16	0.06	0.02	0.04	1.00	0.11	0.03	0.09	0.21	0.05	0.03	0.01	0.48	0.01	0.10	0.07	0.10	0.00	0.01	0.05
C4,3	0.00	0.02	0.04	0.17	0.01	0.05	0.09	0.04	0.10	0.11	0.03	0.06	0.20	0.10	0.06	0.11	0.03	0.11	1.00	0.03	0.00	0.03	0.01	0.16	0.02	0.06	0.02	0.46	0.70	0.02	0.01	0.07	0.14
S4,3	0.01	0.27	0.26	0.19	0.01	0.04	0.01	0.14	0.11	0.02	0.01	0.27	0.06	0.03	0.31	0.21	0.03	0.03	0.03	1.00	0.02	0.05	0.01	0.06	0.30	0.03	0.01	0.75	0.51	0.03	0.01	0.19	0.02
C4,4	0.01	0.03	0.02	0.01	0.14	0.33	0.11	0.10	0.03	0.10	0.17	0.02	0.02	0.11	0.03	0.02	0.24	0.09	0.00	0.02	1.00	0.02	0.07	0.03	0.01	0.14	0.18	0.00	0.01	0.03	0.72	0.06	0.03
S4,4	0.00	0.00	0.05	0.09	0.19	0.06	0.00	0.03	0.04	0.15	0.02	0.01	0.06	0.01	0.07	0.05	0.06	0.21	0.03	0.05	0.02	1.00	0.01	0.00	0.03	0.16	0.12	0.02	0.03	0.74	0.00	0.02	0.01
J5	0.10	0.12	0.01	0.09	0.17	0.03	0.50	0.06	0.02	0.02	0.05	0.00	0.05	0.76	0.05	0.01	0.02	0.05	0.01	0.01	0.07	0.01	1.00	0.05	0.01	0.07	0.09	0.01	0.01	0.03	0.02	0.02	0.05
C5,1	0.00	0.05	0.04	0.60	0.02	0.01	0.01	0.29	0.45	0.05	0.04	0.01	0.16	0.00	0.52	0.21	0.07	0.03	0.16	0.06	0.03	0.00	0.05	1.00	0.25	0.06	0.03	0.04	0.22	0.03	0.05	0.00	0.03
S5,1	0.00	0.03	0.62	0.02	0.03	0.01	0.01	0.25	0.35	0.02	0.03	0.15	0.02	0.02	0.50	0.53	0.03	0.01	0.02	0.30	0.01	0.03	0.01	0.25	1.00	0.07	0.03	0.23	0.23	0.02	0.02	0.06	0.01
C5,2	0.00	0.04	0.10	0.00	0.17	0.17	0.11	0.07	0.05	0.53	0.03	0.00	0.01	0.02	0.17	0.08	0.08	0.48	0.06	0.03	0.14	0.16	0.07	0.06	0.07	1.00	0.10	0.01	0.04	0.07	0.15	0.01	0.00
S5,2	0.00	0.06	0.03	0.03	0.14	0.20	0.17	0.06	0.00	0.13	0.52	0.00	0.01	0.00	0.01	0.05	0.49	0.01	0.02	0.01	0.18	0.12	0.09	0.03	0.03	0.10	1.00	0.00	0.00	0.18	0.07	0.02	0.04
C5,3	0.01	0.05	0.17	0.20	0.00	0.01	0.01	0.18	0.14	0.10	0.00	0.46	0.26	0.08	0.15	0.17	0.07	0.10	0.46	0.75	0.00	0.02	0.01	0.04	0.23	0.01	0.00	1.00	0.09	0.02	0.00	0.19	0.08
S5,3	0.00	0.06	0.17	0.05	0.01	0.04	0.06	0.11	0.04	0.07	0.01	0.30	0.43	0.06	0.22	0.02	0.04	0.07	0.70	0.51	0.01	0.03	0.01	0.22	0.23	0.04	0.00	0.09	1.00	0.01	0.01	0.05	0.09
C5,4	0.01	0.00	0.05	0.07	0.09	0.02	0.02	0.02	0.02	0.07	0.05	0.01	0.05	0.00	0.07	0.05	0.04	0.10	0.02	0.03	0.03	0.74	0.03	0.03	0.02	0.07	0.18	0.02	0.01	1.00	0.01	0.00	0.00
S5,4	0.00	0.02	0.01	0.03	0.04	0.18	0.07	0.04	0.02	0.04	0.03	0.02	0.02	0.03	0.07	0.04	0.09	0.00	0.01	0.01	0.72	0.00	0.02	0.05	0.02	0.15	0.07	0.00	0.01	0.01	1.00	0.01	0.01
C5,5	0.00	0.07	0.03	0.12	0.02	0.03	0.01	0.08	0.08	0.02	0.04	0.04	0.13	0.01	0.04	0.07	0.08	0.01	0.07	0.19	0.06	0.02	0.02	0.00	0.06	0.01	0.02	0.19	0.05	0.00	0.01	1.00	0.01
S5,5	0.01	0.07	0.04	0.08	0.05	0.09	0.05	0.04	0.11	0.07	0.04	0.08	0.02	0.09	0.02	0.01	0.01	0.05	0.14	0.02	0.03	0.01	0.05	0.03	0.01	0.00	0.04	0.08	0.09	0.00	0.01	0.01	1.00

Figure 4.11 Detail of the correlation matrix for the low degree gravity field (deg 2 to 5).

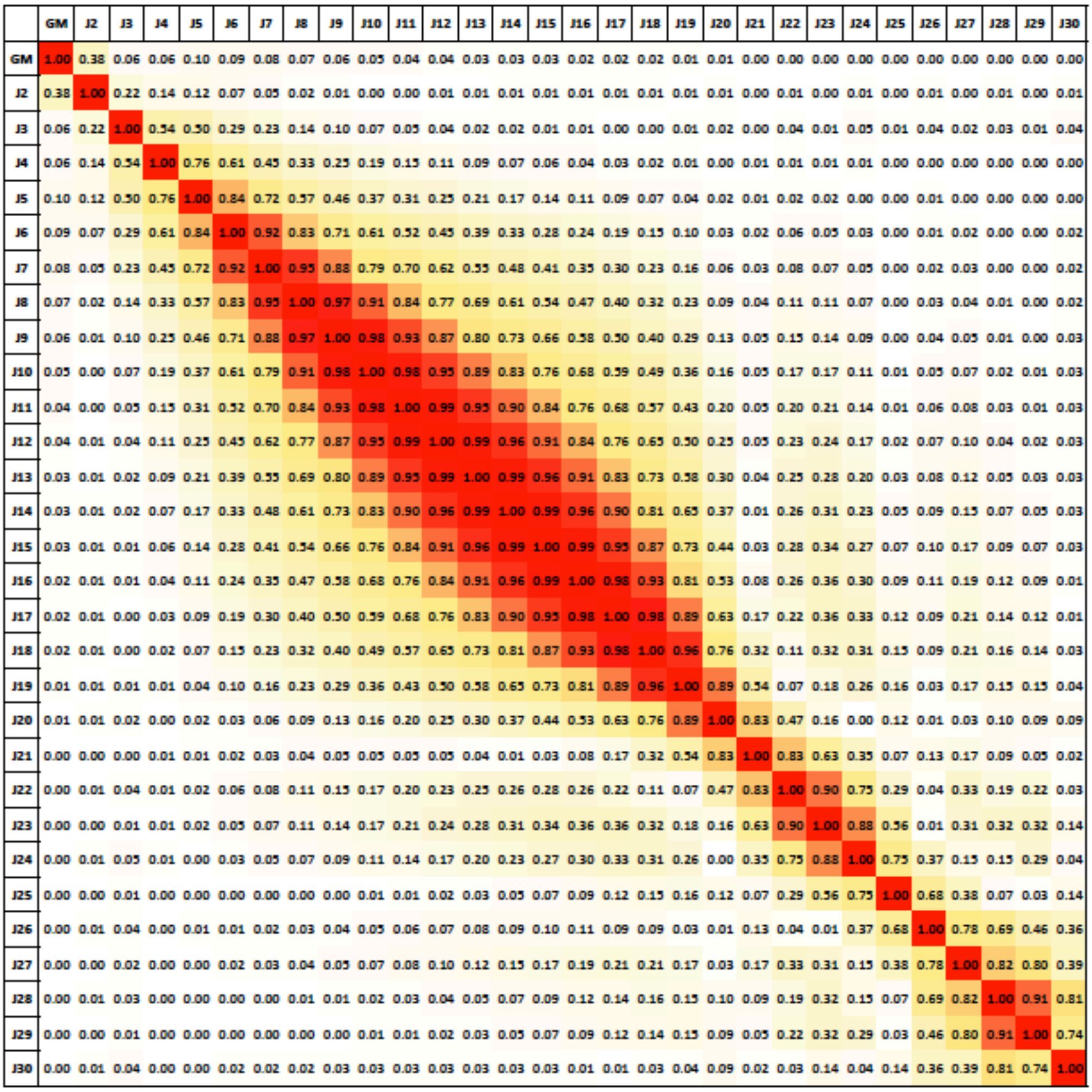

	GM	J2	J3	J4	J5	J6	J7	J8	J9	J10	J11	J12	J13	J14	J15	J16	J17	J18	J19	J20	J21	J22	J23	J24	J25	J26	J27	J28	J29	J30
GM	1.00	0.38	0.06	0.06	0.10	0.09	0.08	0.07	0.06	0.05	0.04	0.04	0.03	0.03	0.03	0.02	0.02	0.02	0.01	0.01	0.00	0.00	0.00	0.00	0.00	0.00	0.00	0.00	0.00	0.00
J2	0.38	1.00	0.22	0.14	0.12	0.07	0.05	0.02	0.01	0.00	0.00	0.01	0.01	0.01	0.01	0.01	0.01	0.01	0.01	0.01	0.00	0.01	0.00	0.01	0.00	0.01	0.00	0.01	0.00	0.01
J3	0.06	0.22	1.00	0.54	0.50	0.29	0.23	0.14	0.10	0.07	0.05	0.04	0.02	0.02	0.01	0.01	0.00	0.00	0.01	0.02	0.00	0.04	0.01	0.05	0.01	0.04	0.02	0.03	0.01	0.04
J4	0.06	0.14	0.54	1.00	0.76	0.61	0.45	0.33	0.25	0.19	0.15	0.11	0.09	0.07	0.06	0.04	0.03	0.02	0.01	0.00	0.01	0.01	0.01	0.01	0.00	0.00	0.00	0.00	0.00	0.00
J5	0.10	0.12	0.50	0.76	1.00	0.84	0.72	0.57	0.46	0.37	0.31	0.25	0.21	0.17	0.14	0.11	0.09	0.07	0.04	0.02	0.01	0.02	0.02	0.00	0.00	0.01	0.00	0.00	0.00	0.00
J6	0.09	0.07	0.29	0.61	0.84	1.00	0.92	0.83	0.71	0.61	0.52	0.45	0.39	0.33	0.28	0.24	0.19	0.15	0.10	0.03	0.02	0.06	0.05	0.03	0.00	0.01	0.02	0.00	0.00	0.02
J7	0.08	0.05	0.23	0.45	0.72	0.92	1.00	0.95	0.88	0.79	0.70	0.62	0.55	0.48	0.41	0.35	0.30	0.23	0.16	0.06	0.03	0.08	0.07	0.05	0.00	0.02	0.03	0.00	0.00	0.02
J8	0.07	0.02	0.14	0.33	0.57	0.83	0.95	1.00	0.97	0.91	0.84	0.77	0.69	0.61	0.54	0.47	0.40	0.32	0.23	0.09	0.04	0.11	0.11	0.07	0.00	0.03	0.04	0.01	0.00	0.02
J9	0.06	0.01	0.10	0.25	0.46	0.71	0.88	0.97	1.00	0.98	0.93	0.87	0.80	0.73	0.66	0.58	0.50	0.40	0.29	0.13	0.05	0.15	0.14	0.09	0.00	0.04	0.05	0.01	0.00	0.03
J10	0.05	0.00	0.07	0.19	0.37	0.61	0.79	0.91	0.98	1.00	0.98	0.95	0.89	0.83	0.76	0.68	0.59	0.49	0.36	0.16	0.05	0.17	0.17	0.11	0.01	0.05	0.07	0.02	0.01	0.03
J11	0.04	0.00	0.05	0.15	0.31	0.52	0.70	0.84	0.93	0.98	1.00	0.99	0.95	0.90	0.84	0.76	0.68	0.57	0.43	0.20	0.05	0.20	0.21	0.14	0.01	0.06	0.08	0.03	0.01	0.03
J12	0.04	0.01	0.04	0.11	0.25	0.45	0.62	0.77	0.87	0.95	0.99	1.00	0.99	0.96	0.91	0.84	0.76	0.65	0.50	0.25	0.05	0.23	0.24	0.17	0.02	0.07	0.10	0.04	0.02	0.03
J13	0.03	0.01	0.02	0.09	0.21	0.39	0.55	0.69	0.80	0.89	0.95	0.99	1.00	0.99	0.96	0.91	0.83	0.73	0.58	0.30	0.04	0.25	0.28	0.20	0.03	0.08	0.12	0.05	0.03	0.03
J14	0.03	0.01	0.02	0.07	0.17	0.33	0.48	0.61	0.73	0.83	0.90	0.96	0.99	1.00	0.99	0.96	0.90	0.81	0.65	0.37	0.01	0.26	0.31	0.23	0.05	0.09	0.15	0.07	0.05	0.03
J15	0.03	0.01	0.01	0.06	0.14	0.28	0.41	0.54	0.66	0.76	0.84	0.91	0.96	0.99	1.00	0.99	0.95	0.87	0.73	0.44	0.03	0.28	0.34	0.27	0.07	0.10	0.17	0.09	0.07	0.03
J16	0.02	0.01	0.01	0.04	0.11	0.24	0.35	0.47	0.58	0.68	0.76	0.84	0.91	0.96	0.99	1.00	0.98	0.93	0.81	0.53	0.08	0.26	0.36	0.30	0.09	0.11	0.19	0.12	0.09	0.01
J17	0.02	0.01	0.00	0.03	0.09	0.19	0.30	0.40	0.50	0.59	0.68	0.76	0.83	0.90	0.95	0.98	1.00	0.98	0.89	0.63	0.17	0.22	0.36	0.33	0.12	0.09	0.21	0.14	0.12	0.01
J18	0.02	0.01	0.00	0.02	0.07	0.15	0.23	0.32	0.40	0.49	0.57	0.65	0.73	0.81	0.87	0.93	0.98	1.00	0.96	0.76	0.32	0.11	0.32	0.31	0.15	0.09	0.21	0.16	0.14	0.03
J19	0.01	0.01	0.01	0.01	0.04	0.10	0.16	0.23	0.29	0.36	0.43	0.50	0.58	0.65	0.73	0.81	0.89	0.96	1.00	0.89	0.54	0.07	0.18	0.26	0.16	0.03	0.17	0.15	0.15	0.04
J20	0.01	0.01	0.02	0.00	0.02	0.03	0.06	0.09	0.13	0.16	0.20	0.25	0.30	0.37	0.44	0.53	0.63	0.76	0.89	1.00	0.83	0.47	0.16	0.00	0.12	0.01	0.03	0.10	0.09	0.09
J21	0.00	0.00	0.00	0.01	0.01	0.02	0.03	0.04	0.05	0.05	0.05	0.05	0.04	0.01	0.03	0.08	0.17	0.32	0.54	0.83	1.00	0.83	0.63	0.35	0.07	0.13	0.17	0.09	0.05	0.02
J22	0.00	0.01	0.04	0.01	0.02	0.06	0.08	0.11	0.15	0.17	0.20	0.23	0.25	0.26	0.28	0.26	0.22	0.11	0.07	0.47	0.83	1.00	0.90	0.75	0.29	0.04	0.33	0.19	0.22	0.03
J23	0.00	0.00	0.01	0.01	0.02	0.05	0.07	0.11	0.14	0.17	0.21	0.24	0.28	0.31	0.34	0.36	0.36	0.32	0.18	0.16	0.63	0.90	1.00	0.88	0.56	0.01	0.31	0.32	0.32	0.14
J24	0.00	0.01	0.05	0.01	0.00	0.03	0.05	0.07	0.09	0.11	0.14	0.17	0.20	0.23	0.27	0.30	0.33	0.31	0.26	0.00	0.35	0.75	0.88	1.00	0.75	0.37	0.15	0.15	0.29	0.04
J25	0.00	0.00	0.01	0.00	0.00	0.00	0.00	0.00	0.00	0.01	0.01	0.02	0.03	0.05	0.07	0.09	0.12	0.15	0.16	0.12	0.07	0.29	0.56	0.75	1.00	0.68	0.38	0.07	0.03	0.14
J26	0.00	0.01	0.04	0.00	0.01	0.01	0.02	0.03	0.04	0.05	0.06	0.07	0.08	0.09	0.10	0.11	0.09	0.09	0.03	0.01	0.13	0.04	0.01	0.37	0.68	1.00	0.78	0.69	0.46	0.36
J27	0.00	0.00	0.02	0.00	0.00	0.02	0.03	0.04	0.05	0.07	0.08	0.10	0.12	0.15	0.17	0.19	0.21	0.21	0.17	0.03	0.17	0.33	0.31	0.15	0.38	0.78	1.00	0.82	0.80	0.39
J28	0.00	0.01	0.03	0.00	0.00	0.00	0.00	0.01	0.01	0.02	0.03	0.04	0.05	0.07	0.09	0.12	0.14	0.16	0.15	0.10	0.09	0.19	0.32	0.15	0.07	0.69	0.82	1.00	0.91	0.81
J29	0.00	0.00	0.01	0.00	0.00	0.00	0.00	0.00	0.00	0.01	0.01	0.02	0.03	0.05	0.07	0.09	0.12	0.14	0.15	0.09	0.05	0.22	0.32	0.29	0.03	0.46	0.80	0.91	1.00	0.74
J30	0.00	0.01	0.04	0.00	0.00	0.02	0.02	0.02	0.03	0.03	0.03	0.03	0.03	0.03	0.03	0.01	0.01	0.03	0.04	0.09	0.02	0.03	0.14	0.04	0.14	0.36	0.39	0.81	0.74	1.00

Figure 4.12 Detail of the correlation matrix for zonal coefficients. Note the high correlation spot starting at J4.

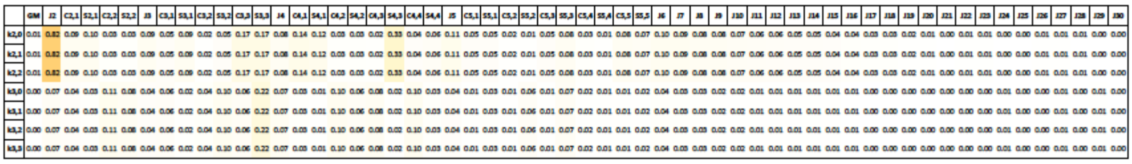

Figure 4.13 Detail of the correlation matrix for Love numbers.

Largely distributed correlations are an index of information dispersion that causes large values of the uncertainties of the estimated parameters.

In circular orbit cases one of the possible approaches is to define a new basis of functions that preserves locally the orthonormal property on the sampled region of the sphere. This basis is called Slepian basis (Albertella *et al.*, 1999). The basis is localized only at a fixed distance from the planet. This approach is not applicable to the Juno case since the orbit is highly elliptical and consequently the jovicentric radius changes continuously during the tracking pass.

Another possible approach is to define local mass anomalies (e.g. ring mass concentrations) whose mission is to absorb the high degree zonal gravity signal. This technique might result particularly expensive if longitudinal variations of the gravity field must be taken into account.

A more practical approach is to build a Singular Value Decomposition filter, which eliminates from the estimation the unobservable linear combination of parameters.

Figure 4.14, Figure 4.15, Figure 4.16, Figure 4.17 show the results for the gravity spectrum of the low degree tesseral coefficients. The results are also reported in Table 4.13.

Parameter	Formal uncertainty	Estimation Error	Estimated value
J2	$2.02 \cdot 10^{-10}$	$-3.78 \cdot 10^{-11}$	$6.57300335696616 \cdot 10^{-3}$
C2,1	$9.42 \cdot 10^{-11}$	$5.53 \cdot 10^{-11}$	$-5.52509549062068 \cdot 10^{-11}$
S2,1	$1.15 \cdot 10^{-10}$	$-3.52 \cdot 10^{-11}$	$3.52421007269847 \cdot 10^{-11}$
C2,2	$2.77 \cdot 10^{-10}$	$-3.54 \cdot 10^{-10}$	$3.53698797709013 \cdot 10^{-10}$
S2,2	$2.64 \cdot 10^{-10}$	$1.47 \cdot 10^{-10}$	$-1.47016657238934 \cdot 10^{-10}$
J3	$1.62 \cdot 10^{-10}$	$2.19 \cdot 10^{-11}$	$-2.19424688710042 \cdot 10^{-8}$
C3,1	$6.92 \cdot 10^{-11}$	$-2.96 \cdot 10^{-11}$	$2.96421488643824 \cdot 10^{-11}$
S3,1	$6.07 \cdot 10^{-11}$	$4.25 \cdot 10^{-11}$	$-4.24588420382452 \cdot 10^{-11}$
C3,2	$1.96 \cdot 10^{-10}$	$2.83 \cdot 10^{-10}$	$-2.83002003785853 \cdot 10^{-10}$
S3,2	$1.87 \cdot 10^{-10}$	$-2.47 \cdot 10^{-10}$	$2.47416348744034 \cdot 10^{-10}$
C3,3	$1.15 \cdot 10^{-10}$	$7.05 \cdot 10^{-11}$	$-7.04635971432487 \cdot 10^{-11}$

S3,3	$1.20 \cdot 10^{-10}$	$4.33 \cdot 10^{-11}$	$-4.33364645217834 \cdot 10^{-11}$
J4	$1.08 \cdot 10^{-10}$	$-4.29 \cdot 10^{-11}$	$-1.95708014002502 \cdot 10^{-4}$
C4,1	$9.82 \cdot 10^{-11}$	$-1.65 \cdot 10^{-11}$	$1.64577298567752 \cdot 10^{-11}$
S4,1	$8.69 \cdot 10^{-11}$	$5.92 \cdot 10^{-11}$	$-5.92019866084788 \cdot 10^{-11}$
C4,2	$8.26 \cdot 10^{-11}$	$4.89 \cdot 10^{-11}$	$-4.88908295743290 \cdot 10^{-11}$
S4,2	$9.50 \cdot 10^{-11}$	$2.81 \cdot 10^{-11}$	$-2.80716347040418 \cdot 10^{-11}$
C4,3	$1.24 \cdot 10^{-10}$	$-1.90 \cdot 10^{-11}$	$1.90477444878097 \cdot 10^{-11}$
S4,3	$1.42 \cdot 10^{-10}$	$-1.48 \cdot 10^{-10}$	$1.47991388048020 \cdot 10^{-10}$
C4,4	$7.05 \cdot 10^{-11}$	$-1.56 \cdot 10^{-10}$	$1.56280926583448 \cdot 10^{-10}$
S4,4	$6.64 \cdot 10^{-11}$	$8.39 \cdot 10^{-11}$	$-8.38519398704783 \cdot 10^{-11}$
J5	$1.76 \cdot 10^{-10}$	$-1.67 \cdot 10^{-10}$	$9.23303568556361 \cdot 10^{-10}$
C5,1	$8.04 \cdot 10^{-11}$	$-1.11 \cdot 10^{-10}$	$1.11182326108961 \cdot 10^{-10}$
S5,1	$7.11 \cdot 10^{-11}$	$-5.42 \cdot 10^{-11}$	$5.42395303668732 \cdot 10^{-11}$
C5,2	$5.33 \cdot 10^{-11}$	$-4.57 \cdot 10^{-11}$	$4.56833452823353 \cdot 10^{-11}$
S5,2	$5.71 \cdot 10^{-11}$	$1.23 \cdot 10^{-10}$	$-1.23362010768213 \cdot 10^{-10}$
C5,3	$8.15 \cdot 10^{-11}$	$8.04 \cdot 10^{-11}$	$-8.03518277276331 \cdot 10^{-11}$
S5,3	$7.77 \cdot 10^{-11}$	$6.04 \cdot 10^{-11}$	$-6.03847833293863 \cdot 10^{-11}$
C5,4	$5.37 \cdot 10^{-11}$	$-4.06 \cdot 10^{-11}$	$4.05811944422247 \cdot 10^{-11}$
S5,4	$5.33 \cdot 10^{-11}$	$-1.64 \cdot 10^{-10}$	$1.64440467913456 \cdot 10^{-10}$
C5,5	$3.35 \cdot 10^{-11}$	$-1.60 \cdot 10^{-11}$	$1.59910249131640 \cdot 10^{-11}$
S5,5	$3.27 \cdot 10^{-11}$	$9.60 \cdot 10^{-13}$	$-9.59582467016234 \cdot 10^{-13}$

Table 4.13 Low degree tesseral gravity spectrum estimation results.

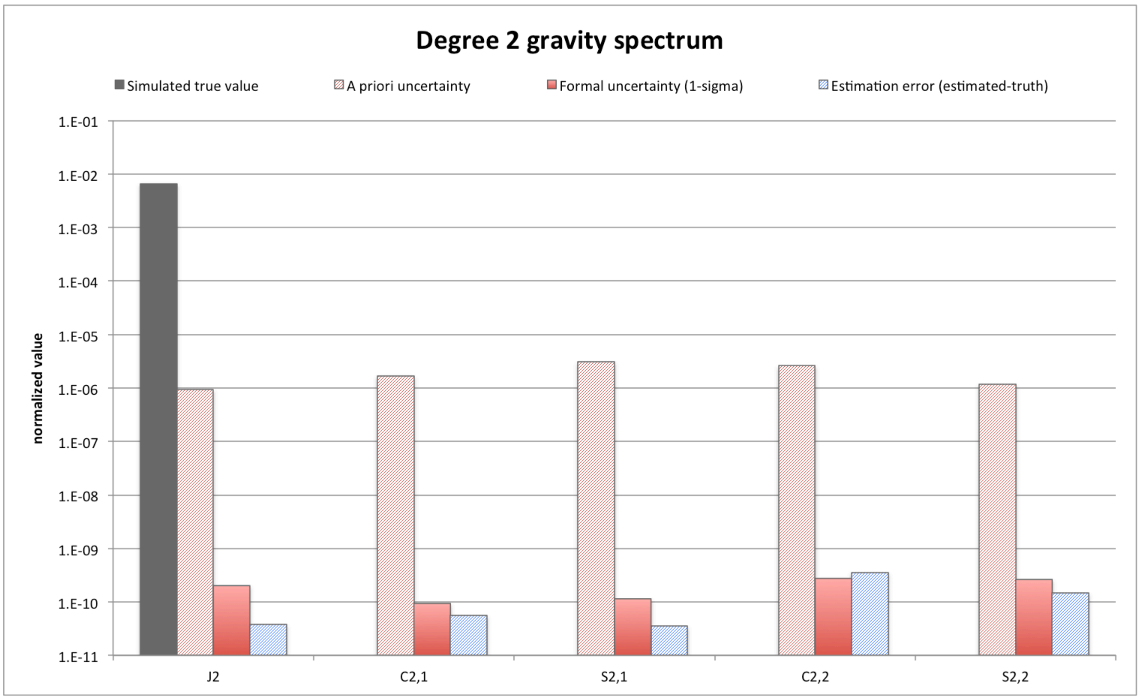

Figure 4.14 Full degree 2 gravity spectrum.

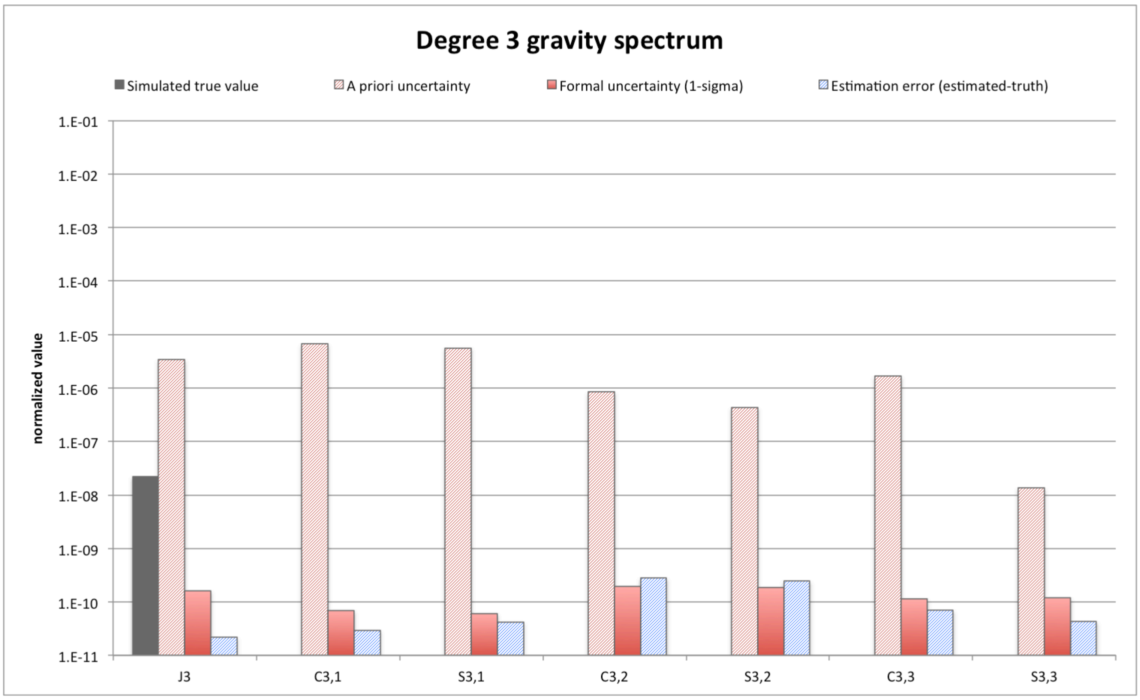

Figure 4.15 Full degree 3 gravity spectrum.

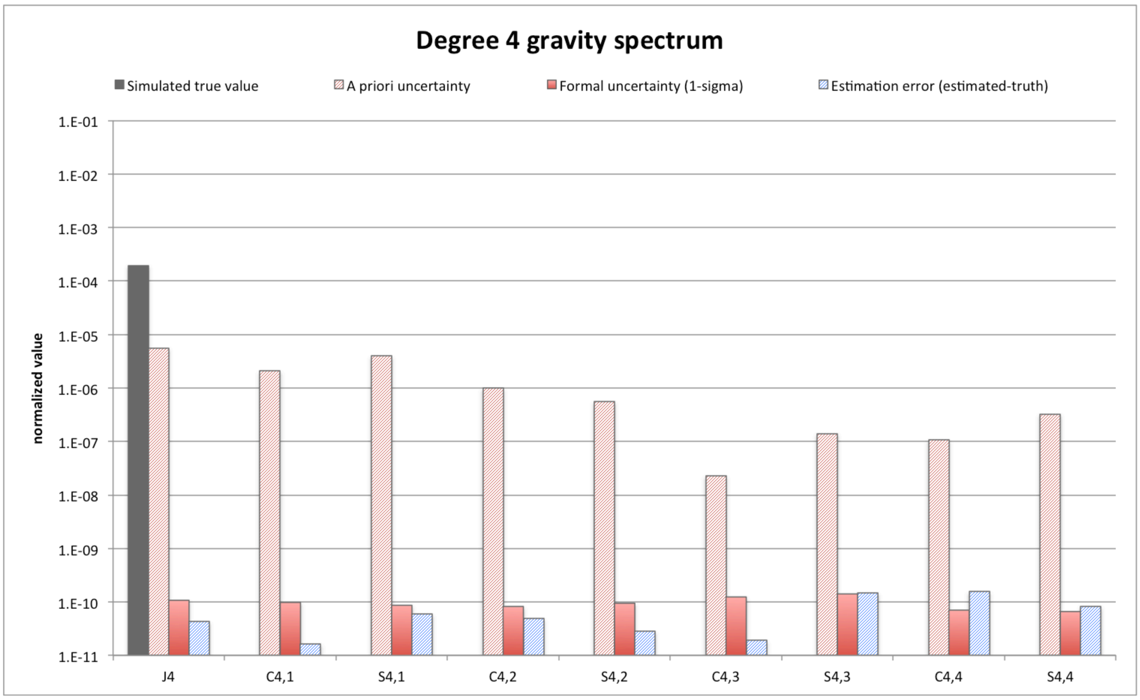

Figure 4.16 Full degree 4 gravity spectrum.

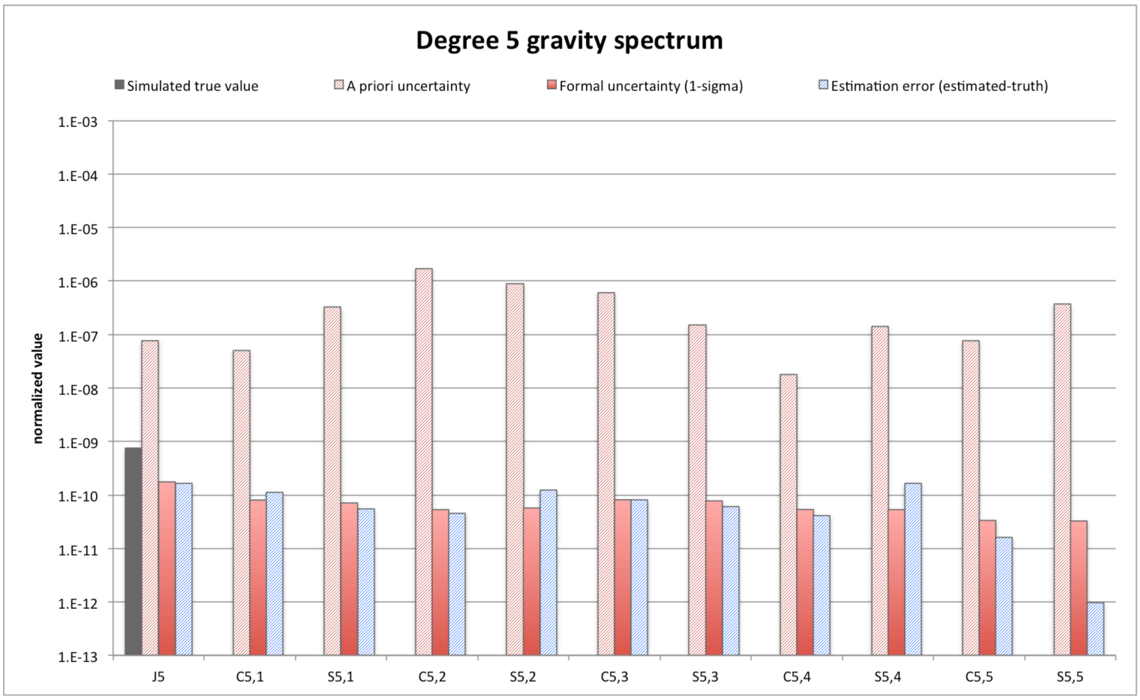

Figure 4.17 Full degree 5 gravity spectrum.

The low degrees normalized 1-sigma formal uncertainty is at a level of 10^{-10}. The tesseral coefficients are simulated with a null value. If Jupiter will show low degrees normalized tesseral harmonics larger than 10^{-10}, these will be correctly determined and absorbed. Estimating the tesseral coefficients causes a dispersion of the data information on a larger number of parameters and consequently larger overall uncertainties. If the tesseral gravity field will be significantly large even at high degrees and a larger number of them must be included in the estimation, the formal uncertainties of all the parameters could worsen even by order of magnitudes (up to a priori saturation).

The knowledge of the GM of Jupiter is not improved by the experiment. The formal uncertainty is practically equal to the a priori uncertainty (cf. Table 4.14).

Parameter	Formal uncertainty	Estimation Error	Estimated value
GM (km^3/s^2)	1.98	-0.225	$1.26712765063660 \cdot 10^8$

Table 4.14 Jupiter System GM estimation results.

Table 4.15 and Figure 4.18 show the estimation results for the Love numbers.

Parameter	Formal uncertainty	Estimation Error	Estimated value
k_2	$2.56 \cdot 10^{-3}$	$5.63 \cdot 10^{-4}$	$5.29437303684238 \cdot 10^{-1}$
k_3	$4.54 \cdot 10^{-3}$	$-1.78 \cdot 10^{-4}$	$2.00178224136132 \cdot 10^{-1}$

Table 4.15 Love numbers estimation results.

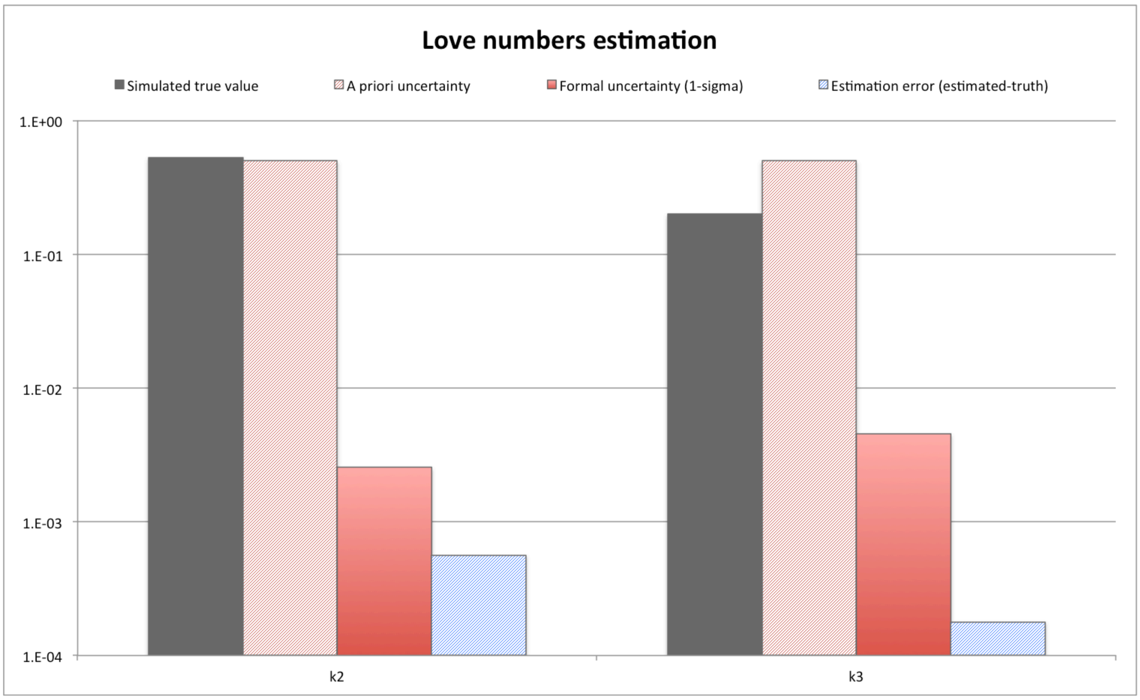

Figure 4.18 Love numbers estimation details.

The tidal deformation produces a velocity perturbation that is mainly directed orthogonally to the orbit plane. Most of the signal is therefore aligned with line-of-sight direction leading to a very good determination of these coefficients.

The gravity field estimation results can also be represented in terms of surface gravity uncertainty. The representation in the spatial scale has the advantage of collecting the information distributed among several parameters into a single scalar function independent from the basis of functions chosen to describe the gravity field.

The surface gravity 1-sigma uncertainty is presented in Figure 4.19 while Figure 4.20 shows the estimation error.

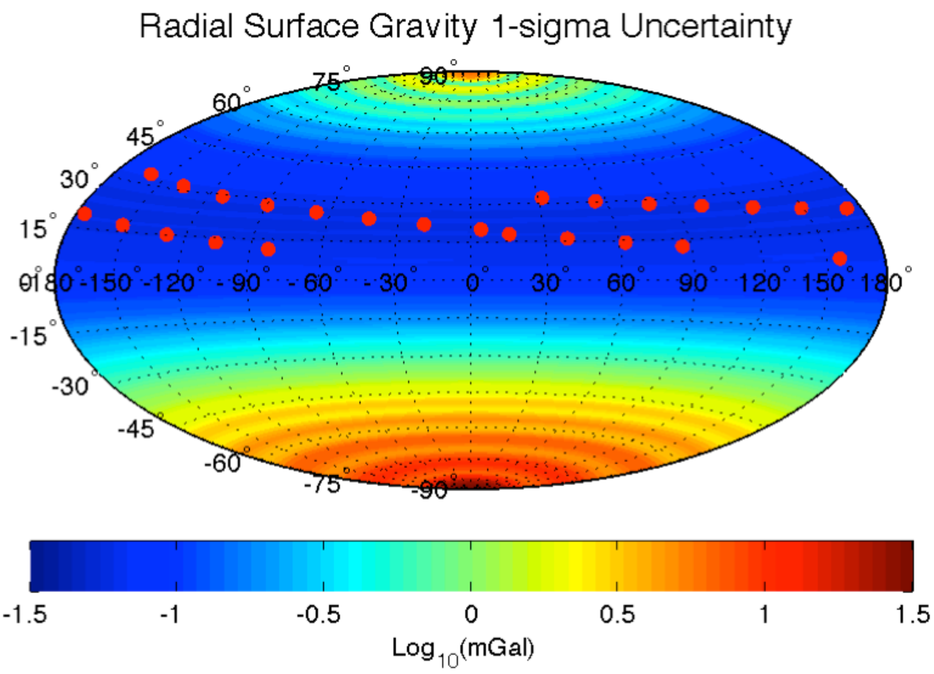

Figure 4.19 Radial surface gravity 1-sigma uncertainty. The color scale is log. Red dots mark the pericenters locations.

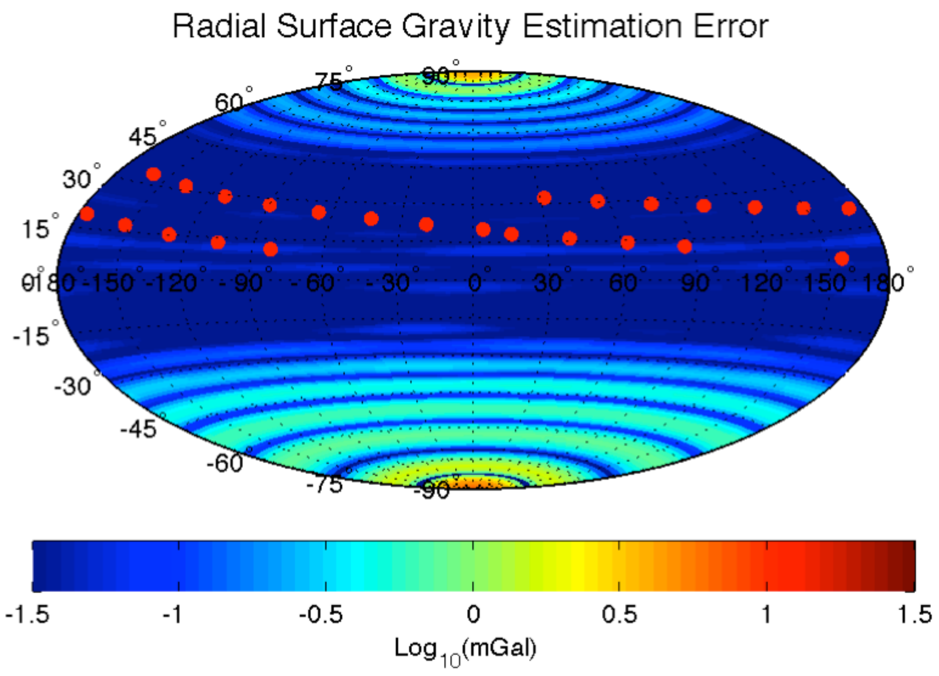

Figure 4.20 Radial surface gravity estimation error (absolute value). The color scale is log. Red dots mark the pericenters locations.

It is evident from the uncertainty plot that the accuracy has a minimum located in the latitude belt 6.5° to 33°, where pericenters are concentrated. The uncertainty increases rapidly moving from the minimum towards the poles. The maximum uncertainty is at the south pole, since the latitude belt covered by Juno is located entirely in the northern hemisphere. The estimation error is compliant with the uncertainties, in particular in the minimum uncertainty region where a very accurate reconstruction of the surface gravity field is possible.

Zonal winds induced gravity anomalies of the order of 1 mGal can be easily detected in the region of minimum uncertainty. If the gravity anomalies will be smaller the measurement will be too uncertain. Small gravity anomalies may require a smaller estimated parameter set to fit the data, since high degrees zonal coefficients might be too small to cause any perturbation on the Doppler signal. This would lead to smaller surface gravity uncertainties that could enable the observation of the zonal winds signal. On the other hand, data fitting might require a larger number of tesseral and sectoral coefficients in the estimated parameters set. This would have a negative effect on the uncertainty on the reconstructed gravity since it would amplify the information dispersion.

The estimation strategy is strongly dependent on the expected shape and magnitude of the gravity field. At the moment the indications from geophysicist do not offer enough constraints. It is impossible at the moment to return a definitive prediction of the uncertainty expected from the Juno gravity experiment. The presented analysis is based on reasonable geophysical assumptions and is at the moment the best prediction possible.

5 Angular Momentum estimate by Lense-Thirring precession

5.1 The Lense-Thirring effect

In Newton's mechanics a body rotates or not with respect to an absolute fixed space. Ernst Mach proposed a different view eliminating the concept of absolute space. The rotational state of a body is defined by the rotational state of the other bodies in the universe, that is a body rotates or not with respect to the other bodies in the universe. This is called the Mach's principle and was an inspiring idea for Albert Einstein in the formulation of General Relativity. According to Newton, a body spinning in the proximity of a rotating central mass does not experience any acceleration but the gravitational attraction and therefore its plane of rotation remains constant. On the other hand, general relativity states that the rotation of the central body modifies the surrounding space-time and therefore alters the rotation plane of the spinning body.

The *Lense-Thirring precession* or *frame dragging* is the relativistic effect that describes the interaction between a rotating mass and the surrounding space-time.

In the weak field and slow motion approximation, the non-linear Einstein field equations can be linearized to resemble the linear equations of electromagnetism. The mass density takes the place of charge density while the mass current density plays the analogue of the charge current densities. There are differences due to the fact that gravity is mediated by a spin-two field and is only attractive while a spin-one field mediates electromagnetism (attractive and repulsive) (Chashchina *et al.*, 2009).

Defining with $\vec{E}$ the gravitoelectric field and with $\vec{H}$ the gravitomagnetic one the gravitational analogue of the Maxwell equations is (Chashchina *et al.*, 2009) :

$$\begin{aligned}
&\nabla\cdot\vec{E}=-4\pi G\rho,\\
&\nabla\times\vec{E}=0,\\
&\nabla\cdot\vec{H}=0,\\
&\nabla\times\vec{H}=4\left[-4\pi G\frac{\rho\vec{v}}{c}+\frac{1}{c}\frac{\partial\vec{E}}{\partial t}\right].
\end{aligned}$$

The Lense-Thirring effect is a manifestation of the gravitomagnetic field and can be considered as the gravitational analogue of the Lorentz force, that is a force orthogonal to the direction of the mass current (angular momentum, $\vec{J}$) generating the gravitomagnetic field and to the velocity of the test mass (ODP User's Manual v.1, p. 89):

$$\ddot{\vec{r}}_{LT}=\frac{(1+\gamma)G\left|\vec{J}\right|}{c^2r^3}\left[\frac{3}{r^2}(\vec{r}\times\vec{v})\left(\vec{r}\cdot\hat{P}\right)+\left(\vec{v}\times\hat{P}\right)\right]$$

where

$\vec{r},\vec{v}$	planetocentric coordinates of the test mass
c	speed of light
$\hat{P}$	direction of the planet north pole
$\vec{J}$	planet angular momentum vector

γ General Relativity γ parameter

G universal gravitational constant

The net effect of this acceleration is a precession of the rotation plane of the gyroscope, in the direction of the rotation of the central body.

The Lense-Thirring effect has been measured with the LAGEOS satellites in Earth orbit with an accuracy of nearly 10% of the value predicted by General Relativity (Ciufolini *et al.*, 2006). The measurement consists in the determination of the sum of the nodes of two counter-rotating satellites (LAGEOS and LAGEOS 2). This approach allows decoupling the precession due to the Lense-Thirring effect from the precession due to the gravity field. The estimate is going to be improved thanks to the recent launch of the LARES satellite (February, 2012).

5.1.1 Lense-Thirring precession of the Juno orbit

Jupiter is the most massive body of the solar system, apart from the Sun, and it is characterized by a very fast rotation period (9.925 hours). Given a Jupiter polar moment of inertia $\left(C/MR^2\right)$ it is possible to derive the angular momentum. In Table 5.1 are reported two different estimates of the angular momentum:

C/MR^2	**Angular momentum (kg km^{-2} s^{-1})**	**Reference**
0.26401	$4.5041 \cdot 10^{32}$	(Hubbard *et al.*, 1989, Table II)
0.40000	$6.8242 \cdot 10^{32}$	(Soffel *et al.*, 2003)

Table 5.1 Jupiter angular momentum.

The Juno orbit about Jupiter makes it particularly sensitive to the frame dragging. The high velocity at pericenter (nearly 60 km/s) combined with a relatively low pericenter altitude (3000 – 5000 km) makes the Lense-Thirring acceleration acting on Juno nearly 3000 times greater than that experienced by the LAGEOS satellites in Earth orbit even if concentrated only at the pericenter.

The approach used with the LAGEOS satellites is not applicable to the Juno spacecraft. The orbit trim maneuvers (OTM) and the repointing maneuvers destroy the dynamical coherence of the Juno trajectory. Therefore, it is not possible to estimate the total displacement of the node of the orbit over one year of mission, as initially proposed by L. Iorio (Iorio, 2010).

In order to get the sensitivity of the relativistic effect on the Doppler signal, two trajectories were compared. One of the two trajectories was integrated taking into account the Lense-Thirring effect, while the second one did not include it. The velocity difference between the two trajectories, projected along the line of sight with the Earth is reported in Figure 5.1.

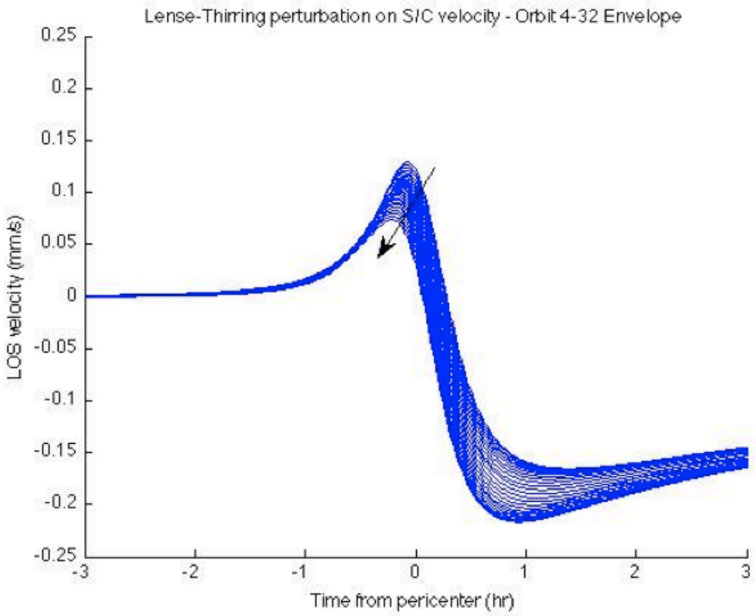

Figure 5.1 Projection on the line of sight of the velocity variation due to the Lense-Thirring effect. The plot shows a curve for each pericenter pass from orbit 4 to 32 (arrow direction).

The mean peak-to-peak signal is 0.35 mm/s, which is much greater than the instrument sensitivity. The detection of this relativistic signal is aided by the fact that the velocity variation is orthogonal to the orbit plane and therefore is mainly directed along the line of sight with the Earth.

It is not possible to set up a general relativity to probe the Lense-Thirring effect with the Juno mission, because of the large uncertainties on the Jupiter angular momentum and gravity field. The assessment of the magnitude of the acceleration (that is detecting any violation of General Relativity) cannot be decoupled by the estimate of the angular momentum, without an independent measurement of this last quantity. On the other hand, it is possible to assume that the General Relativity is the correct theory of gravitation and therefore using the Lense-Thirring signal to estimate the Jupiter angular momentum. If an independent measurement of the Jupiter angular momentum (e.g. from the determination of the polar precession constant) will show up in the future, then it would be possible to read the Juno estimate as a General Relativity test.

The goal of this section is to assess the uncertainties attainable in the estimation of the angular momentum of Jupiter.

5.2 Correction to the Orbit Determination process

The DPTRAJ-ODP integrates the spacecraft trajectory in a relativistic reference frame centered on the barycenter of the Jupiter system. The relativistic metric tensor does not account for the off-diagonal components responsible for the Lense-Thirring precession. Hence, it is necessary to include an apparent acceleration that corrects the spacecraft trajectory, and to adjust the orbit determination problem mathematical formulation (cf. Section 3.4.1) in order to consider dynamical models not included in the standard trajectory integration. This step is necessary since the DPTRAJ-ODP is no more going to be updated from the JPL's Navigation Software Group since all the efforts are currently being spent in the transition to the new orbit determination code MONTE (cf. Section 3.4.4). Nor it can be done in first person since the source code distribution is strictly subjected to the ITAR (International Traffic in Arms Regulation).

A second modification is required in order to estimate the Jupiter angular momentum since the DPTRAJ-ODP does not allow its estimation (as obvious, since it does not include the Lense-Thirring acceleration model). Hence some effort must be spent in computing the partial derivatives of the observables with respect to angular momentum.

5.2.1 Trajectory corrections

Let us consider two trajectories X^* and X. The first is the trajectory integrated by DPTRAJ-ODP with its standard models, while the second is a trajectory integrated considering all the standard dynamical models plus the Lense-Thirring small perturbation.

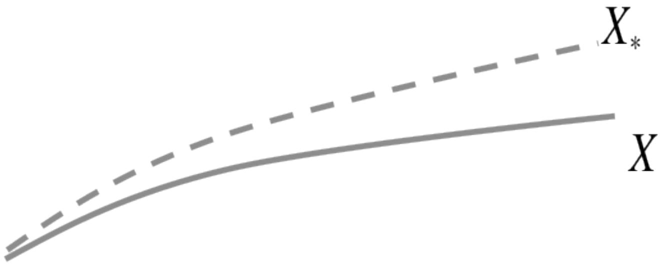

Figure 5.2 Trajectory deviation because of the Lense-Thirring perturbation. X^* is the nominal DPTRAJ-ODP integrated trajectory, while X is the trajectory integrated considering the Lense-Thirring effect.

The differential equations describing the two trajectories are:

$$\dot{X}^* = F\left(X^*, t\right)$$
$$\dot{X} = F\left(X, t\right) + a_{LT}\left(X, t\right)$$

The solution to the first equation is an output of DPTRAJ-ODP while it is impossible to integrate directly the second equation. Assuming that the Lense-Thirring perturbation is small relatively to the gravitational accelerations (it is actually 10 times smaller than the smallest gravitational perturbation, the tidal deformation), it is possible to linearize the second equation onto the solution of the first one.

$$\dot{X} = \underbrace{F\left(X^*,t\right)}_{\dot{X}^*} + a_{LT}\left(X^*,t\right) + \left.\frac{\partial\left(F + a_{LT}\right)}{\partial X}\right|_* \left(X - X^*\right)$$

Passing to the corrections:

$$\dot{x} = \left(\dot{X} - \dot{X}^*\right) = \left.\frac{\partial\left(F + a_{LT}\right)}{X}\right|_* x + a_{LT}\left(X^*,t\right) = Mx + a_{LT}\left(X^*,t\right)$$

Differently from section 3.4.1 this equation is not homogeneous. Its integral is constituted by the solution of the homogeneous equation plus a particular solution

$$x\left(t\right) = \Phi_{LT}\left(t,t_0\right)x_0 + x_P.$$

5.2.1.1 Solution of the homogeneous equation: variational equations integration

The solution of the homogeneous equation $\dot{x} = \left.\frac{\partial F}{\partial X}\right|_* x$ is generally computed in the form $x\left(t\right) = \Phi\left(t,t_0\right)x_0$.

Define q as the vector of the parameters

$$q = \begin{bmatrix} X \\ \cdots \\ a \end{bmatrix} \qquad X = \begin{bmatrix} r \\ \cdots \\ \dot{r} \end{bmatrix}$$

subdivided in state vector parameters X (r is the jovicentric position) and non-state parameters a. When evaluated at the initial epoch these quantities are written as

$$q_0 = \begin{bmatrix} X_0 \\ \cdots \\ a \end{bmatrix} \qquad X_0 = \begin{bmatrix} r_0 \\ \cdots \\ \dot{r}_0 \end{bmatrix}.$$

The state transition matrix takes the form

$$\Phi(t,t_0)=\frac{\partial q}{\partial q_0}=\begin{bmatrix}\frac{\partial X}{\partial X_0} & \frac{\partial X}{\partial a}\\ \frac{\partial a}{\partial X_0} & \frac{\partial a}{\partial a}\end{bmatrix}=\begin{bmatrix}\frac{\partial X}{\partial X_0} & \frac{\partial X}{\partial a}\\ 0 & I\end{bmatrix}=\begin{bmatrix}\left[\frac{\partial X}{\partial q_0}\right]\\ 0 \quad I\end{bmatrix}$$

The derivative of the state vector X with respect to the parameters vector q_0 is the result of the integration of the acceleration partials (Moyer, 1971):

$$\ddot{r}=\ddot{r}(r,\dot{r},q_0)$$

$$\frac{\partial\ddot{r}}{\partial q_0}=\frac{\partial\ddot{r}}{\partial r}\frac{\partial r}{\partial q_0}+\frac{\partial\ddot{r}}{\partial\dot{r}}\frac{\partial\dot{r}}{\partial q_0}+\left.\frac{\partial\ddot{r}}{\partial q_0}\right|_{r,\dot{r}=const}$$

Let

$$Z=\frac{\partial r}{\partial q_0}\quad ;\quad A=\frac{\partial\ddot{r}}{\partial r}\quad ;\quad B=\frac{\partial\ddot{r}}{\partial\dot{r}}\quad ;\quad C=\left.\frac{\partial\ddot{r}}{\partial q_0}\right|_{r,\dot{r}=const}$$

$$\ddot{Z}=AZ+B\dot{Z}+C\qquad\Rightarrow\qquad\frac{\partial\dot{X}}{\partial q_0}=\begin{bmatrix}\frac{\partial\dot{r}}{\partial q_0}\\ \cdots\\ \frac{\partial\ddot{r}}{\partial q_0}\end{bmatrix}=\begin{bmatrix}\dot{Z}\\ \cdots\\ \ddot{Z}\end{bmatrix}=\begin{bmatrix}0 & I\\ A & B\end{bmatrix}\begin{bmatrix}Z\\ \cdots\\ \dot{Z}\end{bmatrix}+\begin{bmatrix}0\\ \cdots\\ C\end{bmatrix}$$

This equation is integrated with initial conditions

$$\left.\frac{\partial X}{\partial q_0}\right|_0=\begin{bmatrix}\frac{\partial X}{\partial X_0} & \vdots & \frac{\partial X}{\partial a}\end{bmatrix}_0=\begin{bmatrix}I & \vdots & 0\end{bmatrix}.$$

When considering the additional Lense-Thirring acceleration the differential equation of the acceleration partials becomes:

$$\ddot{r} = F(X,q_0,t) + a_{LT}(X,q_0,t)$$

$$\frac{\partial \ddot{r}}{\partial q_0} = \frac{\partial\left(F + a_{LT}\right)}{\partial r}\frac{\partial r}{\partial q_0} + \frac{\partial\left(F + a_{LT}\right)}{\partial \dot{r}}\frac{\partial \dot{r}}{\partial q_0} + \left.\frac{\partial\left(F + a_{LT}\right)}{\partial q_0}\right|_{r,\dot{r}=const}$$

The DPTRAJ-ODP allows the access to the A, B, and C matrices at each epoch. These matrices must be corrected for the additional terms coming from the Lense-Thirring acceleration model.

Let

$$\tilde{A} = \frac{\partial\left(F + a_{LT}\right)}{\partial r} = A + \frac{\partial a_{LT}}{\partial r} = A + \Delta A$$

$$\tilde{B} = \frac{\partial\left(F + a_{LT}\right)}{\partial \dot{r}} = B + \frac{\partial a_{LT}}{\partial \dot{r}} = B + \Delta B$$

$$\tilde{C} = \left.\frac{\partial\left(F + a_{LT}\right)}{\partial q_0}\right|_{r,\dot{r}=const} = B + \left.\frac{\partial a_{LT}}{\partial q_0}\right|_{r,\dot{r}=const} = C + \Delta C$$

The variational equations can now be rewritten as

$$\begin{bmatrix} \dot{Z} \\ \cdots \\ \ddot{Z} \end{bmatrix} = \begin{bmatrix} 0 & I \\ A + \Delta A & B + \Delta B \end{bmatrix} \begin{bmatrix} Z \\ \cdots \\ \dot{Z} \end{bmatrix} + \begin{bmatrix} 0 \\ \cdots \\ C + \Delta C \end{bmatrix}.$$

In order to compute the partial derivatives of the trajectory with respect to the Jupiter angular momentum, the q vector must be extended

$$q' = \begin{bmatrix} q \\ \cdots \\ J \end{bmatrix} \quad ; \quad Z' = \frac{\partial X}{\partial q'}$$

$$C' = \begin{bmatrix} C & \vdots & \left.\dfrac{\partial F}{\partial J}\right|_{r,\dot{r}=const} \end{bmatrix} = \begin{bmatrix} C & \vdots & 0 \end{bmatrix} \quad ; \quad \Delta C' = \begin{bmatrix} \Delta C & \vdots & \left.\dfrac{\partial a_{LT}}{\partial J}\right|_{r,\dot{r}=const} \end{bmatrix}$$

The initial conditions for the integration do not change.

The matrices $\Delta A, \Delta B$ are straightforwardly computed using the dyadic form:

$$\vec{a}_{LT} = \frac{(1+\gamma)}{c^2 r^3} GJ\left[\frac{3}{r^2}\left(\vec{r}^T\hat{P}\right)\left(\underline{\underline{\times\vec{v}}}\cdot\vec{r}\right)+\left(\underline{\underline{\times\hat{P}}}\cdot\vec{v}\right)\right]$$

$$\Delta A_{LT} = \frac{\partial\vec{a}_{LT}}{\partial\vec{r}} = -\frac{3(1+\gamma)}{c^2 r^5} GJ\left[\frac{5}{r^2}\left(\vec{r}^T\hat{P}\right)\left(\underline{\underline{\times\vec{v}}}\cdot\vec{r}\right)\vec{r}^T-\left(\underline{\underline{\times\vec{v}}}\cdot\vec{r}\right)\hat{P}^T-\left(\vec{r}^T\hat{P}\right)\underline{\underline{\times\vec{v}}}+\left(\underline{\underline{\times\hat{P}}}\cdot\vec{v}\right)\vec{r}^T\right]$$

$$\Delta B_{LT} = \frac{\partial\vec{a}_{LT}}{\partial\dot{\vec{r}}} = -\frac{(1+\gamma)}{c^2 r^5} GJ\left[-\frac{3}{r^2}\left(\vec{r}^T\hat{P}\right)\underline{\underline{\times\vec{r}}}+\underline{\underline{\times\hat{P}}}\right]$$

The matrix ΔC is generally null except for the angular momentum J and pole location parameters $\left(\alpha_0, \dot{\alpha}_0, \delta_0, \dot{\delta}_0, W_0, \dot{W}_0\right)$.

$$\Delta C_J = \left.\frac{\partial\vec{a}_{LT}}{\partial J}\right|_{r,\dot{r}=const} = \frac{(1+\gamma)}{c^2 r^3} G\left[\frac{3}{r^2}\left(\vec{r}^T\hat{P}\right)\left(\underline{\underline{\times\vec{v}}}\cdot\vec{r}\right)+\left(\underline{\underline{\times\hat{P}}}\cdot\vec{v}\right)\right]$$

$$\Delta C_{\alpha_0} = \left.\frac{\partial\vec{a}_{LT}}{\partial\alpha_0}\right|_{r,\dot{r}=const} = \frac{(1+\gamma)}{c^2 r^3} GJ\left[\frac{3}{r^2}\left(\underline{\underline{\times\vec{v}}}\cdot\vec{r}\right)\vec{r}^T-\underline{\underline{\times\vec{v}}}\right]\begin{bmatrix}-\sin\left(\alpha_0+\dot{\alpha}_0 t\right)\cos\left(\delta_0+\dot{\delta}_0 t\right)\\ \cos\left(\alpha_0+\dot{\alpha}_0 t\right)\cos\left(\delta_0+\dot{\delta}_0 t\right)\\ 0\end{bmatrix}$$

$$\Delta C_{\dot{\alpha}_0} = \left.\frac{\partial\vec{a}_{LT}}{\partial\dot{\alpha}_0}\right|_{r,\dot{r}=const} = \Delta C_{\alpha_0} t$$

$$\Delta C_{\delta_0} = \left.\frac{\partial\vec{a}_{LT}}{\partial\delta_0}\right|_{r,\dot{r}=const} = \frac{(1+\gamma)}{c^2 r^3} GJ\left[\frac{3}{r^2}\left(\underline{\underline{\times\vec{v}}}\cdot\vec{r}\right)\vec{r}^T-\underline{\underline{\times\vec{v}}}\right]\begin{bmatrix}-\cos\left(\alpha_0+\dot{\alpha}_0 t\right)\sin\left(\delta_0+\dot{\delta}_0 t\right)\\ -\sin\left(\alpha_0+\dot{\alpha}_0 t\right)\sin\left(\delta_0+\dot{\delta}_0 t\right)\\ \cos\left(\delta_0+\dot{\delta}_0 t\right)\end{bmatrix}$$

$$\Delta C_{\dot{\delta}_0} = \left.\frac{\partial\vec{a}_{LT}}{\partial\dot{\delta}_0}\right|_{r,\dot{r}=const} = \Delta C_{\delta_0} t$$

$$\Delta C_{W_0} = \left.\frac{\partial \vec{a}_{LT}}{\partial W_0}\right|_{r,\dot{r}=const} = 0 \qquad ; \qquad \Delta C_{\dot{W}_0} = \left.\frac{\partial \vec{a}_{LT}}{\partial \dot{W}_0}\right|_{r,\dot{r}=const} = \Delta C_J \frac{\partial J}{\partial \dot{W}_0}$$

If the angular momentum is supposed to be the result of differential rotation phenomena, it can be considered independent from the rotation rate of Jupiter System III and the last derivative is null.

Once obtained the integrated solution, the state transition matrix $\Phi_{LT}(t,t_0)$ is straightforwardly obtained.

5.2.1.2 *The particular solution*

The particular solution is solution of the linearized trajectory for initial conditions $x_0 = 0$

$$\left.\begin{array}{l} x(t) = \Phi_{LT}(t,t_0)x_0 + x_P \\ x_0 = 0 \end{array}\right\} x(t) = x_P$$

It is computed by directly integrating the equation

$$\dot{x} = Mx + a_{LT}\left(X^*,t\right)$$

with initial conditions $x_0 = 0$.

5.2.2 Observables correction

Once the trajectory correction has been computed, it is necessary to compute the correction to the observables.

The process of the observables linearization is the same as in Section 3.4.1.

$$Y_i - Y_i^* = y_i = \tilde{H}_i x_i + \varepsilon_i .$$

The x_i solution can be rewritten in terms of the trajectory correction computed in the previous section.

$$y_i = \tilde{H}_i\left(\Phi_{LT}\left(t_i,t_0\right)x_0 + x_P\right) + \varepsilon_i = \tilde{H}_i\Phi_{LT}\left(t_i,t_0\right)x_0 + \tilde{H}_i x_P + \varepsilon_i \,.$$

It is not possible to access directly the $\tilde{H}_i$ matrix. The available ODP product is the matrix $H_i = \tilde{H}_i\Phi$ (cf. Section 3.4.1), along with the state transition matrix Φ . Consequently $\tilde{H}_i = H_i\Phi^{-1}$. In doing this operation one must remember that the matrix $\tilde{H}_i$ computed in this way is one element shorter in the parameters direction since it does not account for the partials with respect to the angular momentum. The observables are not explicitly dependent on the value of J, hence

$$\tilde{H}_i \Rightarrow \begin{bmatrix} \tilde{H}_i & \vdots & 0 \end{bmatrix}$$

The term $\tilde{H}_i x_P$ becomes a known quantity that can be summed to the computed observables to account for the Lense-Thirring effect

$$Y_i - \left(Y_i^* + \tilde{H}_i x_P\right) = \tilde{H}_i\Phi_{LT}x_0 + \varepsilon_i \qquad ; \qquad \tilde{Y}_i^* = Y_i^* + \tilde{H}_i x_P$$

$$Y_i - \tilde{Y}_i^* = \tilde{y}_i = H_{LT,i}x_0 + \varepsilon_i \qquad ; \qquad H_{LT,i} = \tilde{H}_i\Phi_{LT} = H_i\Phi^{-1}\Phi_{LT}$$

5.2.3 Least squares filter

Now the trajectory, the computed observables and the observables partial derivatives are available. The least squares filtering can be carried out as in Section 3.4.1.

5.3 Jupiter angular momentum estimation

The Lense-Thirring acceleration model is included in the dynamical model to be used for the observed data simulation. The value adopted in the simulation is $4.5041 \cdot 10^{32}$ kg km^{-2} s^{-1} (cf. Table 5.1). The net signal due to the additional model is reported in Figure 5.3.

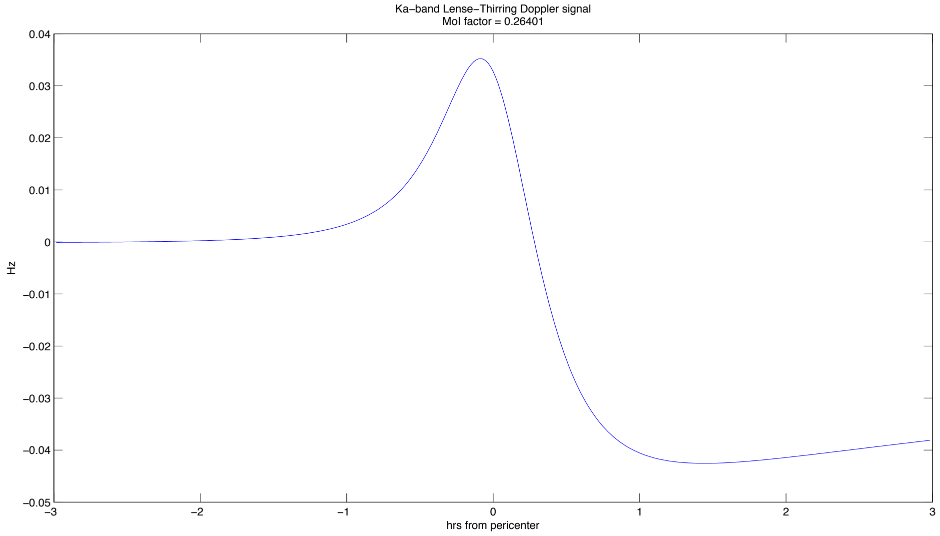

Figure 5.3 Ka-band Doppler signal due to the Lense-Thirring model (orbit no. 4). The peak-to-peak value is compliant with the velocity difference shown in Figure 5.1.

The estimation process setup is the same presented in Section 0. The angular momentum of Jupiter is inserted in the estimated global parameters set with a value of $6.8242 \cdot 10^{32}$ kg km^{-2} s^{-1} and an a priori uncertainty of $8.5302 \cdot 10^{32}$ kg km^{-2} s^{-1}, corresponding to a moment of inertia factor of 0.5. The estimation results are reported in Table 5.2 and Figure 5.4.

Formal uncertainty (1-sigma) kg km^{-2} s^{-1}	Estimation Error kg km^{-2} s^{-1}	Estimated value kg km^{-2} s^{-1}
$1.0591 \cdot 10^{31}$	$3.0881 \cdot 10^{31}$	$4.8129 \cdot 10^{32}$

Table 5.2 Jupiter angular momentum estimation results.

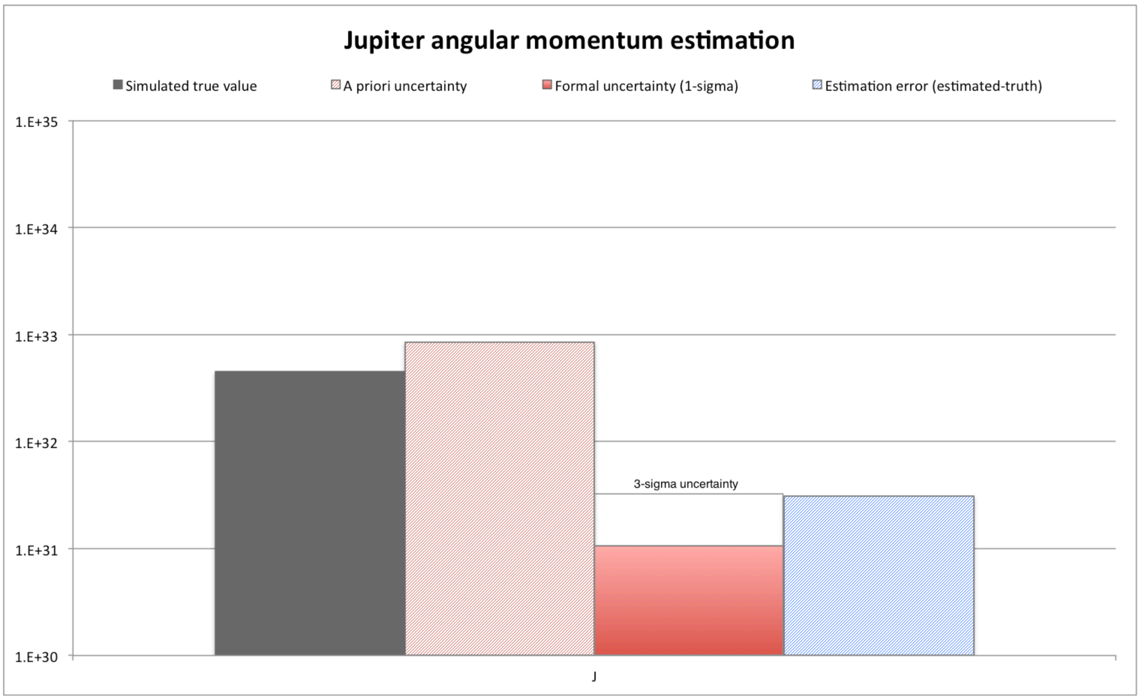

Figure 5.4 Jupiter angular momentum estimation results.

The estimate of the angular momentum is compliant with the formal uncertainty to a 3-sigma level, corresponding to a relative uncertainty of about 7% of the simulated true value. The large estimation error is probably due to the linearized process used for the trajectory integration and observables computation.

Figure 5.5 shows the correlation index between the angular momentum and the other global parameters.

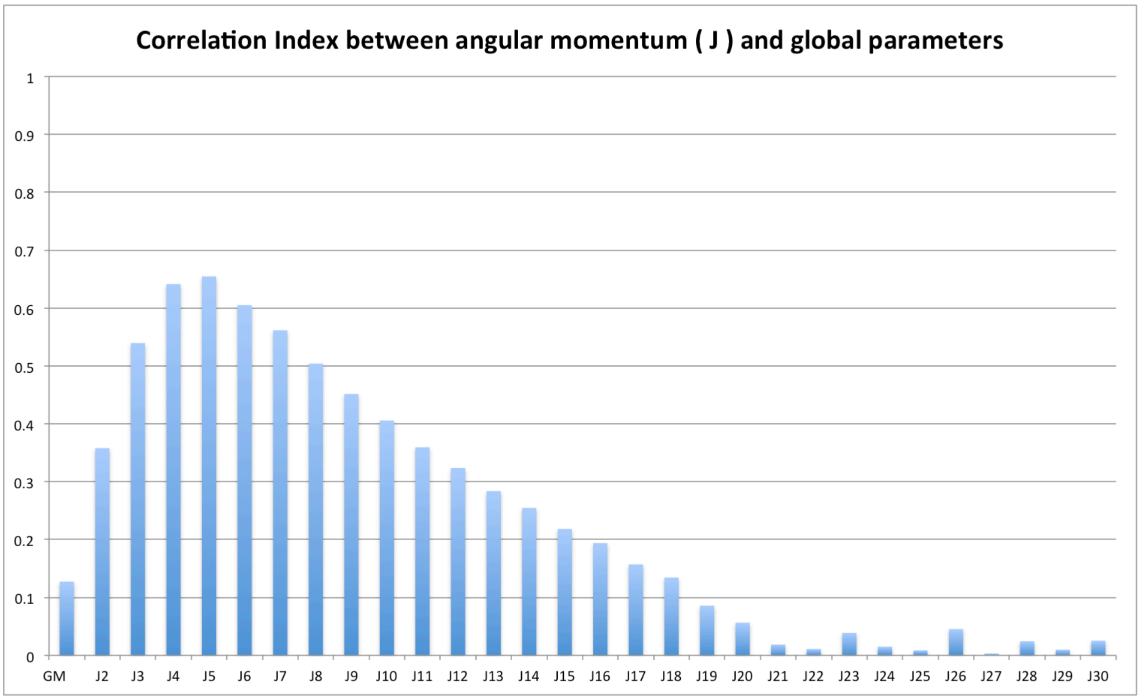

Figure 5.5 Correlation Index between the Jupiter angular momentum and the other gobal parameters (GM and zonal gravity field).

Only the correlation with the GM and the zonal coefficients are relevant (up to 0.65 at J_5). Correlations with tesseral coefficients and Love numbers are negligible.

6 Conclusions

The Juno gravity experiment is an hard challenge from the point of view of the data analysis. The Ka-band Translator allows collecting very high quality Doppler data (accurate to 5 μm/s at 1000 seconds integration time) but unfortunately the orbit geometry is unfavorable to the fulfillment of the experiment scientific requirements.

The gravity field perturbs the spacecraft velocity along-track, which is a direction that lies on the orbit plane. The angle between the line-of-sight and the normal to the orbit plane is very small thus significantly reducing the observable Doppler signal.

Moreover the highly elliptical polar orbit does not guarantee a uniform coverage of the planet surface. The spacecraft is sensitive to the gravity field perturbations only when actually close to pericenter. Since the orbit pericenter rotates northward by one degree per orbit, the surface coverage is substantially limited to 25 points. If one makes the assumption that the gravity field is mainly zonal, the 25 points define a latitude belt, corresponding to the 21.6% of the planet surface.

When the spherical harmonics are used to describe a function on a limited region of the sphere, they lose the property of being mutually orthonormal. The description of the gravity field in the belt is therefore not unique in terms of spherical harmonics functions. The level-2 requirements, expressed in terms of accuracy on the spherical harmonics coefficients, as presented in the Introduction are no more adequate to pose constraints to the performance of the experiment. A reformulation must be considered in terms of uncertainty on the detection of gravity anomalies, at least for the requirements regarding the detection of the zonal winds signal, since gravity anomalies are independent from the basis of functions chosen to represent them.

The numerical simulations have been carried out under the assumption of mainly zonal gravity field. The uncertainty on the reconstructed gravity field in the sampled region is about 0.1 mGal increasing by many orders of magnitude towards the poles (nearly 30 mGal at the south pole). These results take into account the possible presence of a detectable low degree tesseral gravity field (up to degree 5). If the detectable signal from the tesseral gravity required a greater number of coefficients the uncertainty on the global gravity field would be larger.

Along with the static gravity field, the tidal deformations of Jupiter have been estimated. Tides dynamically perturb the gravity field of the planet and consequently the spacecraft trajectory. The expected velocity variations are mainly out-of-plane, thus projecting a large signal onto the line-of-sight. The high sensitivity to the tidal perturbations reflects into a very good determination of the degree 2 and 3 Love numbers. k_2 is determined with an accuracy of $2.6 \cdot 10^{-3}$ while k_3 uncertainty is $4.5 \cdot 10^{-3}$.

The Juno gravity experiment will compensate the unfavorable orbit geometry with an excellent quality of the Doppler data. For sure, the attainable accuracies are sufficient to constrain the mass of the Jupiter core. It is a geophysicists' job to return an affordable estimate of the gravity signal expected from the atmospheric dynamics only (the signal that can uniquely be attributable to this gravity source without contamination with the gravity field of the hydrostatic ellipsoid). The question is at the moment an open issue.

This work has shown the possibility to enhance the scientific return of the mission by estimating the mean angular momentum of the planet by detecting the Doppler signal of the Lense-Thirring precession of the spacecraft trajectory. Usually space mission put General Relativity to test in order to find confirmations or deviations from Einstein's formulation. The Juno mission has not the possibility to set up a relativity experiment for the frame dragging effect because the angular momentum of Jupiter is unknown. On the other hand, LARES will measure the relativistic effect with a relative uncertainty of 1%. If no deviations of General Relativity will be individuated, it is possible to make the assumption that the Einstein's formulation is correct for the Juno gravity experiment accuracy level. At that point, the signal would be deterministic and could be used to estimate the angular momentum. For the first time General Relativity is used to estimate a geophysical parameter.

The JPL's Orbit Determination Program does not contain the model of the Lense-Thirring acceleration for planets other than the Earth. Much of the work consisted in identifying a consistent mathematical formulation for small corrections to the orbit determination process and the consequent software coding able to interact with the ODP products.

The test results show an accuracy of $1 \cdot 10^{31}$ kg km^{-2} s^{-1} in the determination of the angular momentum, which is about the 2% of the expected value. The estimation error is compliant with the formal uncertainty to a 3-sigma level (7% relative accuracy).

This work can be further expanded by studying the effects of mismodeling in the dynamical model used in the estimation process. Non-gravitational accelerations are the main candidates for dynamical model inaccuracies.

The KaTS results determinant for the accomplishment of the scientific results proposed for the Juno mission gravity science experiment. Without the crucial contribution of the Italian instrument none of the objectives would be achieved.

Appendix A : Gravity Mapping

A.1 Gravitational potential and acceleration

The gravitational potential is expressed in terms of spherical harmonics functions. Its gradient is called gravitational acceleration.

$$U = -\frac{GM}{R}\left(\sum_{l=0}^{N}\sum_{m=0}^{l}\left(\frac{R}{r}\right)^{l+1} P_{lm}(cos\theta)[C_{lm}cos(m\varphi) + S_{lm}sin(m\varphi)]\right)$$

$$g = -\nabla U = \left[-\frac{\partial U}{\partial r} \quad -\frac{1}{r}\frac{\partial U}{\partial \theta} \quad -\frac{1}{rsin\theta}\frac{\partial U}{\partial \varphi}\right]$$

$$g(r,\theta,\varphi) = \begin{cases} -\dfrac{\partial U}{\partial r} = -\dfrac{GM}{R^2}\left(\displaystyle\sum_{l=0}^{N}\sum_{m=0}^{l}(l+1)\left(\frac{R}{r}\right)^{l+2} P_{lm}(cos\theta)[C_{lm}cos(m\varphi) + S_{lm}sin(m\varphi)]\right) \\ -\dfrac{1}{r}\dfrac{\partial U}{\partial \theta} = \dfrac{GM}{R^2}\left(\displaystyle\sum_{l=0}^{N}\sum_{m=0}^{l}\left(\frac{R}{r}\right)^{l+2} \frac{\partial P_{lm}(cos\theta)}{\partial \theta}[C_{lm}cos(m\varphi) + S_{lm}sin(m\varphi)]\right) \\ -\dfrac{1}{rsin\theta}\dfrac{\partial U}{\partial \varphi} = \dfrac{GM}{R^2}\left(\displaystyle\sum_{l=0}^{N}\sum_{m=0}^{l} m\left(\frac{R}{r}\right)^{l+2} \frac{P_{lm}(cos\theta)}{sin\theta}[S_{lm}cos(m\varphi) - C_{lm}sin(m\varphi)]\right) \end{cases}$$

Let us change notation in favor of a vector formulation in order to ease the computations of the gravity related quantities.

$$0 \le m \le l \;\rightarrow\; -l \le m \le l \;: \begin{array}{cccc} C_{lm} \rightarrow J_{l,m} & P_{lm}cos(m\varphi) \rightarrow Y_{l,m} \\ S_{lm} \rightarrow J_{l,-m} & P_{lm}sin(m\varphi) \rightarrow Y_{l,-m} \end{array}$$

$$J = \begin{bmatrix} 1 \\ 0 \\ 0 \\ 0 \\ J_{2,0} \\ J_{2,1} \\ J_{2,-1} \\ J_{2,2} \\ J_{2,-2} \\ J_{3,0} \\ \vdots \\ J_{N,-N} \end{bmatrix} = \begin{bmatrix} 1 \\ 0 \\ 0 \\ 0 \\ C_{2,0} \\ C_{2,1} \\ S_{2,1} \\ C_{2,2} \\ S_{2,2} \\ C_{3,0} \\ \vdots \\ S_{N,N} \end{bmatrix} \qquad Y = \begin{bmatrix} Y_{0,0} \\ Y_{1,0} \\ Y_{1,1} \\ Y_{1,-1} \\ Y_{2,0} \\ Y_{2,1} \\ Y_{2,-1} \\ Y_{2,2} \\ Y_{2,-2} \\ Y_{3,0} \\ \vdots \\ Y_{N,-N} \end{bmatrix} = \begin{bmatrix} P_{0,0} \\ P_{1,0} \\ P_{1,1}\cos(\varphi) \\ P_{1,1}\sin(\varphi) \\ P_{2,0} \\ P_{2,1}cos(\varphi) \\ P_{2,1}sin(\varphi) \\ P_{2,2}cos(2\varphi) \\ P_{2,2}sin(2\varphi) \\ P_{3,0} \\ \vdots \\ P_{N,N}sin(N\varphi) \end{bmatrix}$$

$$D_\theta Y = \begin{bmatrix} \partial Y_{0,0}/\partial\theta \\ \partial Y_{1,0}/\partial\theta \\ \partial Y_{1,1}/\partial\theta \\ \partial Y_{1,-1}/\partial\theta \\ \partial Y_{2,0}/\partial\theta \\ \partial Y_{2,1}/\partial\theta \\ \partial Y_{2,-1}/\partial\theta \\ \partial Y_{2,2}/\partial\theta \\ \partial Y_{2,-2}/\partial\theta \\ \partial Y_{3,0}/\partial\theta \\ \vdots \\ \partial Y_{N,-N}/\partial\theta \end{bmatrix} \qquad D_\varphi Y = \begin{bmatrix} \partial Y_{0,0}/\partial\varphi \\ \partial Y_{1,0}/\partial\varphi \\ \partial Y_{1,1}/\partial\varphi \\ \partial Y_{1,-1}/\partial\varphi \\ \partial Y_{2,0}/\partial\varphi \\ \partial Y_{2,1}/\partial\varphi \\ \partial Y_{2,-1}/\partial\varphi \\ \partial Y_{2,2}/\partial\varphi \\ \partial Y_{2,-2}/\partial\varphi \\ \partial Y_{3,0}/\partial\varphi \\ \vdots \\ \partial Y_{N,-N}/\partial\varphi \end{bmatrix} = \begin{bmatrix} 0 \\ 0 \\ -Y_{1,-1} \\ Y_{1,1} \\ 0 \\ -Y_{2,-1} \\ Y_{2,1} \\ -2Y_{2,-2} \\ 2Y_{2,2} \\ 0 \\ \vdots \\ NY_{N,N} \end{bmatrix}$$

$$L = \begin{bmatrix} I(1) & & \\ & \ddots & \\ & & (N+1)I(2N+1) \end{bmatrix} \quad C = \begin{bmatrix} \left(\frac{R}{r}\right)^2 I(1) & & \\ & \ddots & \\ & & \left(\frac{R}{r}\right)^{N+2} I(2N+1) \end{bmatrix}$$

the gravitational acceleration is rewritten as:

$$g(r,\theta,\varphi) = \begin{cases} g_r = -\frac{GM}{R^2}\left(\left(\frac{R}{r}\right)^2 + J^T LCY\right) \\ g_\theta = \frac{GM}{R^2}\left(J^T CD_\theta Y\right) \\ g_\varphi = \frac{GM}{R^2 sin\theta}\left(J^T CD_\varphi Y\right) \end{cases}$$

A.2 Normal and anomalous gravitational potential

The normal gravity potential is the potential of the reference figure

$$U_N = -\frac{GM}{R}\left(\sum_{l=0}^{N}\sum_{m=0}^{l}\left(\frac{R}{r}\right)^{l+1} P_{lm}(cos\theta)\left[C_{lm}^N cos(m\varphi) + S_{lm}^N sin(m\varphi)\right]\right)$$

In the case of a triaxial ellipsoid only the coefficients C_{lm}^N and S_{lm}^N with even l and m are not null. A good approximation consists in considering only the coefficients $C_{2,0}^N$ and $C_{2,2}^N$.

The anomalous potential T is defined as the difference between the measured gravitational potential U and the normal potential U_N.

$$T = U - U_N$$

$$T = -\frac{GM}{R}\left(\sum_{l=0}^{N}\sum_{m=0}^{l}\left(\frac{R}{r}\right)^{l+1} P_{lm}(cos\theta)\left[\left(C_{lm} - C_{lm}^N\right)cos(m\varphi) + \left(S_{lm} - S_{lm}^N\right)sin(m\varphi)\right]\right)$$

$$T = -\frac{GM}{R}\left(\sum_{l=0}^{N}\sum_{m=0}^{l}\left(\frac{R}{r}\right)^{l+1} P_{lm}(cos\theta)\left[C_{lm}^T cos(m\varphi) + S_{lm}^T sin(m\varphi)\right]\right)$$

The harmonic coefficients result

$$C_{lm}^{T} = \left(C_{lm} - C_{lm}^{N}\right) \qquad S_{lm}^{T} = \left(S_{lm} - S_{lm}^{N}\right).$$

Let us define $J_N = \begin{bmatrix} 1 \\ 0 \\ 0 \\ 0 \\ C_{2,0}^{N} \\ C_{2,1}^{N} \\ S_{2,1}^{N} \\ C_{2,2}^{N} \\ S_{2,2}^{N} \\ C_{3,0}^{N} \\ \vdots \\ S_{N,N}^{N} \end{bmatrix}$ and $J_T = \begin{bmatrix} 0 \\ 0 \\ 0 \\ 0 \\ C_{2,0}^{T} \\ C_{2,1}^{T} \\ S_{2,1}^{T} \\ C_{2,2}^{T} \\ S_{2,2}^{T} \\ C_{3,0}^{T} \\ \vdots \\ S_{N,N}^{T} \end{bmatrix}$.

A.3 Shape

A.3.1 Reference figure (Ellipsoid)

The starting point of the geoid definition is the generation of the reference figure. This surface is particularly important because it defines the general shape of the planetary figure. For a synchronous satellite the ellipsoid is defined as the equipotential surface under the action of three different fields:

- its own gravity field
- the rotational (centrifugal) field
- the tidal field from the central planet

The last two potentials can be expressed in terms of degree 2 spherical harmonics, while the gravitational potential of the reference figure is by definition the normal potential:

$$U_N = -\frac{GM}{R}\left(\sum_{l=0}^{N}\sum_{m=0}^{l}\left(\frac{R}{r}\right)^{l+1}\left[C_{lm}^{N}Y_{l,m} + S_{lm}^{N}Y_{l,-m}\right]\right)$$

$$U_r = -\frac{1}{2}\omega^2 r^2 \sin^2\theta = -\frac{1}{3}\omega^2 r^2\left[1 - Y_{2,0}\right]$$

$$U_t = \frac{1}{2}\frac{GM_C}{a^3}r^2\left[Y_{2,0} - \frac{1}{2}Y_{2,2}\right]$$

where R is the reference radius, a the semi-major axis of the orbit and M_C the mass of the perturbing body. The general expression of the potential must be constant (level figure):

$$U = U_N + U_r + U_t = U_0$$

Regrouping the terms having the same angular dependence:

$$U = -\frac{GM}{r} - \frac{1}{3}\omega^2 r^2 + \left[-\frac{GM}{r}\left(\frac{R}{r}\right)^2 C_{20}^{N} + \frac{1}{3}\omega^2 r^2 + \frac{1}{2}\frac{GM_C}{a^3}r^2\right]Y_{2,0} +$$

$$+\left[-\frac{GM}{r}\left(\frac{R}{r}\right)^2 C_{22}^{N} + \frac{1}{4}\frac{GM_C}{a^3}r^2\right]Y_{2,2} +$$

$$-\frac{GM}{r}\left(\left(\frac{R}{r}\right)^2\left(C_{21}^{N}Y_{2,1} + S_{21}^{N}Y_{2,-1} + S_{22}^{N}Y_{2,-2}\right) + \sum_{l\geq 3}^{N}\sum_{m=0}^{l}\left(\frac{R}{r}\right)^{l}\left[C_{lm}^{N}Y_{l,m} + S_{lm}^{N}Y_{l,-m}\right]\right)$$

and introducing the rotational (q_r) and tidal (q_t) parameters:

$$q_r = \frac{\omega^2 R^3}{GM} \qquad q_t = -3\frac{M_C}{M}\left(\frac{R}{a}\right)^3$$

$$U =$$

$$= -\frac{GM}{r}\left\{1 + \frac{1}{3}\left(\frac{r}{R}\right)^3 q_r + \left[\left(\frac{R}{r}\right)^2 C_{20}^N - \frac{1}{3}\left(\frac{r}{R}\right)^3 q_r + \frac{1}{6}\left(\frac{r}{R}\right)^3 q_t\right] Y_{2,0}\right.$$

$$+ \left[\left(\frac{R}{r}\right)^2 C_{22}^N - \frac{1}{12}\left(\frac{r}{R}\right)^3 q_t\right] Y_{2,2} + \left(\frac{R}{r}\right)^2 \left(C_{21}^N Y_{2,1} + S_{21}^N Y_{2,-1} + S_{22}^N Y_{2,-2}\right)$$

$$\left. + \sum_{l\geq 3}^{N} \sum_{m=0}^{l} \left(\frac{R}{r}\right)^l \left[C_{lm}^N Y_{l,m} + S_{lm}^N Y_{l,-m}\right]\right\} = U_0 = -\frac{GM}{R}$$

The radius r must describe an equipotential surface of the potential U.

Approximating the ratio r/R and R/r with 1, and solving for r :

$$r_{ref} =$$

$$= R\left\{1 + \frac{1}{3} q_r + \left[C_{20}^N - \frac{1}{3} q_r + \frac{1}{6} q_t\right] Y_{2,0} + \left[C_{22}^N - \frac{1}{12} q_t\right] Y_{2,2}\right.$$

$$\left. + \left(C_{21}^N Y_{2,1} + S_{21}^N Y_{2,-1} + S_{22}^N Y_{2,-2}\right) + \sum_{l\geq 3}^{N} \sum_{m=0}^{l} \left[C_{lm}^N Y_{l,m} + S_{lm}^N Y_{l,-m}\right]\right\}$$

A.3.2 Particular case 1: Spheroid (C_{20}^N only)

$$J_N = \begin{bmatrix} 1 \\ 0 \\ 0 \\ 0 \\ C_{2,0}^N \\ 0 \\ 0 \\ 0 \\ 0 \\ 0 \\ \vdots \\ 0 \end{bmatrix} \qquad r_{sph} = R\left\{1 + \frac{1}{3} q_r + \left[C_{20}^N - \frac{1}{3} q_r + \frac{1}{6} q_t\right] Y_{2,0} - \left[\frac{1}{12} q_t\right] Y_{2,2}\right\}$$

A.3.3 Particular case 2: Triaxial Ellipsoid (C_{20}^N and C_{22}^N only)

$$J_N = \begin{bmatrix} 1 \\ 0 \\ 0 \\ 0 \\ C_{2,0}^N \\ 0 \\ 0 \\ C_{2,2}^N \\ 0 \\ 0 \\ \vdots \\ 0 \end{bmatrix} \qquad r_{ell} = R\left\{1 + \frac{1}{3}q_r + \left[C_{20}^N - \frac{1}{3}q_r + \frac{1}{6}q_t\right]Y_{2,0} + \left[C_{22}^N - \frac{1}{12}q_t\right]Y_{2,2}\right\}$$

A.4 The geoid

The geoid is defined as an equipotential surface of a planetary body. It could be described as the surface of an ideal ocean, with no waves, currents or atmospheric influence, hence at constant pressure. Deviations of a planetary surface from the geoid provide information on the interior structure. The geoid also defines the zero of the topographic altitude.

The equations for the geoid computation are the same shown for the reference figure where the normal potential is substituted with the actual body gravitational potential.

$$U = U + U_r + U_t =$$

$$= -\frac{GM}{r}\left\{1 + \frac{1}{3}\left(\frac{r}{R}\right)^3 q_r + \left[\left(\frac{R}{r}\right)^2 C_{20} - \frac{1}{3}\left(\frac{r}{R}\right)^3 q_r + \frac{1}{6}\left(\frac{r}{R}\right)^3 q_t\right]Y_{2,0}\right.$$

$$+\left[\left(\frac{R}{r}\right)^2 C_{22} - \frac{1}{12}\left(\frac{r}{R}\right)^3 q_t\right]Y_{2,2} + \left(\frac{R}{r}\right)^2 \left(C_{21}Y_{2,1} + S_{21}Y_{2,-1} + S_{22}Y_{2,-2}\right)$$

$$\left.+\sum_{l\geq 3}^{N}\sum_{m=0}^{l}\left(\frac{R}{r}\right)^l \left[C_{lm}Y_{l,m} + S_{lm}Y_{l,-m}\right]\right\} = U_0 = -\frac{GM}{R}$$

$$r_{geo} =$$

$$= R\left\{1 + \frac{1}{3}q_r + \left[C_{20} - \frac{1}{3}q_r + \frac{1}{6}q_t\right]Y_{2,0} + \left[C_{22} - \frac{1}{12}q_t\right]Y_{2,2}\right.$$

$$\left. + \left(C_{21}Y_{2,1} + S_{21}Y_{2,-1} + S_{22}Y_{2,-2}\right) + \sum_{l\geq 3}^{N}\sum_{m=0}^{l}\left[C_{lm}Y_{l,m} + S_{lm}Y_{l,-m}\right]\right\}$$

The **geoid heights** are defined as the differences between the geoid and the reference figure

$$\varDelta r_{gh} = r_{geo} - r_{ref}$$

$$= R\left\{[C_{20} - C_{20}^{N}]Y_{2,0} + [C_{22} - C_{22}^{N}]Y_{2,2}\right.$$

$$+ \left[(C_{21} - C_{21}^{N})Y_{2,1} + (S_{21} - S_{21}^{N})Y_{2,-1} + (S_{22} - S_{22}^{N})Y_{2,-2}\right]$$

$$\left. + \sum_{l\geq 3}^{N}\sum_{m=0}^{l}\left[\left(C_{lm} - C_{lm}^{N}\right)Y_{l,m} + \left(S_{lm} - S_{lm}^{N}\right)Y_{l,-m}\right]\right\} =$$

$$= R\left\{\sum_{l\geq 2}^{N}\sum_{m=0}^{l}\left[\left(C_{lm} - C_{lm}^{N}\right)Y_{l,m} + \left(S_{lm} - S_{lm}^{N}\right)Y_{l,-m}\right]\right\} = R\left\{\sum_{l\geq 2}^{N}\sum_{m=0}^{l}\left[C_{lm}^{T}Y_{l,m} + S_{lm}^{T}Y_{l,-m}\right]\right\}$$

$$= \frac{T - U_0}{g_0}$$

In vector notation:

$$\varDelta r_{gh} = R\{J_T^T Y\}$$

A.5 Gravity

A.5.1 The spherical approximation

When computing gravity and geoid deviations with respect to a reference figure (e.g. ellipsoid) one must consider that the reference figure deviates from a sphere only by quantities of the order of the flattening. Therefore if the reference ellipsoid is treated as a sphere when dealing with the anomalous potential, the relative error in the equations will consequently be of the same order as the flattening.

This approximation is used only in the computation of small quantities and does not imply that the reference figure is a "sphere" in a geometrical sense. The reference figure is an ellipsoid but the ellipsoidal equations are expanded in power series of the flattening, where all the terms containing the powers of the flattening are neglected. In particular this approximation is adopted for the computation of the anomalous potential, geoid heights, gravity anomalies and disturbances.

(Heiskanen et al., 1967, pp. 96-97)

A.5.2 Gravity disturbances

Adopting the spherical approximation, the gravity disturbance is defined as:

$$\delta g(r,\theta,\varphi) = -\frac{\partial T}{\partial r}$$

$$= -\frac{GM}{R^2}\left(\sum_{l\geq 2}^{N}\sum_{m=0}^{l}(l+1)\left(\frac{R}{r}\right)^{l+2} P_{lm}(cos\theta)\left[C_{lm}^{T}cos(m\varphi) + S_{lm}^{T}sin(m\varphi)\right]\right)$$

on the geoid r=R

$$\delta g(R,\theta,\varphi) = -\frac{GM}{R^2}\left(\sum_{l\geq 2}^{N}\sum_{m=0}^{l}(l+1)P_{lm}(cos\theta)\left[C_{lm}^{T}cos(m\varphi)+S_{lm}^{T}sin(m\varphi)\right]\right)$$

$$= -\frac{GM}{R^2}(J_T^T LY)$$

A.5.3 Gravity anomalies

Analogously, the gravity anomalies are defined as:

$$\Delta g(r,\theta,\varphi) = -\frac{\partial T}{\partial r}-\frac{2}{r}T =$$

$$= -\frac{GM}{R^2}\left(\sum_{l\geq 2}^{N}\sum_{m=0}^{l}(l-1)\left(\frac{R}{r}\right)^{l+2}P_{lm}(cos\theta)\left[C_{lm}^{T}cos(m\varphi)+S_{lm}^{T}sin(m\varphi)\right]\right)$$

on the geoid r=R

$$\Delta g(R,\theta,\varphi) = -\frac{GM}{R^2}\left(\sum_{l\geq 2}^{N}\sum_{m=0}^{l}(l-1)P_{lm}(cos\theta)\left[C_{lm}^{T}cos(m\varphi)+S_{lm}^{T}sin(m\varphi)\right]\right) =$$

$$= -\frac{GM}{R^2}(J_T^T(L-2I)Y)$$

A.6 Computation of the uncertainties

Define the vector of the estimated gravity parameters x as:

$$x = \begin{bmatrix} x_1 \\ x_2 \\ \vdots \\ x_p \end{bmatrix} = \begin{bmatrix} GM \\ J_{2,0} \\ \vdots \\ J_{N,-N} \end{bmatrix}$$

the uncertainty in the function $y = f(x)$ is given by:

$$\sigma_y^2 = \sum_{i=1}^{p}\sum_{j=1}^{p}\left(\frac{\partial y}{\partial x_i}\right)\left(\frac{\partial y}{\partial x_j}\right)COV(x_i,x_j) = \left(\frac{\partial y}{\partial x}\right)COV\left(\frac{\partial y}{\partial x}\right)^T$$

We need to apply this procedure to evaluate the uncertainty associated to the geoid heights, surface gravity acceleration, gravity disturbances and anomalies.

A.6.1 Geoid Heights

$$\Delta r_{gh} = R\{J_T^T Y\}$$

$$\sigma_{\Delta r}^2 = \left(\frac{\partial \Delta r}{\partial x}\right) COV \left(\frac{\partial \Delta r}{\partial x}\right)^T$$

$$\frac{\partial \Delta r}{\partial x} = \begin{bmatrix} \frac{\partial \Delta r}{\partial GM} & \frac{\partial \Delta r}{\partial J} \end{bmatrix} = \begin{bmatrix} 0 & \frac{\partial \Delta r}{\partial J_T}\frac{\partial J_T}{\partial J} \end{bmatrix} = [0 \quad RY^T] \qquad \frac{\partial J_T}{\partial J} = \frac{\partial (J - J_N)}{\partial J} = I$$

A.6.2 Surface gravity

$$g(R,\theta,\varphi) = \begin{cases} g_r = -\frac{GM}{R^2}(1 + J^T L Y) \\ g_\theta = \frac{GM}{R^2}(J^T D_\theta Y) \\ g_\varphi = \frac{GM}{R^2 sin\theta}\left(J^T D_\varphi Y\right) \end{cases}$$

$$\begin{cases} \sigma_{g_r}^2 = \left(\frac{\partial g_r}{\partial x}\right) COV \left(\frac{\partial g_r}{\partial x}\right)^T \\ \sigma_{g_\theta}^2 = \left(\frac{\partial g_\theta}{\partial x}\right) COV \left(\frac{\partial g_\theta}{\partial x}\right)^T \\ \sigma_{g_\varphi}^2 = \left(\frac{\partial g_\varphi}{\partial x}\right) COV \left(\frac{\partial g_\varphi}{\partial x}\right)^T \end{cases}$$

$$\frac{\partial g_r}{\partial x} = \begin{bmatrix} \frac{\partial g_r}{\partial GM} & \frac{\partial g_r}{\partial J} \end{bmatrix} = \begin{bmatrix} \frac{g_r}{GM} & \frac{\partial g_r}{\partial J} \end{bmatrix} = \begin{bmatrix} -\frac{1}{R^2}(1 + J^T L Y) & -\frac{GM}{R^2} Y^T L \end{bmatrix}$$
$$\frac{\partial g_\theta}{\partial x} = \begin{bmatrix} \frac{\partial g_\theta}{\partial GM} & \frac{\partial g_\theta}{\partial J} \end{bmatrix} = \begin{bmatrix} \frac{g_\theta}{GM} & \frac{\partial g_\theta}{\partial J} \end{bmatrix} = \begin{bmatrix} \frac{1}{R^2}(J^T D_\theta Y) & \frac{GM}{R^2} D_\theta Y^T \end{bmatrix}$$
$$\frac{\partial g_\varphi}{\partial x} = \begin{bmatrix} \frac{\partial g_\varphi}{\partial GM} & \frac{\partial g_\varphi}{\partial J} \end{bmatrix} = \begin{bmatrix} \frac{g_\varphi}{GM} & \frac{\partial g_\varphi}{\partial J} \end{bmatrix} = \begin{bmatrix} \frac{1}{R^2 sin\theta}\left(J^T D_\varphi Y\right) & \frac{GM}{R^2 sin\theta} D_\varphi Y^T \end{bmatrix}$$

The total surface gravity module is $|g| = \sqrt{g_r^2 + g_\theta^2 + g_\varphi^2}$

$$\sigma_{|g|}^2 = \frac{1}{|g|^2}\left(g_r^2 \sigma_{g_r}^2 + g_\theta^2 \sigma_{g_\theta}^2 + g_\varphi^2 \sigma_{g_\varphi}^2\right)$$

A.6.3 Gravity disturbances

$$\delta g(R,\theta,\varphi) = -\frac{GM}{R^2}(J_T^T LY)$$

$$\sigma_{\delta g}^2 = \left(\frac{\partial \delta g}{\partial x}\right) COV \left(\frac{\partial \delta g}{\partial x}\right)^T$$

$$\frac{\partial \delta g}{\partial x} = \begin{bmatrix} \frac{\partial \delta g}{\partial GM} & \frac{\partial \delta g}{\partial J} \end{bmatrix} = \begin{bmatrix} \frac{\delta g}{GM} & \frac{\partial \delta g}{\partial J} \end{bmatrix} = \begin{bmatrix} -\frac{1}{R^2}(J_T^T LY) & -\frac{GM}{R^2} Y^T L \end{bmatrix}$$

A.6.4 Gravity anomalies

$$\Delta g(R,\theta,\varphi) = -\frac{GM}{R^2}(J_T^T (L-2I)Y)$$

$$\sigma_{\Delta g}^2 = \left(\frac{\partial \Delta g}{\partial x}\right) COV \left(\frac{\partial \Delta g}{\partial x}\right)^T$$

$$\frac{\partial \Delta g}{\partial x} = \begin{bmatrix} \frac{\partial \Delta g}{\partial GM} & \frac{\partial \Delta g}{\partial J} \end{bmatrix} = \begin{bmatrix} \frac{\Delta g}{GM} & \frac{\partial \Delta g}{\partial J} \end{bmatrix} = \begin{bmatrix} -\frac{1}{R^2}(J_T^T (L-2I)Y) & -\frac{GM}{R^2} Y^T (L-2I) \end{bmatrix}$$

A.7 Example

Suppose we have a set of estimated parameters $J = \begin{bmatrix} C_{20} \\ C_{22} \\ C_{30} \end{bmatrix}$ with associated covariance

$$COV = \begin{bmatrix} \sigma_{C_{20}}^2 & C_1 & C_2 \\ C_1 & \sigma_{C_{22}}^2 & C_3 \\ C_2 & C_3 & \sigma_{C_{30}}^2 \end{bmatrix}.$$

We define the ellipsoid by setting the normal coefficients to $J_N = \begin{bmatrix} C_{20}^N \\ C_{22}^N \\ 0 \end{bmatrix} = \begin{bmatrix} C_{20} \\ C_{22} \\ 0 \end{bmatrix}$.

The resultant anomalous field is $J_T = J - J_N = \begin{bmatrix} C_{20}^T \\ C_{22}^T \\ C_{30}^T \end{bmatrix} = \begin{bmatrix} 0 \\ 0 \\ C_{30} \end{bmatrix}$

Ellipsoid:

$$r_{ell} = R\left\{1 + \frac{1}{3}q_r + \left[C_{20}^N - \frac{1}{3}q_r + \frac{1}{6}q_t\right]Y_{2,0} + \left[C_{22}^N - \frac{1}{12}q_t\right]Y_{2,2}\right\} =$$

$$= R\left\{1 + \frac{1}{3}q_r + \left[C_{20} - \frac{1}{3}q_r + \frac{1}{6}q_t\right]Y_{2,0} + \left[C_{22} - \frac{1}{12}q_t\right]Y_{2,2}\right\}$$

Geoid:

$$r_{geo} = R\left\{1 + \frac{1}{3}q_r + \left[C_{20} - \frac{1}{3}q_r + \frac{1}{6}q_t\right]Y_{2,0} + \left[C_{22} - \frac{1}{12}q_t\right]Y_{2,2} + C_{30}Y_{3,0}\right\}$$

The ellipsoid is a reference surface and has no associated uncertainty.

On the other hand the geoid is defined by the estimated parameters:

$$\frac{\partial r_{geo}}{\partial x} = R[Y_{20} \quad Y_{22} \quad Y_{30}]$$

$$\sigma_{r_{geo}}^2 = \left(\frac{\partial r_{geo}}{\partial x}\right) COV \left(\frac{\partial r_{geo}}{\partial x}\right)^T = R^2[Y_{20} \quad Y_{22} \quad Y_{30}]\begin{bmatrix}\sigma_{C_{20}}^2 & C_1 & C_2 \\ C_1 & \sigma_{C_{22}}^2 & C_3 \\ C_2 & C_3 & \sigma_{C_{30}}^2\end{bmatrix}\begin{bmatrix}Y_{20} \\ Y_{22} \\ Y_{30}\end{bmatrix} =$$

$$= R^2\left\{\sigma_{C_{20}}^2 Y_{20}^2 + \sigma_{C_{22}}^2 Y_{22}^2 + \sigma_{C_{30}}^2 Y_{30}^2 + 2C_1Y_{20}Y_{22} + 2C_2Y_{20}Y_{30} + 2C_3Y_{22}Y_{30}\right\}$$

The geoid heights are

$$\Delta r_{gh} = r_{geo} - r_{ell}$$

their uncertainty is:

$$\sigma_{\Delta r}^2 = \sigma_{r_{geo}}^2 = R^2\left\{\sigma_{C_{20}}^2 Y_{20}^2 + \sigma_{C_{22}}^2 Y_{22}^2 + \sigma_{C_{30}}^2 Y_{30}^2 + 2C_1Y_{20}Y_{22} + 2C_2Y_{20}Y_{30} + 2C_3Y_{22}Y_{30}\right\}$$

Otherwise:

$$\sigma_{\Delta r}^2 = \left(\frac{\partial \Delta r}{\partial x}\right) COV \left(\frac{\partial \Delta r}{\partial x}\right)^T = R^2[Y_{20} \quad Y_{22} \quad Y_{30}]\begin{bmatrix}\sigma_{C_{20}}^2 & C_1 & C_2 \\ C_1 & \sigma_{C_{22}}^2 & C_3 \\ C_2 & C_3 & \sigma_{C_{30}}^2\end{bmatrix}\begin{bmatrix}Y_{20} \\ Y_{22} \\ Y_{30}\end{bmatrix} =$$

$$= R^2\left\{\sigma_{C_{20}}^2 Y_{20}^2 + \sigma_{C_{22}}^2 Y_{22}^2 + \sigma_{C_{30}}^2 Y_{30}^2 + 2C_1Y_{20}Y_{22} + 2C_2Y_{20}Y_{30} + 2C_3Y_{22}Y_{30}\right\}$$

List of figures

List of tables

Bibliography

1. Grammier, R.S., *A look inside the Juno Mission to Jupiter,* in Aerospace Conference. IEEE, Big Sky, MT, 2009, pp. 1-10. paper #1582.

2. Bolton, S.J., *The Juno Mission,* in Proceedings of the International Astronomical Union Symposium No. 269. Padova, Italy, 2010, vol. **6**, pp. 92-100.

3. Nybakken, R., *The Juno mission to Jupiter -- A pre-launch update,* in Aerospace Conference. IEEE, Big Sky, MT, 2011, pp. 1-8. paper #1179.

4. Nybakken, R., *The Juno mission to Jupiter launch campaign and early cruise report,* in Aerospace Conference. IEEE, Big Sky, MT, 2012, pp. 1-14.

5. Lunine, J.I., et al., *The Origin of Jupiter*, in *Jupiter : the planet, satellites and magnetosphere*, F. Bagenal, T.E. Dowling, and W.B. McKinnon Editors. 2004, Cambridge University Press: Cambridge, U.K. ; New York. pp. 19-34.

6. Bagenal, F., T.E. Dowling, and W.B. McKinnon, *Introduction*, in *Jupiter : the planet, satellites and magnetosphere*, F. Bagenal, T.E. Dowling, and W.B. McKinnon Editors. 2004, Cambridge University Press: Cambridge, U.K. ; New York. pp. 1-34.

7. Seiff, A., et al., *Thermal structure of Jupiter's atmosphere near the edge of a 5-μm hot spot in the north equatorial belt.* Journal of Geophysical Research. **103**(E10): p. 22857, 1998.

8. Ingersoll, A.P., et al., *Dynamics of Jupiter's Atmosphere*, in *Jupiter : the planet, satellites and magnetosphere*, F. Bagenal, T.E. Dowling, and W.B. McKinnon Editors. 2004, Cambridge University Press: Cambridge, U.K. ; New York. pp. 1-34.

9. Kaspi, Y., et al., *Gravitational signature of Jupiter's internal dynamics.* Geophysical Research Letters. **37**(1), 2010.

10. Porco, C.C., et al., *Cassini imaging of Jupiter's atmosphere, satellites, and rings.* Science. **299**: pp. 1541-1547, 2003.

11. Atkinson, D.H., J.B. Pollack, and A. Seiff, *The Galileo Probe Doppler Wind Experiment: Measurement of the deep zonal winds on Jupiter.* Journal of Geophysical Research. **103**(E10): p. 22911, 1998.

12. Elkins-Tanton, L.T., *Jupiter and Saturn*. The solar system. 2006, New York: Chelsea House. xx, 220 p.

13. Guillot, T., et al., *The Interior of Jupiter*, in *Jupiter : the planet, satellites and magnetosphere*, F. Bagenal, T.E. Dowling, and W.B. McKinnon Editors. 2004, Cambridge University Press: Cambridge, U.K. ; New York. pp. 35-57.

14. Connerney, J.E.P., N.F. Ness, and M.H. Acuña, *Zonal harmonic model of Saturn's magnetic field from Voyager 1 and 2 observations.* Nature. **298**(5869): pp. 44-46, 1982.

15. Khurana, K.K., et al., *The Configuration of Jupiter's Magnetosphere*, in *Jupiter : the planet, satellites and magnetosphere*, F. Bagenal, T.E. Dowling, and W.B. McKinnon Editors. 2004, Cambridge University Press: Cambridge, U.K. ; New York. pp. 593-616.

16. Hubbard, W.B., *High Precision Maclaurin-based Models of Rotating Liquid Planets.* Astrophysical Journal Letters. **756**: p. L15, 2012.

17. Smith, B.A., et al., *The Jupiter System Through the Eyes of Voyager 1.* Science. **204**(4396): pp. 951-972, 1979.

18. Burns, J.A., et al., *Jupiter's Ring-Moon System*, in *Jupiter : the planet, satellites and magnetosphere*, F. Bagenal, T.E. Dowling, and W.B. McKinnon Editors. 2004, Cambridge University Press: Cambridge, U.K. ; New York. pp. 241-262.

19. Montenbruck, O. and E. Gill, *Satellite Orbits. Models, Methods, Applications*. 2000: Springer.

20. Simone, L., et al., *A Ka-band translator for radio-science applications,* in Advanced RF Sensors and Remote Sensing Instruments. ESA-ESTEC, 2009.

21. deepspace.jpl.nasa.gov, *34-Meter Beam Waveguide (BWG) Antennas*. JPL Web Site 2006; Available from: http://deepspace.jpl.nasa.gov/dsn/antennas/34m.html.

22. Tortora, P., et al., *Precise Cassini Navigation During Solar Conjunctions through Multifrequency Plasma Calibrations.* Journal of Guidance, Control and Dynamics. **27**: pp. 251-257, 2004.

23. Asmar, S.W., *Spacecraft Doppler tracking: Noise budget and accuracy achievable in precision radio science observations.* Radio Science. **40**(2), 2005.

24. Slobin, S.D., *34-m BWG Stations Telecommunications Interfaces,* DSN Telecommunications Link Design Handbook, 104, Rev. F, NASA-DSN, 2010.

25. Resch, G.M., et al., *The Media Calibration System for Cassini Radio Science: Part III,* The Interplanetary Network Progress Report, IPN PR 42-148, 2002, pp. 1-12.

26. Tanner, A.B., *Design and performance of a high-stability water vapor radiometer.* Radio Science. **38**(3), 2003.

27. Iess, L., B. Bertotti, and M. Dobrowolny, *Plasma Effects on Doppler Measurements of Interplanetary Spacecraft.* Astronomy and Astrophysics. **121**(2): pp. 203-210, 1983.

28. Tapley, B.D., B.E. Schutz, and G.H. Born, *Statistical orbit determination*. 2004, Amsterdam ; Boston: Elsevier, Academic Press. xv, 547 p.

29. JPL Navigation Software Group, *DPTRAJ-ODP User's Reference Manual, volume 1*, 1996.

30. Allen, C.W. and A.N. Cox, *Allen's astrophysical quantities*. 4th ed. 2000, New York: AIP Press : Springer. xviii, 719 p.

31. Gierasch, P., *Radiative–Convective Latitudinal Gradients for Jupiter and Saturn Models with a Radiative Zone.* Icarus. **142**(1): pp. 148-154, 1999.

32. Jacobson, R.A., *JUP230 orbit solution*, 2003.

33. Gavrilov, S.V., V.N. Zharkov, and V.V. Leontev, *Influence of Tides on the Gravitational Field of Jupiter.* Soviet Astronomy. **19**(5): pp. 618-621, 1976.

34. Milani, A. and G. Gronchi, *Theory of orbit determination*. 2010, Cambridge, UK ; New York: Cambridge University Press. x, 382 p.

35. Albertella, A., F. Sansò, and N. Sneeuw, *Band-limited functions on a bounded spherical domain: the Slepian problem on the sphere.* Journal of Geodesy. **73**(9): pp. 436-447, 1999.

36. Chashchina, O.I., L. Iorio, and Z. Silagadze, *Elementary derivation of the Lense-Thirring precession.* Acta Phys.Polon. **B40**: pp. 2363-2378, 2009.

37. Ciufolini, I., E.C. Pavlis, and R. Peron, *Determination of frame-dragging using Earth gravity models from CHAMP and GRACE.* New Astronomy. **11**(8): pp. 527-550, 2006.

38. Hubbard, W.B. and M.S. Marley, *Optimized Jupiter, Saturn, and Uranus interior models.* Icarus. **78**(1): pp. 102-118, 1989.

39. Soffel, M., et al., *The IAU 2000 Resolutions for Astrometry, Celestial Mechanics, and Metrology in the Relativistic Framework: Explanatory Supplement.* The Astronomical Journal. **126**(6): pp. 2687-2706, 2003.

40. Iorio, L., *Juno, the angular momentum of Jupiter and the Lense–Thirring effect.* New Astronomy. **15**(6): pp. 554-560, 2010.

41. Moyer, T.D., *Mathematical Formulation of the Double-Precision Orbit Determination Program (DPODP)*, JPL Technical Report, JPL-TR 32-1527, NASA-JPL, 1971.

42. Heiskanen, W.A. and H. Moritz, *Physical geodesy*. Series of books in geology. 1967, San Francisco,: W. H. Freeman. vi, 364 p.